bcrs-89-25

sea bottom topography with x-band SLAR

J. Vogelzang
G.J. Wensink
G.P. de Loor
H.C. Peters
H. Pouwels
W.A. van Gein

sea bottom topography with x-band SLAR

drs. J. Vogelzang
Rijkswaterstaat, Tidal Waters Division (RWS-DGW)
ir. G.J. Wensink
Delft Hydraulics (WL)
dr.ir. G.P. de Loor
Physics and Electronics Laboratories FEL-TNO
ir. H.C. Peters
Rijkswaterstaat, North Sea Directorate (RWS-DNZ)
ir. H. Pouwels
National Aerospace Laboratory (NLR)
ir. W.A. van Gein
Hydrogr. Service of the Royal Netherlands Navy (DH)

report bcrs 89-25
final report project TO-3.10

October 1989

This research has been carried out with financial support of the Netherlands remote sensing board (bcrs)

CONTENTS

SUMMARY

It is known for some time now that under favorable conditions (moderate wind and strong tidal current) the bottom topography of shallow seas can be made visible using imaging radar (Side Looking Airborne Radar, SLAR and Synthetic Aperture Radar, SAR). Knowledge of sea bottom topography is important for shipping, fishery and all kinds of off-shore activities as harbour construction and routing oil pipes and telecommunication cables.

In this work we report on the BCRS project 'bottom topography'. The aim of this project was to investigate the usability of imaging bottom topography with SLAR and SAR for cartographic purposes, to establish the possibilities of this method in terms of mapping accuracy and geometrical resolution and to establish the optimum hydro-meteorological conditions.

The main part of this project is formed by an experiment with the Dutch Digital SLAR in a test area off the Dutch coast. With this HH polarized X-band SLAR system and the PARES software for processing the data, it is possible to obtain both geometrically and radiometrically correct images.

As a preparation of this experiment, a number of radar images has been made of the area off the coast of Zeeland and Zuid Holland using the 'oil-SLAR'. This is a VV polarized X-band SLAR system, carried by the oil patrol aircraft of the Dutch Coast Guard. Though this radar is primarily intended to detect oil spills, the images frequently show bottom topography. Therefore these images can be used to establish the optimum hydro-meteorological conditions. A number of images, all taken around Low Water at Hoek van Holland, is compared with wind and wave data. It is concluded that the optimum wind speed for imaging bottom topography with the 'oil-SLAR' is between 4 and 10 m/s (3 - 5 Bft). There is no evidence for any dependence on the wind- or flight direction. The current velocity should be as large as possible.

A number of models describing the imaging mechanism has been put forward. According to these models, the imaging mechanism consists of three steps :

1. The interaction between bottom topography and (tidal) current causes modulations in the current velocity at the surface. This is usually described with the continuity equations.
2. These current velocity modulations cause spatial variations in the wave spectrum, described by the action balance equation.
3. Spatial wave spectrum variations show up as intensity variations in the radar image. This is commonly described with first order Bragg scattering.

Three existing one-dimensional models of the imaging mechanism (Alpers and Hennings, 1984 ; Shuchman, Lyzenga and Meadows, 1985 ; Holliday, St-Cyr and Woods, 1987) have been compared by solving the action balance equation numerically. It is shown that if advection is taken into account, these three models (further referred to as simple relaxation models) give similar results. In particular, these models predict that for X-band at winds exceeding 5 m/s (3 Bft) the extremes in the radar backscatter are located right above regions with maximum bottom slope.

The main experiment was performed in an area 20 km NW to the Noordwijk Tower (Meetpost Noordwijk, MPN). The bottom topography here is dominated by sand waves with a crest-to-crest distance of typically 500 m and a height between 2 and 6 m at a depth of 23 m. This area has been chosen for the following reasons :

1. The bottom topography is relatively simple and quasi one-dimensional. Therefore the results can be compared with predictions by the one-dimensional simple relaxation models.
2. Wind, temperature and wave data are measured on a routine base on MPN.
3. The area has been studied frequently in the past with imaging radar.

The test area consists of two mutually perpendicular rectangles with common centre, each measuring 5 x 10 km. The rectangles are oriented in the direction of the sand wave crests and the dominating current. Two flights were made, with opposing directions of the current velocity to study its influence. During each flight both rectangles were recorded from both directions parallel to the longer sides. Therefore the central 5 X 5 km of the test area was recorded from four different directions. The periods in the tidal cycle during which the current velocity reaches its maximum values were found from old current measurements on MPN.

As remarked before, the optimum wind speed for mapping bottom topography with the 'oil-SLAR' is between 4 and 10 m/s (3 - 5 Bft). This value agrees with the experience from other radar systems. This does not automatically imply that this is also the optimum wind speed for the Dutch Digital SLAR, since there exists a minimum wind speed at which the radar backscatter of the sea is detectable with the radar system being used. The Dutch Digital SLAR is a rather insensitive instrument. Because the radar backscatter of the sea increases with increasing wind speed, the optimum wind speed for the Dutch Digital SLAR is estimated between 7 and 10 m/s (5 Bft).

During the experiment the current velocity profile was measured from two ships near the centre of the test area: the one located above a crest (the 'Octans') and the other above a trough (the 'Smal Agt'). From these profiles and the wind data from MPN the mean and surface current velocity vectors were calculated using the method of Davies (1987, 1988). The position of the 'Octans' was recorded with high precision. These data have been used to position the radar images relative to digitized bathymetric maps with an error of 2 pixels (30 m). Digitized bathymetric maps were constructed from an ordinary bathymetric map of the test area using spline interpolation techniques. This method makes it possible to calculate not only the depth at any point of the test area, but also the bottom slopes.

The experiment was performed on January 19th, 1988. The wind speed varied between 7.3 and 8.3 m/s (5 Bft); the surface current velocity perpendicular to the sand wave crests between 0.6 and 0.8 m/s. The results for the mean current velocity agree with the continuity equations. However, since the current velocity was measured at two points only, this can not be regarded as conclusive evidence for the validity of the continuity equations. The quality of the radar images is rather poor and depends on the angle between wind- and flight direction, due to the low sensitivity of the Dutch Digital SLAR. The images with range direction pointing upwind/crosswind and flight direction parallel to the sand wave crests show the sand waves most clearly.

These images have been compared with digitized maps of depth and bottom slope by overlaying maps and images and by calculating the correlation between the two. It appears that the extremes in the radar backscatter are located right above regions with maximum bottom slope, within the error in position (2 pixels, 30 m). This is in perfect agreement with predictions from simple relaxation models. The quality of the images obtained during the experiment is not good enough to calculate the bottom slope from the images (inverse modelling).

The most important conclusions from this study are :

1. The extremes in the radar backscatter are located above regions with maximum bottom slope for X-band at a wind speed between 7.3 and 8.3 m/s (5 Bft).
2. The optimum wind speed depends on the sensitivity of the radar system being used.

Since radar images show the slope of bottom related features over a large area, such images can be used to optimize time- and cost consuming bathymetric surveys, notably in regions where the sea bottom is not well known like the coastal waters of developing countries. It should be mentioned here that SEASAT L-band imagery has already been used to route telephone cable UK-NL 12.

The mapping of bottom topography with imaging radar can become a very useful technique. However, the influence of many parameters (current velocity, radar wavelength and polarization) is not well known yet. Further investigation during the ERS-1 and SIR-C/X-SAR missions is recommended.

SAMENVATTING (SUMMARY IN DUTCH)

Het is reeds geruime tijd bekend dat onder gunstige omstandigheden (matige wind en sterke getijstroom) de bodemtopografie van ondiepe zeeën zichtbaar gemaakt kan worden met behulp van beeldvormende radar (Side Looking Airborne Radar, SLAR en Synthetic Aperture Radar, SAR). Kennis van de bodemtopografie is van groot belang voor scheepvaart, visserij en allerlei off-shore activiteiten zoals de bouw van havens en het leggen van pijpleidingen en telefoonkabels.

In dit rapport brengen we verslag uit van het BCRS project 'bodemtopografie'. Het doel van dit project was te onderzoeken in hoeverre opnames van de bodemtopografie door SLAR en SAR bruikbaar zijn voor kartografische doeleinden, vast te stellen wat de mogelijkheden en beperkingen zijn in termen van nauwkeurigheid en geometrische precisie en vast te stellen welke hydro-meteorologische omstandigheden het beste zijn.

Het belangrijkste deel van dit project wordt gevormd door een experiment met de 'Nederlandse Digitale SLAR' in een proefgebied voor de Nederlandse kust. Met dit HH-gepolariseerde X-band SLAR systeem en de PARES programmatuur voor de verwerking van de gegevens is het mogelijk om zowel geometrisch als radiometrisch correcte beelden te verkrijgen.

Ter voorbereiding op dit experiment zijn een aantal radaropnames gemaakt van de Voordelta (het gebied voor de Zeeuwse en Zuid-Hollandse kust) met behulp van de 'olie-SLAR'. Dit is een VV-gepolariseerd X-band SLAR systeem, geplaatst in het olieopsporingsvliegtuig van de Kustwacht. Ofschoon dit radarsysteem in de eerste plaats bedoeld is voor het detecteren van olievervuiling, laten de hiermee gemaakte opnames regelmatig bodemtopografie zien. Derhalve kunnen deze beelden gebruikt worden om de beste hydrometeorologische omstandigheden te bepalen. Een aantal opnames, allen gemaakt rond Laag Water te Hoek van Holland, is vergeleken met wind- en golfgegevens. Hieruit is geconcludeerd dat de beste windsnelheid voor het waarnemen van bodemtopografie met de 'olie-SLAR' tussen 4 en 10 m/s (3 - 5 Bft) ligt. Er zijn geen aanwijzingen gevonden voor enige afhankelijkheid van de wind- of vliegrichting. Wel moet de stroomsnelheid zo groot mogelijk zijn (groter dan 0.4 m/s).

In de literatuur zijn een aantal modellen voor de beschrijving van het beeldvormende mechanisme voorgesteld. Volgens deze modellen bestaat het beeldvormende mechanisme uit drie stappen :

1. De wisselwerking tussen de bodemtopografie en de (getij) stroom veroorzaakt modulaties in de stroomsnelheid aan het oppervlak. Dit wordt doorgaans beschreven met de continuiteitsvergelijkingen.
2. De modulaties in de stroomsnelheid aan het oppervlak veroorzaken plaatselijke variaties in het golfspectrum, zoals beschreven door de actiebalansvergelijking.
3. Plaatselijke variaties in het golfspectrum worden op radaropnames zichtbaar als modulaties in de intensiteit. Dit wordt meestal beschreven met behulp van eerste orde Bragg verstrooiing.

Drie bestaande, een-dimensionale modellen voor het beeldvormende mechanisme (Alpers en Hennings, 1984 ; Shuchman, Lyzenga en Meadows, 1985 ; Holliday, St-Cyr en Woods, 1987) zijn onderling vergeleken door de actie-balansvergelijking numeriek op te lossen. Hieruit blijkt dat, wanneer advectie wordt meegenomen, deze drie modellen (in het vervolg aangeduid als eenvoudige relaxatiemodellen) vergelijkbare resultaten opleveren. In het bijzonder voorspellen deze modellen dat voor X-band bij een wind van meer dan 5 m/s

(3 Bft) de extreme waardes van de teruggestrooide radarstraling precies gepositioneerd zijn boven de gebieden met de grootste bodemhelling.

Het experiment is uitgevoerd in een gebied op 20 km ten NW van Meetpost Noordwijk (MPN). De bodemtopografie in dit gebied bestaat uit zandgolven met een onderlinge afstand tussen de toppen van typisch 500 m en een hoogte tussen 2 en 6 m op een diepte van ongeveer 23 m. Dit gebied is om de volgende redenen gekozen :

1. De bodemtopografie is relatief eenvoudig en bijna een-dimensionaal. Derhalve kunnen de uitkomsten van het experiment vergeleken worden met de voorspellingen van de een-dimensionale eenvoudige relaxatiemodellen.
2. Gegevens omtrent wind, temperatuur en golven worden routinematig op MPN ingewonnen.
3. Het gebied is in het verleden meerdere malen bestudeerd met behulp van beeldvormende radar.

Het proefgebied bestaat uit twee onderling loodrechte rechthoeken met gemeenschappelijk middelpunt, van elk 5 bij 10 km. De rechthoeken zijn georienteerd in de richting van de zandgolven en de dominerende stroomsnelheid. Er zijn twee vluchten gemaakt, bij tegengestelde richtingen van de stroomsnelheid om de invloed hiervan te bestuderen. Gedurende iedere vlucht is elk van beide rechthoeken opgenomen vanuit beide richtingen parallel aan de langste zijde. Zodoende is het centrale deel van 5 x 5 km opgenomen vanuit vier verschillende richtingen. Uit oude metingen van de stroomsnelheid bij MPN zijn de periodes in de getijcyclus bepaald waarin de stroomsnelheid maximaal is.

Zoals reeds eerder is opgemerkt ligt de optimale windsnelheid voor het waarnemen van bodemtopografie met behulp van de 'olie-SLAR' tussen 4 en 10 m/s (3 - 5 Bft). Deze waarde stemt overeen met ervaringen vanuit andere radarsystemen. Dit betekent echter niet automatisch dat dit dan ook de beste windsnelheid voor de 'Nederlandse Digitale SLAR' is, aangezien er een minimum windsnelheid bestaat waarbij het door de zee teruggestrooide radarsignaal detecteerbaar is door het gebruikte radarsysteem. De 'Nederlandse Digitale SLAR' blijkt een tamelijk ongevoelig instrument. Aangezien de hoeveelheid door de zee teruggestrooide radarstraling toeneemt met toenemende windsnelheid, ligt de optimale windsnelheid voor de 'Nederlandse Digitale SLAR' tussen 7 en 10 m/s (5 Bft).

Gedurende het experiment is het stroomsnelheidsprofiel gemeten vanaf twee schepen in of nabij het centrum van het proefgebied : een schip boven een top van een zandgolf (de 'Octans') en de ander boven een dal (de 'Smal Agt'). Uit de gemeten profielen en de windgegevens van MPN zijn de gemiddelde stroomsnelheidsvector en de stroomsnelheidsvector aan het oppervlak berekend met behulp van de methode van Davies (1987, 1988). De positie van de 'Octans' is met grote nauwkeurigheid vastgelegd. Deze gegevens zijn gebruikt om de postie van de radaropnames ten opzichte van de digitale dieptekaarten vast te leggen met een fout van twee pixels (30 m). Uit een gewone dieptekaart zijn digitale dieptekaarten geconstrueerd met behulp van spline interpolatie. Op deze manier is het mogelijk om op ieder punt van het proefgebied niet alleen de diepte maar ook de bodemhelling te berekenen.

Het experiment is uitgevoerd op 19 januari 1988. De windsnelheid varieerde tussen 7.3 en 8.3 m/s; de stroomsnelheid loodrecht op de zandgolven tussen 0.6 en 0.8 m/s. De resultaten van de metingen van de stroomsnelheid zijn in overeenstemming met de continuiteitsvergelijkingen. Gezien het feit dat de stroomsnelheid slechts op twee punten gemeten is, kan dit niet gezien worden als doorslaggevend bewijs voor de geldigheid van de continui-

teitsvergelijkingen. De kwaliteit van de radaropnames is vrij slecht en hangt af van de hoek tussen vlieg- en windrichting, ten gevolge van de lage gevoeligheid van de 'Nederlandse Digitale SLAR'. De beelden met de radarkijkrichting schuin tegen de wind in en de vliegrichting parallel aan de zandgolven vertonen de zandgolven het duidelijkst.

Deze beelden zijn vergeleken met digitale kaarten van diepte en bodemhelling door kaarten en beelden over elkaar te leggen, en door de correlatie tussen beide te berekenen. Hieruit blijkt dat de extreme waarden in de hoeveelheid teruggestrooide radarstraling gelocaliseerd zijn precies boven gebieden met maximale bodemhelling, binnen de fout in positie (twee pixels, 30 m). Dit komt voortreffelijk overeen met de voorspellingen van eenvoudige relaxatiemodellen. De kwaliteit van de beelden is niet goed genoeg om uit de radarbeelden de bodemhelling te berekenen (inverse modellering).

De belangrijkste conclusies van deze studie zijn :

1. Voor X-band radar bij een wind van 7.3 tot 8.3 m/s (5 Bft) zijn de extreme waarden in de hoeveelheid teruggestrooide radarstraling precies gepositioneerd boven gebieden met maximale bodemhelling.
2. De optimale windsnelheid voor het waarnemen van bodemtopografie hangt af van de gevoeligheid van het radarsysteem.

Omdat radarbeelden de helling van bodemstructuren laten zien over een groot gebied, kunnen dergelijke opnames gebruikt worden voor het optimaliseren van dure en tijdrovende bathymetrische meetprogramma's, in het bijzonder in gebieden waar de zeebodem niet goed bekend is zoals de kustwateren van ontwikkelingslanden. Het dient hier opgemerkt te worden dat SEASAT L-band beelden reeds gebruikt zijn voor het bepalen van de optimale route van telefoonkabel UK-NL 12.

Kartering van de bodemtopografie met beeldvormende radar kan een zeer bruikbare techniek worden. Echter, de invloed van veel parameters (stroomsnelheid, radar golflengte en -polarisatie) is niet goed bekend. Verder onderzoek gedurende de ERS-1 en SIR-C/X-SAR missies wordt dan ook aanbevolen.

SYMBOLS USED

In this section the symbols used in this work are listed in order of appearance.

T_0 : Recording time of 'oil-SLAR' image
T_{HW} : Time of high water at Hoek van Holland
δT : Difference between T_0 and T_{HW}
V : Surface current velocity with components V_{par} and V_{per}
H_s : Significant wave height
h : Water depth
U : Depth averaged or mean current velocity, with components U_x and U_y or U_{per} and U_{par}
x, y, z : Spatial coordinates
ξ : Elevation of the water surface (sea level)
g : Gravitational acceleration
s : Slope of the coordinate system with components s_x and s_y
τ_b : Bottom shear stress with components τ_{bx} and τ_{by}
ρ : Water density
C : Chezy's factor
r : Bottom shear stress factor
Ω_v : Vorticity
β : Angle of local bottom slope
C_{par} : Constant
C_{per} : Constant
Ω : Apparent wave frequency
A : Action spectrum
S : Source term in action balance equation
k : Wave number
ω : Intrinsic wave frequency
γ : Ratio of surface tension and water density
c_g : Group velocity of water waves
E : Energy spectrum
μ : Relaxation rate or wave growth rate
τ_r : Relaxation time (inverse of μ)
A_0 : Equilibrium action spectrum
δA : Deviation of the action spectrum from equilibrium
V_0 : Unperturbed surface current velocity
δV : Perturbation in surface current velocity
τ_a : Advection time
K : Wave number of bottom topography
a : Phillips parameter
c_p : Phase velocity of water waves
u_z : Wind speed at z meter anemometer height relative to the water
u_* : Friction wind velocity
κ : Von Karman's constant
z_0 : Roughness length
σ_0 : Normalized radar cross section (NRCS)
θ : Angle of incidence
g_{pq} : Backscatter function for first order Bragg scattering
W : Two-dimensional wave number spectral density of sea surface roughness
k_B : Bragg wave number

ε_r : Relative complex dielectrical constant
α_i : Angle between the vertical and the normal of the sea surface in the plane of incidence
β_i : Angle between the vertical and the normal of the sea surface in a plane perpendicular to the plane of incidence
θ_i : Local angle of incidence
P : Joint probability density of slopes for large scale sea roughness
h_0 : Unperturbed water depth
ξ_0 : Unperturbed sea level (or water surface elevation)
δh : Difference in depth
$\delta \xi$: Difference in sea level (or water surface elevation)
V_m : Modulation in surface current velocity
b : Surface current modulation length
ΔV : Relative difference in surface current velocity
ΔA : Relative difference in action spectral density
φ : Phase shift
α : Modulation depth
w_{10} : Wind speed at 10 m anemometer height relative to a fixed coordinate system
T_{max} : Time of maximum current velocity
V_{max} : Maximum current velocity
T_{LWS} : Time of low water at Scheveningen
T_{HWS} : Time of high water at Scheveningen
P_x : Pixel size in x-direction
P_y : Pixel size in y-direction
Φ : Image direction
H_{ij} : Geographical height of pixel j on line i
L_{ij} : Geographical length of pixel j on line i
R_H : Length of one minute geographical height
R_L : Length of one minute geographical length
D : Discharge
k_c : Cutoff wave number
k_{max} : Maximum wave number
C : Cutoff factor
γ_0 : Reflection coefficient
$\nabla_{per}(h)$: Bottom slope in the direction of the current velocity component normal to the sand wave crests
C_j : Correlation coefficient between image and map with image shifted over j pixels in the direction of the current relative to map
$\overline{M}$: Mean pixel value of bottom slope in digitized map
$\overline{I_j}$: Mean value of radar intensity in image with image shifted over j pixels in the direction of the current relative to map

CONVENTIONS

All dimensional quantities in this work are in SI units, except when explicitly stated otherwise. The direction of wind, current and radar images is expressed in degrees clockwise in respect to true North (degrees true North).

It is worth noting that it is common practice to define current direction as the direction to which the current is flowing, expressed in degrees measured clockwise from the North (degrees true North). This definition is clearly opposed to the definition of wind and wave direction, which is defined as the direction from which the wind is blowing or the direction from which the waves are coming, also expressed in degrees true North. Therefore care must be taken to avoid confusion between wind and current direction.

The wind speed is always given at some reference height. There are two 'official' reference heights : 10 m and 19 m. Both are used in this work. Unfortunately, the reference height is not indicated clearly in much of the literature. In this work the wind speed at anemometer height z is defined both relative to the water (denoted as u_z) and to a fixed coordinate system (denoted as w_z). It is only in the absence of currents that u_z and w_z are identical. The wind speed in this work is given both in m/s and Bft (Beaufort). As a reference, the next table gives the relation between the two.

Wind speed at 10 m	
Bft	m/s
0	0.0 - 0.2
1	0.3 - 1.5
2	1.6 - 3.3
3	3.4 - 5.4
4	5.5 - 7.9
5	8.0 - 10.7
6	10.8 - 13.8
7	13.9 - 17.1
8	17.2 - 20.7
9	20.8 - 24.4
10	24.5 - 28.4
11	28.5 - 32.6
12	> 32.6

1 INTRODUCTION

1.1 Historical overview

It is known for some time now that under suitable conditions (moderate wind speed and strong tidal current) the sea bottom topography is visible in images taken by Side Looking Airborne Radar (SLAR) and Synthetic Aperture Radar (SAR). This phenomenon has been discovered by de Loor in 1969 in Q-band SLAR imagery of the North Sea (de Loor and Brunsveld van Hulten, 1978 ; de Loor, 1981). These images were made off the Dutch coast to study the detection of waves and swell directions. The images revealed some kind of wave patterns, which originally were believed to be caused by swell. However, it was observed that the patterns were fixed in position and disappeared during high and low tide in the test area, when the tidal current velocity vanishes. Then it was realized that these patterns were caused by sand waves. The phenomenon was observed regularly since 1974, when the UK EMI X-band SLAR came in regular use in the Netherlands (this system will be referred to as the old EMI SLAR; it was in use till 1980). In later experiments also tidal patterns, currents and internal waves were observed.

At first this phenomenon was considered a disturbing factor, obscuring oil spills in radar images, and little attention was paid to it. This changed drastically after the SEASAT mission in 1978. SEASAT carried a L-band SAR that recorded spectacular images of bottom topography in shallow seas like the Southern Bight of the North Sea (Alpers and Hennings, 1984), the English Channel (Lodge, 1983), and the Nantucket Shoals (Shuchman, Lyzenga and Meadows, 1985). All SEASAT images showing bottom related structures are reviewed by Kasischke et al. (1983). Besides bottom topography the SEASAT images also frequently show other phenomena like internal waves (Rufenach and Smith, 1985) and ship wakes (Vesecky and Stewart, 1982).

The SEASAT mission demonstrated the potential of radar remote sensing for the study of the ocean and aroused much interest. It stimulated further research, both experimental (McLeish et al., 1981 ; Valenzuela et al., 1985) and theoretical (Alpers and Hennings, 1984 ; Shuchman, Lyzenga and Meadows, 1985 ; Holliday, St-Cyr and Woods, 1987 ; van Gastel, 1987a, Hennings, 1988). Also practical applications were considered (Hennings, 1985 and 1988).

1.2 Aims and scope of this work

Knowledge of the bottom topography of shallow seas is important for fishery, harbour construction and off-shore activities like routing oil pipes and telecommunication cables. It is not (yet?) possible to extract precise bathymetric data from radar images. Therefore this technique will not replace the traditional time and cost consuming bathymetric surveys. However, radar imagery gives an overview of large area's. It can therefore be used to optimize bathymetric surveys. This can be most important for regions where the bathymetry is not well known like the coastal waters of developing countries.

From 1 November 1986 onwards the project 'bottom topography' was carried out to investigate the usability of SLAR and SAR images for mapping sea bottom topography. The goals of the project were :

1. To establish the optimum meteorological and hydrodynamical conditions for mapping sea bottom topography with SLAR and SAR.
2. To establish the possibilities and limitations in terms of mapping accuracy and resolution.
3. To develop methods for mapping sea bottom topography with SLAR and SAR on a routine base.

This work was funded by the Netherlands Remote Sensing Board (BCRS) as a part of the National Remote Sensing Program (NRSP). The project team is :

W.A. van Gein	Hydrographic Service of the Royal Netherlands Navy (DH)
G.P. de Loor	Physics and Electronics Laboratory (FEL-TNO)
H.C. Peters	Rijkswaterstaat, North Sea Directorate (RWS-DNZ)
H. Pouwels	National Aerospace Laboratory (NLR)
D. Spitzer	Rijkswaterstaat, Tidal Waters Division (RWS-DGW)
J. Vogelzang	Rijkswaterstaat, Tidal Waters Division (RWS-DGW)
G.J. Wensink	Delft Hydraulics (WL)

Project leader is J. Vogelzang. The meetings of the project team were attended by A.C. de Bruin and S.A.P. Frelier (PTT Telecom).

1.3 Project activities

The main part of this project is formed by an experiment performed in a test area off the Dutch coast. This experiment will be referred to as the main experiment. In the test area radar images were taken by the Dutch Digital SLAR operated by the National Aerospace Laboratory (NLR). With this system and the image processing facilities at NLR both radiometrically and geometrically correct images can be obtained. The necessary sea truth was collected simultaneously by Rijkswaterstaat. The images obtained during the experiment are compared with digitized bathymetric maps of the test area to study the relation between the bottom topography visible on the maps and in the radar images. This yields information about the possibility to use images by SLAR and SAR for cartographic purposes. As a by-product, the relation between radar image and bathymetric map can be compared with predictions by existing theories of the imaging mechanism. By measuring the current velocity in the test area during the experiment it is also possible to check theoretical predictions of the radar backscatter by means of model calculations.

In preparation of this experiment the following activities were carried out:

1. Collection of images taken by the 'oil-SLAR' of Rijkswaterstaat in an area off the coast of Zeeland and Zuid Holland.
2. Making an inventory of area's on the North Sea suitable for further investigation and establishing the optimum conditions to observe sea bottom topography.
3. Evaluation and choice of the test area, making an inventory of and archieving the images and hydro-meteorological data of the test area.

This report describes all of these activities, including the main experiment with the Dutch Digital SLAR.

1.4 Introductory remarks on this report

The oil patrol aircraft of the Dutch Coast Guard is equipped with several sensors, among which an Ericsson X-band SLAR (the 'oil-SLAR'). From 1986 onwards a series of images has been made of the area off the coast of Zeeland and Zuid Holland. Chapter 2 deals with the evaluation of these 'oil-SLAR' images, the most of which are taken around low tide at Hoek van Holland. The relevant wind and wave data that could be retrieved is presented and the optimum wind speed for mapping bottom topography with X-band SLAR is estimated. All 'oil-SLAR' images were recorded during current velocities exceeding 0.4 m/s. These values are considered as favorable for mapping bottom topography (Alpers and Hennings, 1984 ; van Gastel, 1987a). No evidence has been found for any dependence on wind or flight direction. The optimum wind speed for mapping bottom topography with the 'oil-SLAR' is estimated between 4 and 10 m/s (3 - 5 Bft). However, it was realized during the project that the optimum wind speed also depends on the sensitivity of the radar system. Therefore this is not a priori the optimum wind speed for the Dutch Digital SLAR.

Chapter 3 contains the theoretical description of the imaging mechanism. It is generally accepted that the imaging mechanism consists of three steps:

1. Interaction between (tidal) current and bottom topography produces modulations in the surface current velocity.
2. Modulations in the surface current velocity cause variations in the wave spectrum.
3. Variations in the wave spectrum cause modulations in the radar backscatter.

The modelling of these three steps is described. The hydrodynamic modulation (second step) is calculated by solving the action balance equation numerically for three existing simple relaxation models (Alpers and Hennings, 1984 ; Shuchman, Lyzenga and Meadows, 1985 ; Holliday, St-Cyr and Woods, 1987). Comparison shows that the difference between the three models is small. Advection is important at L-band but can in most cases be neglected at X-band. The hydrodynamic modulation at X-band is an order of magnitude smaller than that at L-band. The change of the sea surface due to variations in the current velocity is estimated using Bernouilli's law. It is shown that this effect can be neglected. Though this chapter is quite technical in nature, the reader is advised to study the introduction and the conclusions in order to appreciate the subsequent chapters.

In chapter 4 the choice of the test area, tidal phase, wind speed, flight tracks and sea truth for the main experiment is discussed. For the experiment a location 20 km NW to the Noordwijk Platform (MPN) has been chosen. The period in the tidal cycle during which the current velocity reaches its maximum value is estimated using old current measurement at MPN. As stated before, it was realized during the project that the optimum wind speed depends on the sensitivity of the radar system being used. Using a parametrization of the radar cross section of the sea surface as a function of angle of incidence and wind speed, the optimum wind speed for mapping bottom topography is estimated between 7 and 10 m/s (5 Bft).

Chapter 5 deals with the further processing of the data collected during the main experiment. This chapter contains a description of how a digitized bathymetric map was constructed from an ordinary bathymetric map using spline interpolation techniques. With this approach it is not only possible to calculate the depth at each point of the test area, but also the slope

of the sea bottom in any direction. This chapter ends with solving the problem of positioning the radar images relative to the bathymetric map. This chapter is also technical in nature. It can be skipped by readers not interested in details.

The results of the main experiment and their discussion are the subject of chapter 6. The images and the sea truth are presented. The results of the current velocity measurements agree with the continuity equations, but cannot be regarded as conclusive evidence for the validity of these equations due to the large errors in the measurements. The quality of the radar images is rather poor. Therefore the images have been filtered to make the sand waves better visible. The best results have been obtained with a median filter. The modulation depth in the images is found to be an order of magnitude larger than the hydrodynamic modulation predicted by simple relaxation models. Comparison of the radar images with digitized maps shows that the extremes in the radar backscatter are positioned above regions with maximum bottom slope, with an error of two pixels (30 m). This is in perfect agreement with the prediction of simple relaxation models. The positional relation between images and maps is quantified by calculating the correlation between the two. The quality of the images is not good enough for inverse modelling.

The results of this study concerning the imaging mechanism, optimum hydro-meteorological conditions and practical applicability are summarized in chapter 7. This chapter also contains the conclusions and recommendations for future activities.

Finally, the reader is referred to the list of symbols and the conventions used in this work. These are listed in the beginning of this report.

2 EVALUATION 'OIL-SLAR' IMAGES

2.1 Introduction

The oil patrol aircraft of the Dutch Coast Guard is equipped with several sensors. One of them is a X-band Ericsson SLAR, the 'oil-SLAR'. Table 1 contains some data of this system.

TRANSMITTER	
radar frequency	9.4 GHz
pulse power	10 kW
pulse width	500 ns
pulse frequency	1 kHz
ANTENNA	
construction	slotted wave guide, VV polarization
antenna length	3 m (double sided)
horizontal beam width	0.5° (one-way)
gain	31 dB
RECEIVER	
dynamic range	50 dB
DISPLAY	
displayed area	20 x 80 km
pixel size	75 x 75 m

Table 1. Specifications of the 'oil-SLAR'.

As a preparation for the main experiment a series of images has been made of the area off the coast of Zeeland and Zuid Holland in the Southwestern part of the Netherlands, starting in 1986. Though the 'oil-SLAR' is primarily intended to detect oil spills, its images frequently show sea bottom topography. These images are neither radiometrically nor geometrically corrected. Therefore they cannot be compared in detail with bathymetric maps, in contrast with the images of the Dutch Digital SLAR. However, the 'oil-SLAR' images offer a cheap and easy way to study the visibility of bottom topography in a range of hydro-meteorological conditions.

This chapter deals with the study of a number of 'oil-SLAR' images, recorded during 1986 and 1987. The relevant wind and wave data, as far as retrievable, is presented. From these images it is concluded that there is no dependence between the quality of the images and the wind or flight direction. The optimum wind speed for imaging bottom topography with the 'oil-SLAR' is estimated between 4 and 10 m/s (3 - 5 Bft).

However, as explained in chapter 4, this optimum wind speed depends on the sensitivity of the radar system. Due to the lower sensitivity of the Dutch Digital SLAR the main experiment had to be performed at a higher wind speed.

2.2 Images and flight data

The images are numbered in order of the recording date. During several days a number of images has been made from different flight directions. These images have a character (a, b, ...) behind their number. Table 2 contains the flight data, as far as retrievable. The starting time T_0 of each image is written as hh:mm:ss. All times are in MET.

The heading of the aircraft is measured clockwise, starting from the North. The heading (the direction to which the nose of the aircraft is pointing) roughly corresponds with the flight direction relative to the ground. The difference between the two directions is caused by the wind. There might be a variation of several degrees in heading and flight direction relative to the ground due to variations in the wind speed. Since the 'oil-SLAR' images will not be compared in detail with bathymetric maps these effects are not considered in further detail. The majority of the images is taken with the heading parallel to the coast line. Only images 3c, 3d, 4b, 8b, 9c and 10b have a heading perpendicular to the coast line.

Image number	Date	T_0 (MET)	Heading deg.	direction	Height (ft)
1	Feb 27 '86	11:01:55	40	NE	1100
2	Mar 3 '86	14:57:02	217	SW	1500
3a	May 2 '86	14:44:42	217	SW	1600
3b		15:09:58	54	NE	1500
3c		15:27:40	142	SE	1500
3		15:39:49	302	NW	1500
4a	Jun 13 '86	14:01:21	217	SW	1100
4b		14:49:35	307	NW	1100
5a	Jul 20 '86	07:49:35	220	SW	1300
5b		08:12:53	35	NE	1300
6	Aug 31 '86	06:48:24	220	SW	-
7a	Sep 20 '86	10:31:56	220	SW	1000
7b		10:54:01	38	NE	1000
8a	Oct 16 '86	08:27:42	219	SW	1100
8b		08:43:28	339	NW	1100
8c		08:47:43	42	NE	1100
9a	Nov 7 '86	08:34:53	219	SW	1200
9b		09:06:16	39	NE	1200
9c		09:32:52	293	NW	1200
10a	Feb 22 '87	14:20:13	222	SW	1300
10b		15:18:30	325	NW	1300

Table 2. Images and flight data.

The range direction is perpendicular to the heading, both to the left and to the right of the aircraft. All images were taken from a height between 1000 and 1600 ft (between 300 and 480 m). The angle of incidence varies from about 45° to 89° at the edge of the images.

2.3 Current

Table 3 contains tidal and current data. T_{HW} is the time of the nearest (in time) high tide at Hoek van Holland, denoted as hh:mm. The values of T_{HW} are taken from the tidal tables (Rijkswaterstaat, 1985 and 1986). δT is the difference between T_{HW} and T_0, the time on which the recording of the images was started, rounded off to whole hours. V is the (temporal) mean surface current velocity in the area off the coast of Zeeland and Zuid Holland as given by the current atlas (Dienst der Hydrografie, 1976).

From table 3 it can be seen that all images except 9a, 9b and 9c are taken between low tide and two hours after low tide at Hoek van Holland. According to the current atlas the current velocity in the area considered here has its maximum during this period and is directed along the coast from NE to SW. Images 9a, 9b and 9c were taken between 3 and 4 hours after high tide at Hoek van Holland. The current velocity is also maximal during this period but pointing in the opposite direction.

Image number	T_{HW} (MET)	δT (h)	V (m/s)	Image number	T_{HW} (MET)	δT (h)	V (m/s)
1	16:33	- 6	0.4 - 1.0	6	12:31	- 6	0.7 - 1.1
2	19:44	- 5	0.6 - 1.1	7a,b	15:51	- 5	0.4 - 1.0
3a	9:24	+ 5	0.6 - 1.1	8a,b,c	13:42	- 5	0.4 - 1.0
3b,c,d	9:24	+ 6	0.4 - 1.0	9a,b	5:42	+ 3	0.4 - 1.0
4a,b	18:18	- 4	0.6 - 1.0	9c	5:42	+ 4	0.4 - 1.0
5a	13:32	- 6	0.4 - 1.0	10a	8:15	- 6	0.4 - 1.0
5b	13:32	- 5	0.4 - 1.0	10b	21:09	+ 6	0.4 - 1.0

Table 3. Current data.

2.4 Wind and wave data

The wind and wave data are presented in table 4. The wind speed and direction are taken from Logboek Meetnet Noordzee (Rijkswaterstaat, 1986 and 1987) or Monthly Bulletin North Sea (KNMI, 1986 and 1987). H_s is the significant wave height, as given by Monthly Bulletin North Sea. All wind and wave data were recorded on Lichteiland Goeree (LEG), except the data for images 10a and 10b which were measured on Europlatform.

The wind speed recorded on LEG is not reliable because the wind field at the anemometer is disturbed by other constructions. Comparison of LEG wind speeds with those recorded at other posts of the North Sea Monitoring Network shows that the LEG wind speeds can be too low, depending on the wind direction. The wind speeds from the nearest post, Europlatform, are

not complete. Therefore the wind speeds from LEG are used as an indication of the effect of the wind speed on the visibility of bottom topography.

Image number	Wind speed (m/s)	(Bft)	Wind direction (deg.)	(dir.)	H_s (m)
1	8.6	5	89	W	1.0
2	4.0	3	32	NE	0.5
3a	6 - 7	4	110 - 120	SE	0.5
3b	6 - 7	4	110 - 120	SE	0.5
3c	6 - 7	4	110 - 120	SE	0.5
3d	6 - 7	4	110 - 120	SE	0.5
4a	5.3	3	356	N	0.5
4b	6.5	4	7	N	0.5
5a	8.3	5	220	SW	1.0
5b	8.9	5	220	SW	1.0
6	8.4	5	330	NW	2.0
7a	3.7	3	285	W	0.5
7b	3.8	3	281	W	0.5
8a	10.4	5	15	N	1.5
8b	10.8	6	18	N	1.5
8c	10.8	6	18	N	1.5
9a	12 - 14	6	170 - 190	S	2.0
9b	12 - 14	6	170 - 190	S	2.0
9c	12 - 14	6	170 - 190	S	2.0
10a	6 - 8	4	350 - 10	N	1.0
10b	6 - 8	4	350 - 10	N	1.0

Table 4. Wind and wave data.

2.5 Bottom topography

Image number 2 most clearly exhibits a number of structures that can be related to bottom topography. Image number 2 is shown in figure 1. The projection of the aircraft track on the ground is located in the middle of the image. The aircraft was flying from top to bottom. The current direction is also from top to bottom. From figure 1 it can be seen that the quality of the image decreases towards the edges, where the backscattered intensity decreases, and towards the centre, where the backscattered intensity is very high due to specular reflections. This decrease in quality affects the visibility of bottom related structures. The names of some features visible on figure 1 are shown in figure 2.

Table 5 shows whether or not some structures on image 2 ('Bollen van Goeree' ; 'Oosterhinder' ; 'Banjaard', 'Noordland' and 'Hompels' ; 'Middelbank' and 'Steenbanken') are visible in the other images. A plus sign indicates that the structure is visible, a question mark that the structure is invisible because it is located outside or near the edge of the image. A minus sign means that the structure is not visible though it is expected to be.

Sand waves are visible in image 2 (near 'Oosterhinder'), in image 3d (off the coast of Goeree) and in images 7b, 8a, 8b, 8c and 10b (off the coast of Walcheren). Their visibility is indicated with a plus sign (visible) or a minus sign (not visible).

The last column of table 5 gives an (subjective) indication of the quality of the image as far as the visibility of bottom topography is concerned : '++' means very good, '+' means good, '0' means fair and '-' stands for bad.

Image number	Bollen van Goeree	Oosterhinder	Banjaard Noordland Hompels	Middelbank	Steenbanken	Sand waves	Quality
1	?	+	+	?	?	-	0
2	+	+	+	+	+	+	++
3a	-	-	-	?	?	-	-
3b	-	+	+	+	?	-	0
3c	?	?	?	?	?	-	-
3d	?	+	?	?	?	+	+
4a	?	?	?	?	?	-	+
4b	?	+	?	?	?	-	+
5a	?	?	?	?	?	-	0
5b	?	?	+	?	?	-	0
6	?	?	+	?	?	-	0
7a	?	?	+	?	?	-	0
7b	-	+	+	+	+	+	++
8a	?	?	+	?	?	+	0
8b	?	?	?	?	?	+	0
8c	?	?	+	+	+	+	+
9a	?	?	?	?	?	-	-
9b	+	?	?	?	?	-	0
9c	?	?	+	?	?	-	0
10a	+	?	?	?	?	-	0
10b	+	?	+	?	?	+	+

Table 5. Visibility of bottom topography.

Besides the structures mentioned before a number of images also show other bottom features like sand banks West of Goeree, 'Rassen' near Westkapelle and 'Bankje van Zoutelande' Southwest of Walcheren. These structures are not included in table 5. However, their visibility is included in the indication of the quality of the images.

The images made at a wind speed between 4 and 8 m/s (3 - 4 Bft) show more details than those at higher winds. Note that the wind speeds given here can be too low due to the bad positioning of the anemometer at LEG, as stated before. Therefore the optimum wind speed can be somewhat higher. It is estimated between 4 and 10 m/s (3 - 5 Bft), in agreement with the value found with the old EMI SLAR. It has been mentioned in the literature (Alpers and Hennings, 1984 ; van Gastel, 1987a) that bottom topography can be mapped with imaging radar when the wind speed is between 2 and 10 m/s

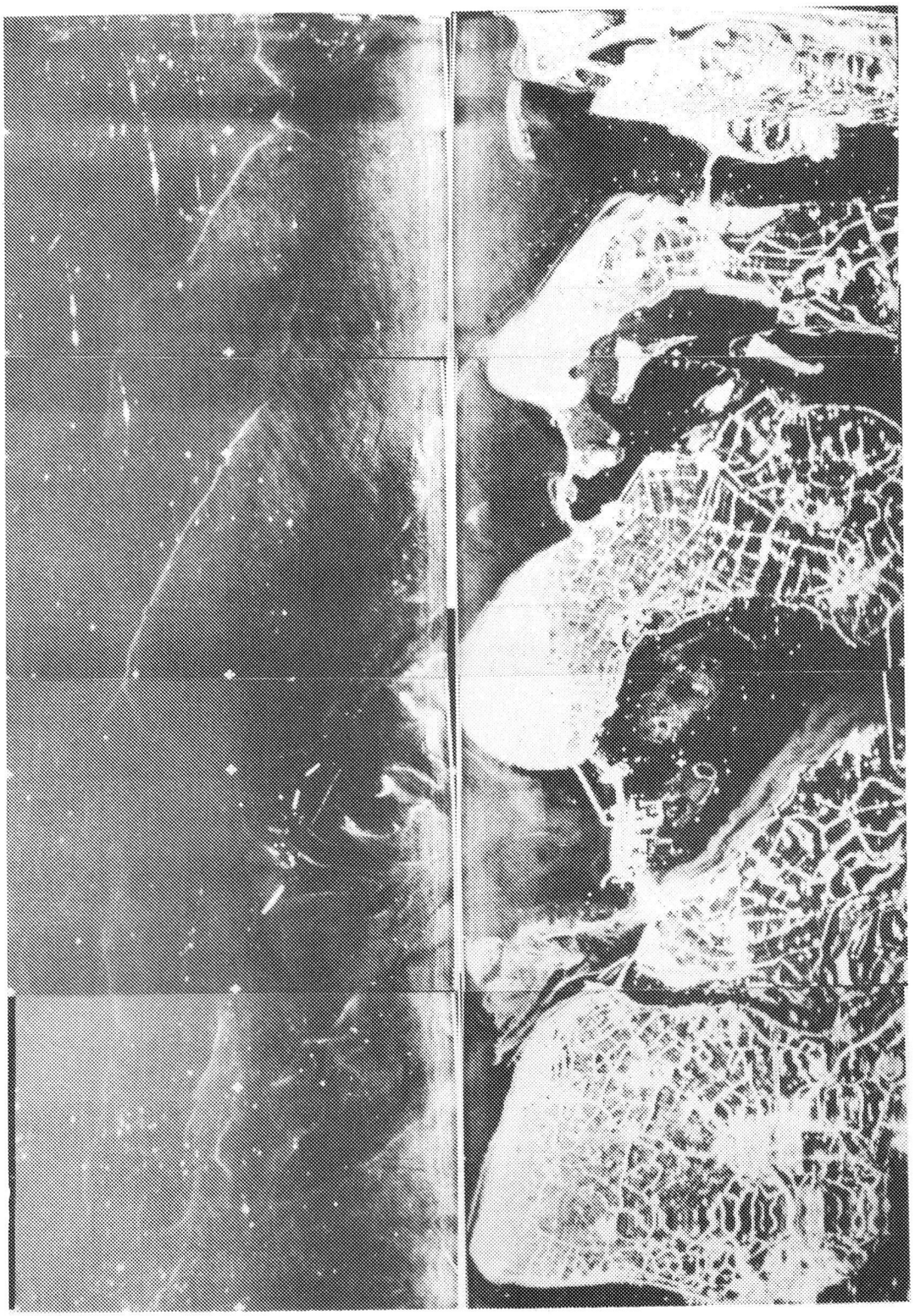

Figure 1. 'Oil-SLAR' image 2, recorded March 3, 1986. Both flight and current direction are from top to bottom.

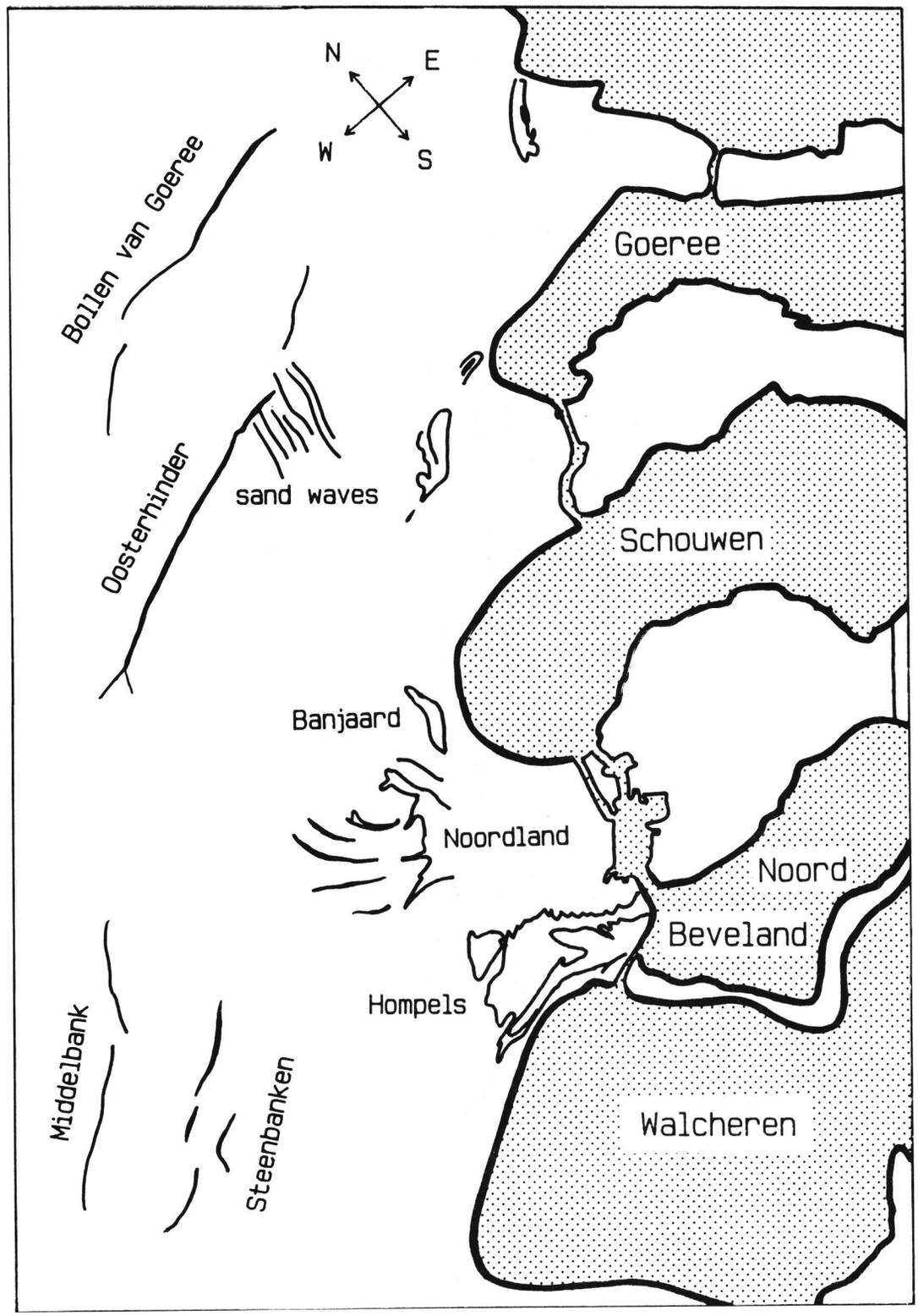

Figure 2. Some features visible in figure 1.

(1 - 5 Bft). However, large banks like 'Middelbank' and 'Steenbanken' are visible even at higher wind speed (12 - 14 m/s, 6 Bft; image 8c). Apparently the visibility of bottom topography slowly decreases with increasing wind speed. This view is supported by model calculations presented in chapter 3. It would be interesting to make some images at lower (1 - 2 Bft) and higher (6 - 7 Bft) wind speeds.

As already stated before, the sensitivity of the radar system is an important factor in stating the optimum wind speed for imaging bottom topography. Therefore it can not be concluded that also for the Dutch Digital SLAR the optimum wind speed will be 4 - 10 m/s (3 - 5 Bft).

2.6 Discussion

The relevant data are summarized in table 6. The indication of the quality of the images is identical to that used in table 5 (see section 2.5).

Image number	Heading	Wind dir.	Wind speed (Bft)	Quality
1	NE	W	5	0
2	SW	NE	3	++
3a	SW	SE	4	-
3b	NE	SE	4	0
3c	SE	SE	4	-
3d	NW	SE	4	+
4a	SW	N	3	+
4b	NW	N	4	+
5a	SW	SW	5	0
5b	NE	SW	5	0
6	SW	NW	5	0
7a	SW	W	3	0
7b	NE	W	3	++
8a	SW	N	5	0
8b	NW	N	6	0
8c	NE	N	6	+
9a	SW	S	6	-
9b	NE	S	6	0
9c	NW	S	6	0
10a	SW	N	4	0
10b	NW	N	4	+

Table 6. Summary.

The current velocity for all images is between 0.4 and 1.1 m/s. It is mentioned in the literature (Alpers and Hennings, 1984 ; van Gastel, 1987a) that bottom topography can be made visible with imaging radar when the current velocity equals 0.5 m/s or more. It should be noted that not the

magnitude of the current velocity itself determines the visibility of bottom topography, but the magnitude of the modulation in the current velocity (see chapter 3). However, the modulation in the current velocity due to bottom topography increases with increasing current velocity. As far as the current velocity is concerned, all images were made during favorable conditions.

According to the theory of Alpers and Hennings (1984) a sand bank parallel to the current direction is not visible. This is due to their supposition that the component of the current velocity parallel to the bank direction is constant. This does not hold in reality, because of the visibility of 'Middelbank' and 'Steenbanken' in images 2, 7b and 8c. It should be noted that these banks are not as well visible as 'Oosterhinder' and 'Bollen van Goeree', which make a larger angle with the current velocity.

Since the radar range direction is both to the left and to the right of the aircraft, dependence of the quality of the image on the angle between wind and flight direction must be visible in any image, especially those with the range in the upwind/downwind direction. There is no sign of any such dependence, in contrast with the old measurements using the EMI SLAR.

2.7 Conclusions

From the evaluation of the 'oil-SLAR' images the following conclusions are drawn :

1. During high and low tide at Hoek van Holland, when the current velocity reaches its maximum value in the area off the coast of Zeeland and Zuid Holland according to the current atlas, the situation is favorable for imaging bottom topography as far as the current velocity is concerned.
2. There is no sign of any dependence of the quality of the images on the wind and flight direction.
3. The optimum wind speed for imaging bottom topography with the 'oil-SLAR' is estimated between 4 and 10 m/s (3 - 5 Bft). The visibility of bottom topography decreases slowly with increasing wind speed, large banks being visible even at 12 - 14 m/s (6 Bft) or more.
4. Since the optimum wind speed depends on the sensitivity of the radar system, the optimum wind speed of 4 - 10 m/s (3 - 5 Bft) for mapping bottom topography with the 'oil-SLAR' can not be applied directly to the Dutch Digital SLAR.

It is recommended that some 'oil-SLAR' images are made at lower (1 - 2 Bft) and higher (6 - 7 Bft) wind speeds to gain more insight in the effect of the wind speed, and at other tidal phases to study the effect of the current velocity.

3 THEORY

3.1 Introduction

The theory of the imaging mechanism for mapping sea bottom topography with SLAR and SAR is described in this chapter. Though this chapter is technical in nature, the reader is advised to study the introduction and the conclusions in order to appreciate the subsequent chapters.

Several theories have been proposed to describe the imaging mechanism. It is now generally accepted that this mechanism consists of three steps :

1. Interaction between tidal flow and bottom topography produces variations in the current velocity at the sea surface. This is usually described with the continuity equations (mass conservation).
2. Variations in the surface current velocity give rise to modulations in the wind generated spectrum of water waves as described by the action balance equation.
3. Modulations in the wave spectrum cause spatial variations in the radar backscatter. The relation between the sea surface and the radar cross section is generally described using first order Bragg scattering.

Models of this kind have been proposed by Hughes (1978), Alpers and Hennings (1984), Phillips (1984), Shuchman, Lyzenga and Meadows (1985), Holliday, St-Cyr and Woods (1986) and van Gastel (1987a). Internal waves also cause variations in the surface current velocity, and therefore the second and third step of the mechanism outlined above is used to describe their signature in radar images. The central point in these models is the effect of the surface current velocity on the wave spectrum, described by the action balance equation.

The simplest model is the one by Alpers and Hennings (AH, 1984). They assume that variations in the surface current velocity lead to only small deviations of the wave spectrum from equilibrium. In a first order perturbation scheme, using constant relaxation rate and neglecting advection they arrive at an analytical solution of the action balance equation. Recently they extended their model to include advection for a harmonic variation in the surface current velocity (Hennings, 1988).

Shuchman, Lyzenga and Meadows (SLM, 1985) solve the action balance equation numerically using the source function given by Hughes (1978). With this source function also an analytical solution can be found (Hughes, 1978 ; Hennings, 1988).

Holliday, St-Cyr and Woods (HSW, 1986) use a model similar to that of Alpers and Hennings but with a relaxation rate that is a function of wave number and wind speed. They also include other scattering mechanisms than first order Bragg, by employing a backscatter model based on the Stratton-Chu integral equation.

Van Gastel (1987a) includes the effects of wind input, dissipation and nonlinear wave-wave interactions in a rigorous way. The action balance equation is solved numerically. Since only triad wave-wave interactions are taken into account, this model is restricted to X-band.

The models described above predict different values not only for the magnitude of the modulation in the radar backscatter but also for the position of this modulation relative to the bottom topography. The latter quantity is crucial if radar images are to be used for cartographic purposes. It is often expressed as a phase shift between the maximum radar backscatter and the maximum current velocity (minimum depth).

The predictions of the models are summarized in table 7. The precise values of the modulation and the phase shift depend on bottom shape, current velocity and wind speed.

Authors	Modulation		Phase shift	
	L-band	X-band	L-band	X-band
AH, 1984	0.1	0.01	90°	90°
SLM, 1985	0.1	0.01	110° - 150°	100°
HSW, 1986	0.1	0.1	110° - 150°	100°
van Gastel, 1987a	-	1000	-	150° - 210°
Hennings, 1988	0.1	0.1	100° - 150°	100°

Table 7. Predictions of some models of the modulation (order of magnitude) and the phase shift at L- and X-band.

At L-band all models (except that of van Gastel which is restricted to X-band) predict modulations in the radar backscatter of the order of 10%. The modulations calculated for a number of cases are generally in good agreement with the SEASAT L-band data (AH, 1984 ; SLM, 1985 ; Hennings, 1988). AH predict a phase shift of 90°, because in their model advection is neglected. Therefore the modulation in the radar backscatter is proportional to the gradient in the surface current velocity and thus, using the continuity equations, to the depth gradient. Advection, included in the other models, increases the phase shift. The accuracy in position of all radar images, including SEASAT, is not good enough for a precise determination of the phase shift.

At X-band the results of the SARSEX experiment indicate that the modulation is of the same order of magnitude as that at L-band (Apel et al., 1985). In that case the models of AH and SLM underestimate the modulation at X-band by an order of magnitude (HSW, 1987). By employing other scattering mechanisms than first order Bragg, like a scattering model based on the Stratton-Chu integral equation (HSW, 1987) or a two-scale model (Hennings, 1988) the modulation is increased to the correct order of magnitude. According to all models except that of van Gastel, advection is not very important at X-band. This is due to the fact that the relaxation rate at X-band is much larger than at L-band, causing the wave spectrum to return much faster to its equilibrium. Therefore advection has little effect at X-band.

Van Gastel predicts very high modulations at X-band for low wind speeds. This modulation is always negative, in contrast with the other models. The phase shift is around 180°, so the maximum backscatter is located at the minimum current velocity (maximum depth if the continuity equations are used). These predictions agree with measurements by Kwoh, Lake and Rungaldier (1986). Experiments with X-band SLAR at higher wind speeds, however,

indicate that the phase shift is close to 90° and that both positive and negative modulations occur (de Loor, 1981 ; chapter 6 of this work).

In this chapter a description of the simple models will be given. Section 3.2 is devoted to the derivation of the continuity equations, which describe the relation between current velocity and depth in the most simple way, starting from the general Navier-Stokes equations.

The action balance equation and three models for its source term (AH, SLM and HSW) are described in section 3.3. These models will be referred to as simple relaxation models. Also a short derivation of the solution of the action balance equation without advection is given.

Section 3.4 deals with the radar cross section of the sea surface. First order Bragg scattering and two scale models are presented. Their validity at conditions encountered on sea is discussed. Also some attention is paid to the influence of the current on the shape of the sea surface. It is shown that this effect can be neglected.

The action balance equation has been solved numerically in one dimension for the three source terms mentioned above using the method of characteristics (Hughes, 1978 ; Phillips, 1984). These calculations were performed for situations that can occur in sand wave area's off the Dutch coast. The results are presented in section 3.5. It will be shown that advection can be important, notably at L-band for features smaller than 1 km, and that all three models for the source term give similar results. More elaborate calculations and information about the method of solution can be found in Vogelzang (1988).

3.2 Current velocity

The depth averaged flow over a bottom topography can be described by the continuity equation and the momentum equations (Navier-Stokes equations) as follows

$$\frac{\partial(hU_x)}{\partial x} + \frac{\partial(hU_y)}{\partial y} = 0 \quad , \tag{1}$$

$$U_x \frac{\partial U_x}{\partial x} + U_y \frac{\partial U_y}{\partial y} + g \frac{\partial \xi}{\partial x} - g\, s_x + \frac{\tau_{bx}}{\rho h} = 0 \quad , \tag{2a}$$

$$U_x \frac{\partial U_y}{\partial x} + U_y \frac{\partial U_y}{\partial y} + g \frac{\partial \xi}{\partial y} - g\, s_y + \frac{\tau_{by}}{\rho h} = 0 \quad , \tag{2b}$$

where x and y are the horizontal spatial coordinates as shown in figure 3, U_x and U_y are the velocity components in x- and y-direction, g is the gravitational acceleration, ρ the mass density of the fluid, ξ the elevation of the water surface and h the local water depth, while s_x and s_y are the slopes of the coordinate system in x- and y-direction and τ_{bx} and τ_{by} are the components of the bottom shear stress in x- and y-direction. The following expression can be derived for the components of the bottom shear stress

$$\tau_{bx} = \frac{\rho g}{C^2} U U_x = \rho h r U_x \quad , \tag{3a}$$

$$\tau_{by} = \frac{\rho g}{C^2} U U_y = \rho h r U_y \quad , \tag{3b}$$

where U is the magnitude of the velocity ($U^2 = U_x^2 + U_y^2$), C is Chezy's factor and r the bottom shear stress factor ($r = gU/C^2h$)

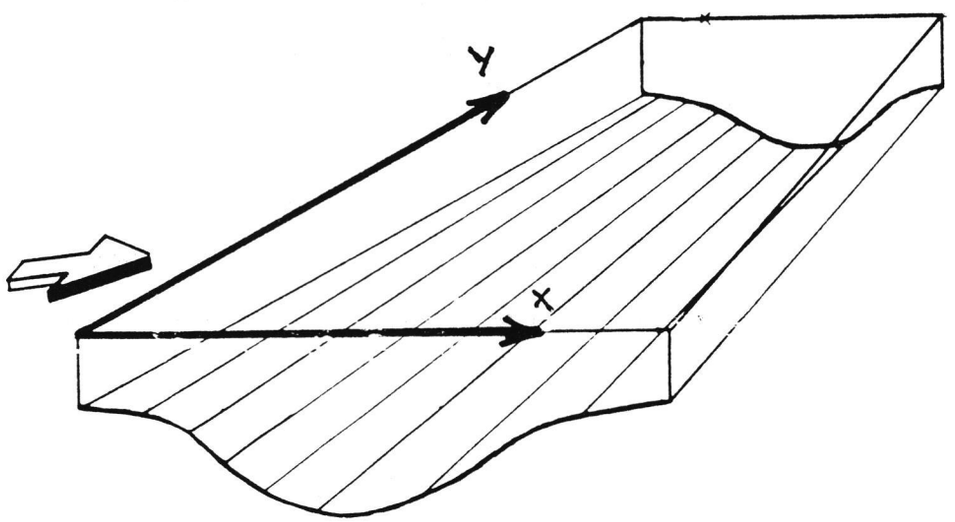

Figure 3. Definition of the coordinate system.

In the mathematical formulation of the convection terms in the momentum equations, (2a) and (2b), and the definition of the bottom shear stress components according to equations (3a) and (3b) the influence of secondary flow effects are left out of consideration. For a first approximation of the depth averaged flow field this simplification seems to be justified.

Eliminating the pressure gradient terms from equations (2a) and (2b) leads to the vorticity transport equation

$$U_x \frac{\partial \Omega_v}{\partial x} + U_y \frac{\partial \Omega_v}{\partial y} - \frac{\Omega_v}{h}\left[U_x \frac{\partial h}{\partial x} + U_y \frac{\partial h}{\partial y} \right] + r\Omega_v = U_y \frac{\partial r}{\partial x} - U_x \frac{\partial r}{\partial y} \quad , \tag{4}$$

with the vorticity Ω_v defined by

$$\Omega_v = \frac{\partial U_x}{\partial y} - \frac{\partial U_y}{\partial x} \quad . \tag{5}$$

The bottom topography is now assumed to be formed by sand waves that are infinitely long in the direction parallel to the their crests (y-direction), as indicated in figure 3. Therefore the flow is uniform in that direction and the vorticity transport equation (4) can be simplified to

$$U_x \frac{d\Omega_v}{dx} - \frac{\Omega_v}{h} U_x \frac{dh}{dx} + r\Omega_v = U_y \frac{dr}{dx} \quad , \tag{6}$$

or, equivalently

$$\frac{d\Omega_v}{dx} = \frac{\Omega_v}{h}\frac{dh}{dx} - \frac{r}{U_x}\Omega_v + \frac{U_y}{U_x}\frac{dr}{dx} \quad . \tag{7}$$

Moreover, the continuity equation (1) reduces to

$$\frac{d(hU_x)}{dx} = 0 \quad . \tag{8}$$

In equation (7) the effects of both convective inertia and bottom resistance are incorporated. An estimate of the order of magnitude of both terms can be obtained from the momentum equations

$$\frac{\text{convective inertia}}{\text{bottom resistance}} = \frac{\tan(\beta)}{g/C^2} \quad , \tag{9}$$

where β is the local bottom slope. As can be seen from equation (9), the flow pattern is dominated by convective inertia in a situation with relatively steep bottom slopes while bottom resistance is important as well in a situation with mild slopes. It is assumed that for sand waves the former process is dominant. In this case equation (7) reduces to

$$\frac{d\Omega_v}{dx} - \frac{\Omega_v}{h}\frac{dh}{dx} = \frac{d}{dx}\left[\frac{\Omega_v}{h}\right] = 0 \quad . \tag{10}$$

In case of uniform flow this equation is satisfied when $\Omega_v = 0$. Then equation (8) implies that the flow field above the sand waves behaves in the following way

1. the velocity component perpendicular to the sand waves is inversely proportional to the depth.
2. the velocity component parallel to the sand waves is constant.

This can be written in the form used by e.g. Alpers and Hennings (1984)

$$U_x = C_{per}/h \quad , \tag{11a}$$

$$U_y = C_{par} \quad , \tag{11b}$$

where C_{per} and C_{par} are constants. From equations (11a) and (11b) the gradient in the current velocity is readily found to be

$$\frac{dU_x}{dx} = - \frac{C_{per}}{h^2} \frac{dh}{dx} \qquad (12)$$

To include the effect of surface wind on the current and to give information about the current profile a transformation technique can be used by which the distributions of the (tidal or wind induced) current velocities over the depth can be extracted at any horizontal position from depth averaged flow data (Davies, 1987, 1988).

3.3 The action balance equation

The evolution of the action spectrum A is described by the action balance equation (Hasselmann, 1960 ; Willebrand, 1975). In one dimension and for stationary current this equation reads

$$\frac{\partial \Omega(k,x)}{\partial k} \frac{\partial A(k,x)}{\partial x} - \frac{\partial \Omega(k,x)}{\partial x} \frac{\partial A(k,x)}{\partial k} = S(k,x) \quad , \qquad (13)$$

where x is the position, k the wave number and S the source function describing the combined effect of wind input, dissipation and wave-wave interactions. The first term on the left hand side is called the advection term, the second the refraction term. The apparent frequency Ω is given by

$$\Omega(k,x) = \omega(k) + k\, V(x) \quad , \qquad (14)$$

with V the surface current velocity (which is a function of position now) and ω the intrinsic frequency which obeys

$$\omega(k) = [g\, k + \gamma\, k^3]^{1/2} \quad , \qquad (15)$$

g being the gravitational acceleration and γ the ratio of the surface tension and the water density. From (14) one gets, assuming that the surface current velocity obeys the continuity equations

$$\frac{\partial \Omega(k,x)}{\partial x} = k \frac{dV(x)}{dx} \quad , \qquad (16a)$$

$$\frac{\partial \Omega(k,x)}{\partial k} = c_g(k) + V(x) \quad , \qquad (16b)$$

where $c_g = d\omega/dk$ is the group velocity of the water waves. The action spectrum is related to the energy spectrum E by

$$A(k,x) = \frac{E(k,x)}{\omega(k)} \quad . \qquad (17)$$

The source function S used by AH (1984) is linear in the action spectrum. It is given by

$$S(k,x) = -\mu\,[A(k,x) - A_0(k)] \quad , \tag{18}$$

where A_0 is the equilibrium action spectrum and μ the relaxation rate. The relaxation rate is the crucial parameter. Because it is not well known it is considered as an adjustable constant parameter in the work of AH. The effect of this source function is to drive the spectrum back to its equilibrium value at a rate controlled by μ. The inverse of μ is the relaxation time τ_r, which for SEASAT L-band is expected to be of the order of 10 - 100 Bragg wave periods.

AH solve the action balance equation (13) by supposing

$$A(k,x) = A_0(k) + \delta A(k,x) \quad , \tag{19a}$$

$$V(x) = V_0 + \delta V(x) \quad , \tag{19b}$$

where δA and δV are small compared to A_0 and V_0 respectively. Substituting (18), (19a) and (19b) in (13), using (16a) and (16b), and neglecting terms of second order in δA and δV they arrive at

$$\left[(c_g(k) + V_0)\,\frac{\partial}{\partial x} + \mu\right]\delta A(k,x) = k\,\frac{dV(x)}{dx}\,\frac{dA_0(k)}{dk} \quad . \tag{20}$$

The advection time τ_a is defined as

$$\tau_a = [(c_g + V_0)\,K]^{-1} \quad , \tag{21}$$

where K is the wave number of the bottom topography and, therefore, of the current velocity variation. AH assume that $\tau_a \gg \tau_r$, equivalent to

$$(c_g + V_0)\,K \ll \mu \quad . \tag{22}$$

Note that in their paper this condition, their equation (32), is misprinted. Taking $K = 2\pi/b$, b the length of the current velocity variation, and supposing V_0 to be of the same order of magnitude as c_g, this assumption is correct if μ or b is large. Under this assumption AH neglect the advection term (the first term on the left hand side of (20)). With a Phillips equilibrium spectrum of the form

$$E_0(k) = \omega(k)\,A_0(k) = a\,k^{-4} \quad , \tag{23}$$

a being the Phillips constant, they arrive at

$$\delta A(k,x) = -\frac{4 + c_g/c_p}{\mu}\,A_0(k)\,\frac{dV(x)}{dx} \quad , \tag{24}$$

where $c_p = \omega/k$ is the phase speed of the waves. Substitution of (12) for the derivative of the current velocity (assuming that the surface current velocity also satisfies the continuity equations) yields their final

result, the modulation in the action spectrum being proportional to the gradient in the current velocity. Recently AH have extended their model to include advection (Hennings, 1988). Since their model is analytical rather than numerical they are able to include advection for harmonic variations in the surface current velocity as a function of position only. They still have to neglect terms of second order in δA and δV.

SLM use a source function that is quadratic in the action spectrum. It is given by

$$S(k,x) = \mu(k)\, A(k,x)\, [1 - A(k,x)/A_0(k)] \quad . \tag{25}$$

Here the relaxation rate μ (or wave growth rate parameter) is a function of wave number and wind speed. As already mentioned, the relaxation rate is not well known. Hughes (1978) has reviewed and parametrized the available measurements. For waves travelling into the same direction as the wind, the case considered in this work, his parametrization reads

$$\mu(k) = \omega(k)\, u_*/c_p \,\{0.01 + 0.016\, u_*/c_p\} \{1 - \exp[-8.9(u_*/c_p - 0.03)^{1/2}]\} \quad , \tag{26}$$

where u_* is the friction wind velocity. Note that the relaxation rate vanishes for $u_* \leq 0.03\, c_p$. For neutral stability the friction wind velocity can be related to the wind speed u_z relative to the water by

$$u_z = \frac{u_*}{\kappa} \ln \frac{z}{z_0} \quad , \tag{27}$$

where κ is von Karman's constant, z the anemometer height and z_0 the roughness length. SLM and Hughes use the parametrization of the roughness length given by Inoue (1967), which in SI units reads

$$z_0 = 0.001\, (0.0684/u_* + 4.28\, u_*^2 - 0.443) \quad . \tag{28}$$

One could also use the parametrization given by Garratt (1977), the form of which was originally proposed by Charnock (1955)

$$z_0 = \frac{0.0144}{g}\, u_*^2 \quad . \tag{29}$$

Figure 4 shows the wave growth rate μ as a function of u_{10}, the wind speed relative to the water at 10 m anemometer height, for $k = 30\ m^{-1}$ and $k = 300\ m^{-1}$. From figure 4 one can see that μ is a rapidly varying function of U_{10} and that the two parametrizations of the roughness length give similar results. For the von Karman constant κ a value of 0.40 was adopted.

HSW (1986) use the same source function as AH, but include the wave number and wind speed dependence in the relaxation rate following SLM and Hughes.

It should be noted that substitution of (19a) into (25), the source function used by SLM, and neglecting terms quadratic in δA yields (18), the source function of HSW and AH, the only difference with AH being the form of the relaxation rate. Thus one expects that for small modulations in the

action spectrum, which occur for large values of the relaxation rate, the models of AH, HSW and SLM will give similar results, since the source functions will almost be the same. On the other hand the source functions will also be the same when the relaxation rate approaches zero. Differences between the models of AH, HSW and SLM are therefore expected to occur at intermediate values of the relaxation rate where advection is neither dominant nor negligible.

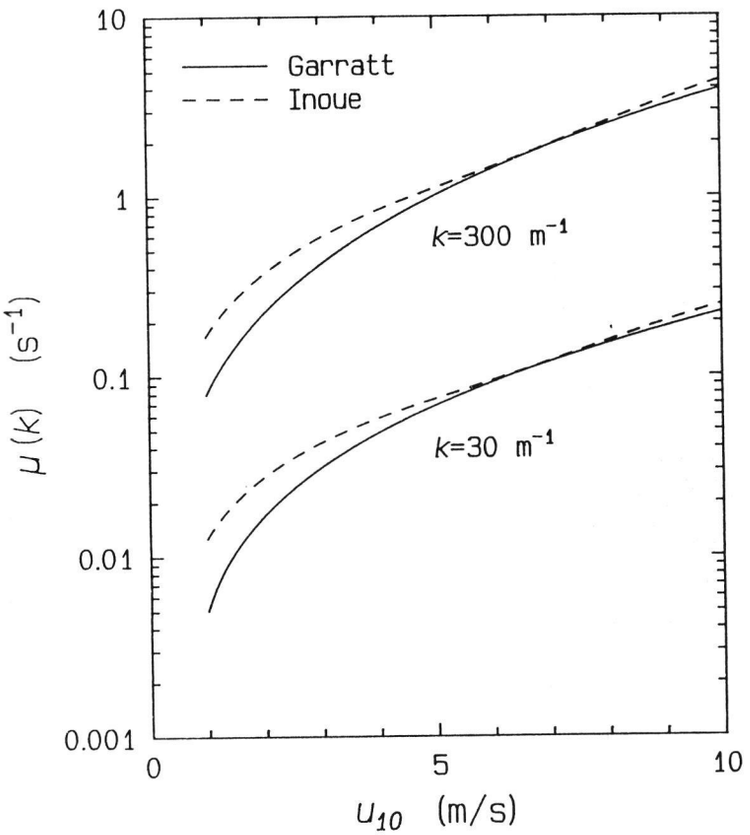

Figure 4. The relaxation rate or wave growth rate μ as a function of the wind speed at 10 m anemometer height relative to the water u_{10} according to Hughes with the parametrizations of the roughness length given by Garratt and Inoue. The lower curves are at L-band, the upper at X-band.

3.4 Radar cross section

The most widely used models for the description of the radar cross section of the sea surface σ_0 at angles of incidence between 20° and 70°, the range of interest for this work, are first order Bragg scattering and two scale models. For small angles of incidence (0° - 10°) Kirchhoff scattering, also known as specular reflection, can be used (Barrick, 1968). At grazing angles shadowing effects become important. A review of the

scattering models is given by Valenzuela (1978).

For first order Bragg scattering, also called slightly rough surface scattering or wave-wave model, the radar cross section of the sea σ_0 reads (Valenzuela, 1978)

$$\sigma_0(\theta)_{pq} = 4\pi\,(k\cos(\theta))^4\,|g_{pq}(\theta)|^2\,W(k_B,0) \quad . \tag{30}$$

Here p is the polarization of the incoming radar radiation and q that of the backscattered radiation. The incoming radiation is in the x-z plane, z being the vertical direction and x, y the horizontal coordinates. θ is the angle of incidence and k the wave number of the radar radiation. W is the two-dimensional wave number spectral density of the sea surface roughness and k_B the Bragg wave number given by

$$k_B = 2\,k\,\sin(\theta) \quad . \tag{31}$$

The functions g are in first order

$$g_{vv}(\theta) = \frac{(\varepsilon_r - 1)[\varepsilon_r(1 + \sin^2(\theta)) - \sin^2(\theta)]}{[\varepsilon_r\cos(\theta) + (\varepsilon_r - \sin^2(\theta)^{1/2}]^2} \quad , \tag{32a}$$

$$g_{hh}(\theta) = \frac{(\varepsilon_r - 1)}{[\varepsilon_r\cos(\theta) + (\varepsilon_r - \sin^2(\theta)^{1/2}]^2} \quad , \tag{32b}$$

$$g_{vh}(\theta) = g_{hv}(\theta) = 0 \quad , \tag{32c}$$

where h and v stand for horizontal and vertical polarization respectively and ε_r is the complex relative dielectric constant of the sea. The relative permeability of the sea μ_r is set equal to 1. In first order there is no cross polarized backscatter. A clear derivation of these formulas can be found in Ulaby, Moore and Fung (1982). Second order Bragg scattering is treated by Valenzuela (1967) and Fung (1968).

Assuming first order Bragg scattering the dominant mechanism, equations (30) and (31) show that the radar cross section of the sea is proportional to the wave height spectrum at the Bragg wave number, which is of the same order of magnitude as the wave number of the radar radiation. For L-band radar the Bragg wave number is of the order of 30 cm, for X-band of the order of 3 cm.

In the presence of longer waves (e.g. swell) the local angle of incidence varies due to the tilting effect of the longer waves. This effect is incorporated in two scale models (also called wave-facet models or composite surface scattering models) as follows (Valenzuela, 1978)

$$\sigma_0^{SEA}(\theta)_{pq} = \int_{-\infty}^{\infty} d(\tan\alpha_i) \int_{-\infty}^{\infty} d(\tan\beta_i)\;\sigma_0(\theta_i)_{pq}\;P(\tan\alpha_i,\tan\beta_i) \quad , \tag{33}$$

where P is the joint probability density of slopes for the large scale roughness of the sea. The angle between the vertical and the normal of the sea surface is α_i in the plane of incidence and β_i in a plane perpendicular

to the plane of incidence. The local angle of incidence θ_i is given by

$$\cos(\theta_i) = \cos(\theta + \alpha_i)\cos(\beta_i) \quad . \tag{34}$$

The local cross section for a tilted patch is given by $\sigma_0(\theta_i)$ and can be related to equations (30), (31) and (32) for Bragg scattering (Valenzuela, 1978).

Two scale models combine Bragg scattering and Kirchhoff scattering in a rather ad hoc way. For seas at higher winds the wave spectrum has to be separated into a short wave part and a long wave part. There is no sound criterium at which wave number this separation should be made. Moreover, Bragg scattering is valid only if the amplitudes and slopes of the sea waves are small. In practice, the use of Bragg scattering often can not be justified because the amplitudes of the waves are too large. Nevertheless Bragg scattering and two scale models give a satisfactory description of the experimental data. A more fundamental approach to electromagnetic scattering from the sea surface which avoids these problems would be the solution of the Stratton-Chu integral equation, which can be derived directly from the Maxwell equations (Stratton, 1941 ; Holliday, 1986).

Another possible mechanism that might cause tilt modulation is the change of the mean sea level with current velocity. This effect can be estimated with Bernouilli's law in the form

$$1/2\ U^2 + g\,\xi = \text{constant} \quad , \tag{35}$$

where U is the current velocity, g the gravitational acceleration and ξ the sea level. Suppose that at position 1 the depth equals h_0 and the sea level ξ_0, while at position 2 the depth equals $h_0 + \delta h$ and the sea level $\xi_0 + \delta\xi$, the current velocity directed along the line connecting positions 1 and 2. Equating (35) for positions 1 and 2 the value of $\delta\xi$ is found to be

$$\delta\xi = \frac{U_2^2 - U_1^2}{2g} \quad . \tag{36}$$

Using the continuity equation (11b) to relate U_2, the current velocity at position 2 to U_1, the current velocity at position 1, U_2 reads

$$U_2 = U_1\,(1 + \delta h/h_0 + \delta\xi/\xi_0) \approx U_1\,(1 + \delta h/h_0) \quad , \tag{37}$$

the approximation being justified if $\delta\xi/\xi_0$ is much smaller than $\delta h/h_0$. Substitution of (37) in (36), neglecting terms quadratic in δh, finally yields

$$\delta\xi = \frac{U_1^2\,\delta h}{g\,h_0} \quad . \tag{38}$$

When (38) is evaluated with values found in the test area of the main experiment (U_1 = 0.75 m/s, δh = 6 m, h_0 = 20 m and g = 10 m/s^2, see chapters 5 and 6) the value of $\delta\xi$ is 1.7 cm. With a maximum bottom slope of 0.15 for sand waves in the Southern Bight of the North Sea (Terwindt, 1971) the distance between the two points is 40 m, resulting in a maximum tilt angle of 0.027°. This variation in the local angle of incidence is much too

small to account for the observed modulations in the radar cross section. Therefore this effect can be safely neglected.

3.5 Model calculations

3.5.1 General

The action balance equation has been solved numerically using the method of characteristics or, equivalently, integration along energy paths (Hughes, 1978 ; Phillips, 1984). The advantage of a numerical solution is that the source terms employed by Alpers and Hennings (AH, 1984), by Shuchman, Lyzenga and Meadows (SLM, 1985) and by Holliday, St-Cyr and Woods (HSW, 1987) can be compared within the same model. Also it is possible to include advection into the AH model. Information about the algorithm used to solve the action balance equation and more elaborate calculations can be found in Vogelzang (1988).

The surface current velocity V used in this work is defined as

$$V(x) = V_0 + V_m \sin(2\pi x/b) \quad , \tag{39}$$

with V_0 = 1 m/s and V_m = 0.1 m/s. The algorithm can handle any other functional form of the current velocity. This form of V was chosen to facilitate comparison with other work, in particular the AH model including advection (Hennings, 1988). It was found that the numerical solution presented here is almost identical to the analytical solution of AH, the difference being due to second order terms neglected by them.

The value of V_m corresponds with current velocity modulations measured above sand waves in the North Sea (van Gastel, 1987b) ; V_0 is usually somewhat smaller (around 0.5 m/s at low tide and around 0.7 m/s at high tide). The current velocity modulation length b can be regarded as the wavelength of a specially shaped periodic bottom topography (or internal wave) causing a surface current velocity of the form (39). The relative variation in the current velocity ΔV is defined as

$$\Delta V(x) = \frac{V(x) - V_0}{V_0} \quad . \tag{40}$$

The calculations presented here were performed using g = 9.81 m/s^2 for the gravitational acceleration, τ = 0.07275 N/m for the surface tension and ρ = 1025 kg/m^3 for the sea water density.

3.5.2 Behavior of the action spectrum

Figure 5 shows ΔV and ΔA as a function of x for k = 30 m^{-1} and μ = 0.068674 s^{-1}, and for k = 300 m^{-1} and μ = 1.009323 s^{-1} using the source function of AH (17). ΔA is defined as the relative deviation of the action spectrum from its equilibrium value

$$\Delta A(k,x) = \frac{A(k,x) - A_0(k)}{A_0(k)} \quad . \tag{41}$$

The wave numbers correspond to the Bragg wave number of radar radiation with a wavelength of 30 cm (L-band) and 3 cm (X-band) respectively, incident to the sea surface under approximately 45°. The relaxation rate was calculated using the prescription of Hughes (26), with Garratt's wind profile, (27) and (29), at a wind speed of 5 m/s relative to the water at 10 m anemometer height. The relaxation rate was held constant during the calculation. At x = 0 the wave spectrum was set equal to the Phillips equilibrium spectrum. From figure 5 it appears that after a transient period, the length of which increases with decreasing relaxation rate, the spectrum reaches steady state. Note that the curve for ΔA at L-band is not symmetrical around zero, due to the terms of second order in δA and δV neglected by AH. This asymmetry increases with decreasing relaxation rate.

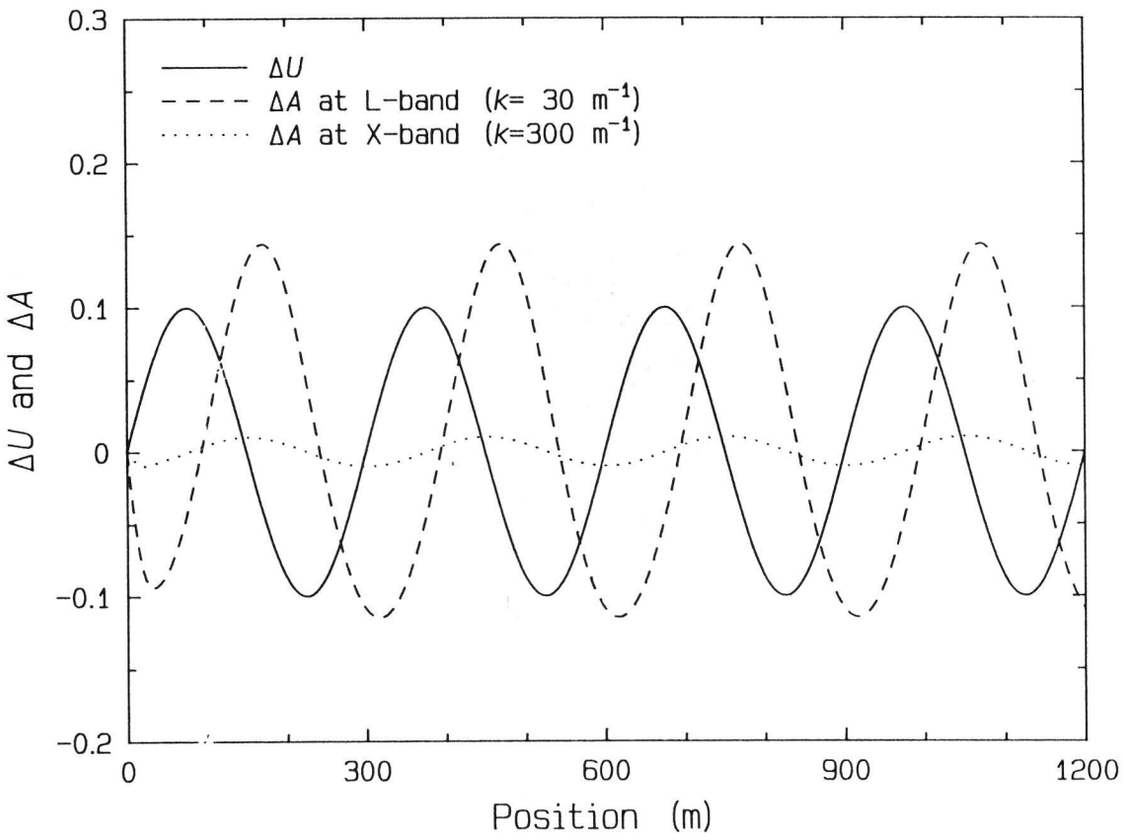

Figure 5. The modulations in the current velocity and in the action spectrum, ΔV and ΔA, as a function of position.

Though ΔA is not exactly a harmonic function, a phase shift φ and a modulation depth α are defined as

$$\varphi = (z_{max} - y_{max})\ 360°/b \quad , \tag{42a}$$

$$\alpha = (\Delta A_{max} - \Delta A_{min})/2 \quad , \tag{42b}$$

where ΔA_{max} and ΔA_{min} are the maximum and minimum value of ΔA, y_{max} is the position of a maximum in ΔV and z_{max} the position of the subsequent maximum in ΔA, moving in the direction of the current velocity.

Note that if first order Bragg scattering is the dominant scattering mechanism, the backscattered intensity is proportional to A evaluated at the Bragg wave number. In that case ΔA equals the relative modulation in the backscattered intensity.

3.5.3 Variation of wind speed and current modulation length

The next figures show the effect of wind speed and current modulation length. The parametrization of the roughness length given by Inoue (28), used by SLM and Hughes, gives almost the same results as that by Garratt (29) which is used in this work. Note that the source function of AH equals the source function used by HSW when the wave number and wind speed dependence of μ is included.

Figure 6a and 6b show the effect of w_{10}, the wind speed at 10 m anemometer height measured in the same frame as the current velocity. The current velocity modulation length b equals 300 m. The curves were obtained using the source functions at L-band ($k = 30\ m^{-1}$) and X-band ($k = 300\ m^{-1}$). The values of the relaxation rate for all curves in figures 6a and 6b were obtained from (26), (27) and (29). The relaxation rate was kept constant during the calculation for the curves labeled AH. For the solution of equations (26), (27) and (29) one needs the value of u_{10}, the wind speed relative to the water at 10 m anemometer height. Since wind and waves are travelling into the same direction here, the relation between u_{10} and w_{10} is

$$u_{10} = w_{10} - V_0 \quad , \tag{43a}$$

for constant relaxation rate μ (AH), and

$$u_{10} = w_{10} - V(x) \quad , \tag{43b}$$

for variable relaxation rate μ (SLM and HSW).

Figure 6a shows φ as a function of w_{10}. There is little difference between the three models. For large values of w_{10} (large values of μ) φ approaches 90°, the value predicted by AH. For smaller values of w_{10} (smaller values of μ) φ increases and becomes 180° when μ equals zero, due to advection. At X-band this effect is unimportant, φ being close to 90°. Advection can be neglected unless the wind speed is very small, in which case the phase shift rises rapidly to 180°. At L-band, however, the effect is much stronger and advection must be included.

Figure 6b shows α as a function of w_{10}. For α it makes no difference which model for the source term is used. The modulation at X-band is an order of magnitude smaller than that at L-band. Note that according to AH α will go to infinity for very low winds when μ approaches zero. Advection, however, keeps α at finite value when μ vanishes.

Figures 7a and 7b show the effect of variation of the current modulation length b. The wind speed relative to the water was set equal to 5 m/s, corresponding to $w_{10} = 6$ m/s.

Figure 7a shows φ as a function of b. Again the three models for the source function give similar results. Advection is unimportant at X-band, φ being close to 90°. At L-band advection must be included since φ rises

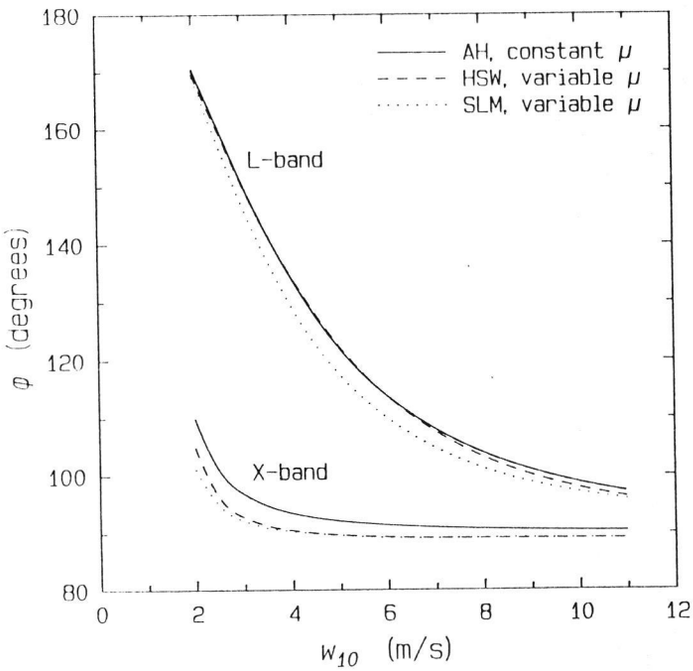

Figure 6a. The phase shift φ as a function of the wind speed at 10 m anemometer height w_{10}.

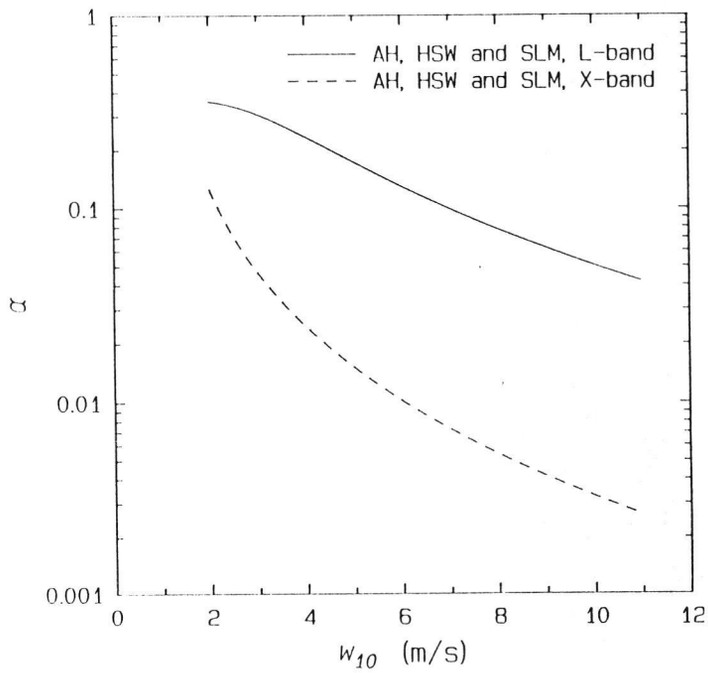

Figure 6b. The modulation depth α as a function of the wind speed at 10 m anemometer height w_{10}.

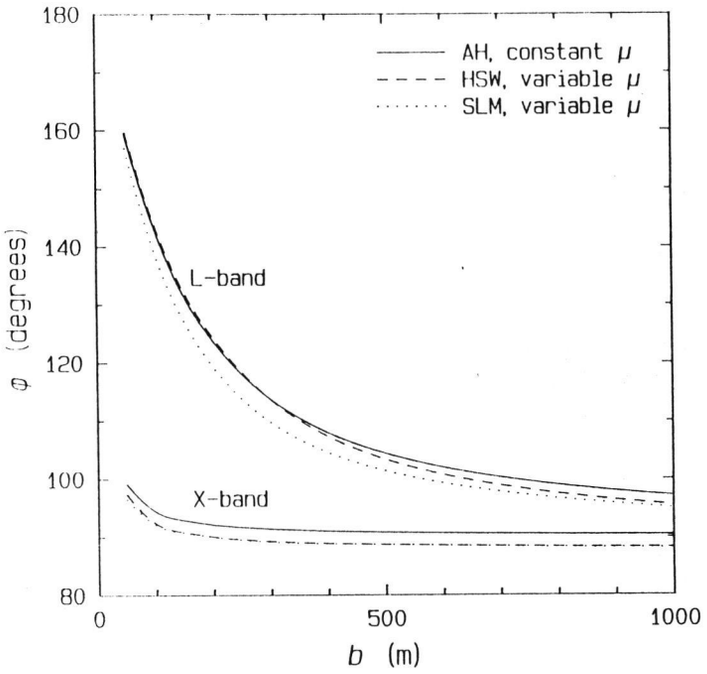

Figure 7a. The phase shift φ as a function of the current modulation length b for constant and variable relaxation rate μ.

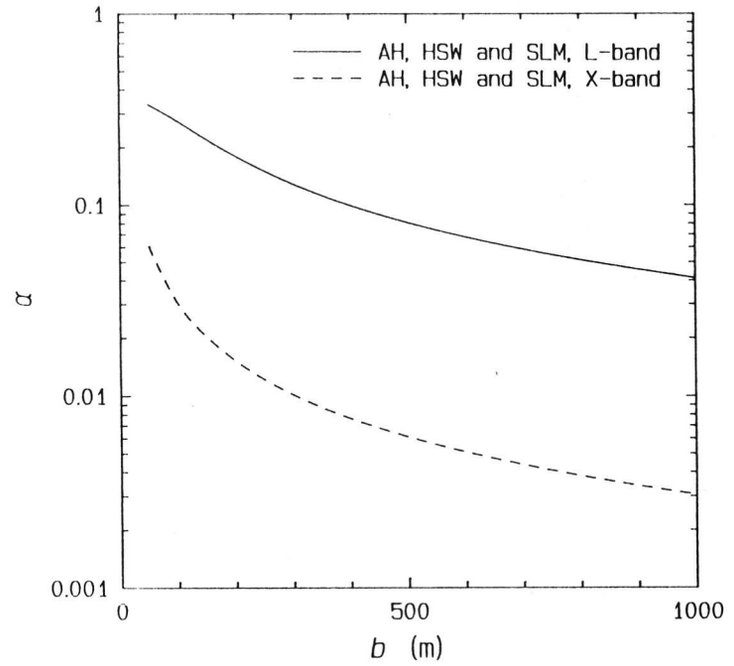

Figure 7b. The modulation depth α as a function of the current modulation length b for constant and variable relaxation rate μ.

strongly with decreasing b.

Figure 7b shows α as a function of b for the three source terms. For α it makes no difference which source term is used. From figure 7b it can be seen that α rises with decreasing b, due to the fact that the gradient of the current velocity increases.

3.6 Conclusions

The action balance equation was solved numerically using the method of characteristics. The model constructed thus is not restricted to any specific form of the surface current velocity or the source function. It therefore allows inclusion of the source functions used by Alpers and Hennings (1984), Shuchman, Lyzenga and Meadows (1985) and Holliday, St-Cyr and Woods (1986). The model also makes it possible to extend the original model of Alpers and Hennings by including advection and second order terms. From the results of the model calculations presented in the previous section the following conclusions are drawn :

1. Advection can be important for both the magnitude of the modulation in the radar backscatter and the position of this modulation relative to the bottom topography, notably at L-band for features smaller than 1 km like sand waves. This has also been concluded by Hennings (1988).
2. The terms of second order in δA and δV, neglected by AH in their model with advection but included in this work, have only a small effect on the phase shift and the modulation depth. They shift the action spectrum upward for small values of the relaxation rate.
3. When advection is included into the model of Alpers and Hennings the three models studied in this work give almost the same results. Therefore the effects of quadratic terms in the source function and the effects of wave number and wind speed variations due to current velocity variations in the relaxation rate are small.
4. The modulation at X-band is an order of magnitude smaller than at L-band. This contradicts the experimental result that the modulation at X-band is of the same order of magnitude as at L-band.

The calculations from which these conclusions are drawn, were performed with moderate variation in the current velocity (10%). For large variations the quadratic terms in the source function are expected to become more important. It should be noted that the modulation in the radar backscatter at X-band can be increased by including other scattering mechanisms than first order Bragg (Holliday, St-Cyr and Woods, 1986 ; Hennings, 1988) or by taking nonlinear wave-wave interactions properly into account (van Gastel, 1987a).

4 EXPERIMENT

4.1 Introduction

This chapter contains a description of how the main experiment was set up: the choice of the test area, hydro-meteorological conditions and sea truth. A first experiment was performed on September 16th, 1987. A wind speed between 4 and 7 m/s (3 - 4 Bft) was expected for this day. However, the wind dropped to 1 Bft during the experiment and therefore the radar images showed no sign of bottom topography. Then it was realized that a minimum wind speed exists at which the radar backscatter from the sea is detectable by the radar system. The experiment was repeated successfully on January 19th, 1988 at a wind speed between 7.3 and 8.3 m/s (5 Bft). All further references are to this experiment unless explicitly stated otherwise.

The choice of the test area is motivated in section 4.2. This section also contains a description of the flight tracks of the laboratory aircraft carrying the Dutch Digital SLAR.

Old measurements of the current velocity at the Noordwijk Platform (MPN) were used to estimate the periods in the tidal cycle during which the current velocity exceeds 0.4 m/s or 0.5 m/s. These periods are around high and low tide in Scheveningen. This is discussed in section 4.3.

Section 4.4 deals with the choice of the wind speed. The optimum wind speed for mapping bottom topography with the Dutch Digital SLAR is estimated between 7 and 10 m/s using a parametrization of the radar cross section of the sea. Also the difference in optimum wind speed for the various radar systems is discussed in this section.

Section 4.5 contains a description of the Dutch Digital SLAR system as it was used during the experiment of January 19th, 1988.

The sea truth that is needed for the interpretation of the radar images and their comparison with theoretical predictions is discussed in section 4.6.

4.2 Test area and flight tracks

Three different area's were considered to perform the experiment :

1. The area 75 km West of Hoek van Holland
2. An area off the coast of Zeeland and Zuid Holland, to be selected using the 'oil-SLAR' images.
3. The area 20 km NW to the Noordwijk Platform

Area 1 is centered around the point with coordinates 50° 55' 59.26" N and 2° 59' 31.30" E, 75 km West of Hoek van Holland. The topography of the sea bottom in this area is dominated by sand waves with a height between 5 and 10 m. The crest-to-crest distance is typically 300 m. The current velocity has been measured here in 1984 by van Gastel (1987b).

Area 2 has a complicated structure. This area contains sand banks and parts with sand waves. It has been recorded by the 'oil-SLAR' during 1986 and 1987 (see chapter 2).

Area 3 has its bottom topography also dominated by sand waves. Here they have a height varying between 2 and 6 m. The crest-to-crest distance is typically 500 m. Several radar observations have been made in this area from 1969 onwards (de Loor and Brunsveld van Hulten, 1978 ; de Loor, 1981).

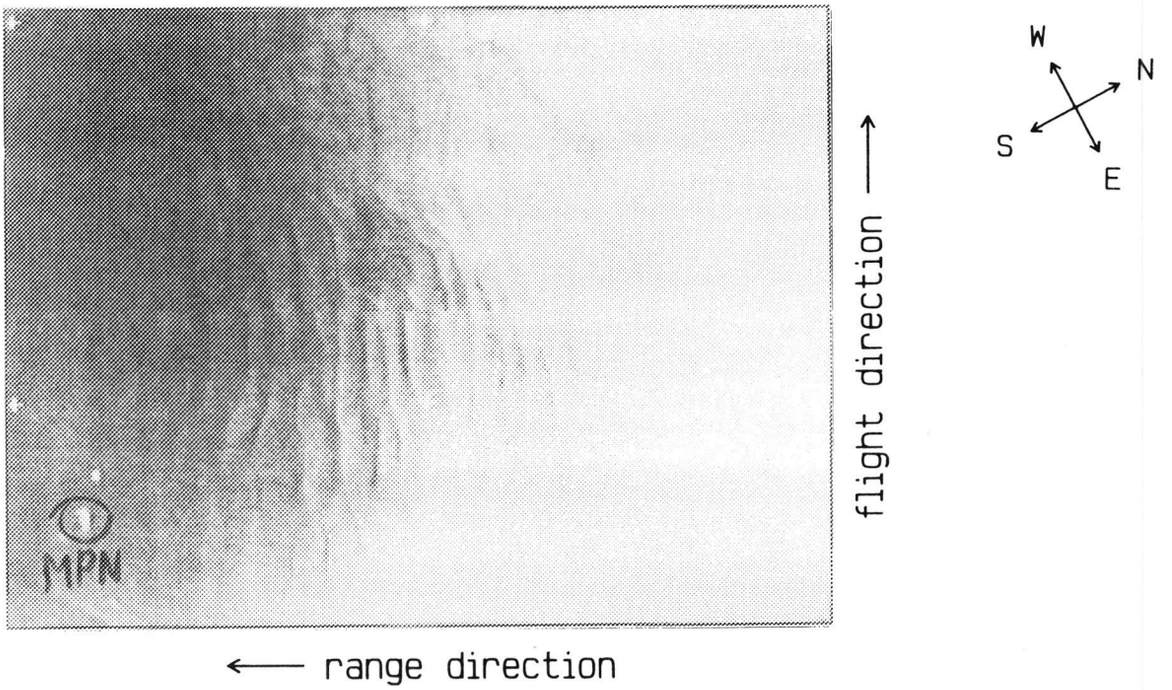

Figure 8. 'Oil-SLAR' image of the test area showing sand waves taken on June 22, 1987 at 6:19 GMT from a height of 1500 ft. The wind was SW, 4.8 m/s ; the aircraft heading 299°. The Noordwijk Tower (MPN) is visible in the lower left corner.

Figure 8 shows a recent 'oil-SLAR' image taken near this area.

A test area suitable for performing the experiment has to meet the following requirements :

1. Simple and preferably quasi one-dimensional bottom topography.
2. Close to a fixed measuring platform.

The first requirement is imposed in order to facilitate the comparison of radar images to digitized bathymetric maps. The test area must be quasi one-dimensional to keep comparison with theoretical predictions feasible, since most existing theories of the imaging mechanism are one-dimensional (see chapter 3). The second requirement is imposed in order to obtain the sea truth as easily as possible. Considering these requirements area's 1 and 2 are rejected and area 3 is preferred.

Figure 9 shows the test area. It consists of two rectangles, EFGH and PQRS, each measuring 5 km by 10 km. The rectangles are mutually perpendicular and have the same centre point M. The longer side of EFGH is parallel to the average current direction and perpendicular to the sand wave crests. The data concerning height and orientation of the sand waves in the test area are taken from van Alphen and Damoiseaux (1986). The distance between M and MPN is 21.8 km, the distance between MPN and the coast line is 9.5 km. The geographical coordinates of the points are listed in table 8.

Both rectangles were recorded from both flight directions parallel to the longer sides, as shown in figure 10a. In this way the effect of the angle between flight direction and current velocity direction can be

studied. The distance between the projection of the flight track on the sea surface and the nearest longer side measures 1636 m. The aircraft flew at a height of 1500 m. This implies that the angle of incidence varied between 47.5° and 77.3°, as shown in figure 10b. These measurements were performed around high and low tide (at opposing current directions) to study the effect of the current velocity direction.

Point	Height (N)	Length (E)	Point	Height (N)	Length (E)
E	52° 25.60'	4° 2.23	P	52° 25.16'	3° 59.25'
F	52° 20.96'	3° 57.64'	Q	52° 22.78'	3° 57.00'
G	52° 19.54'	4° 1.44'	R	52° 20.00'	4° 4.47'
H	52° 24.10'	4° 6.00'	S	52° 22.26'	4° 6.70'
M	52° 22.54'	4° 1.84'	MPN	52° 16.43'	4° 17.77'

Table 8. Geographical coordinates of the test area.

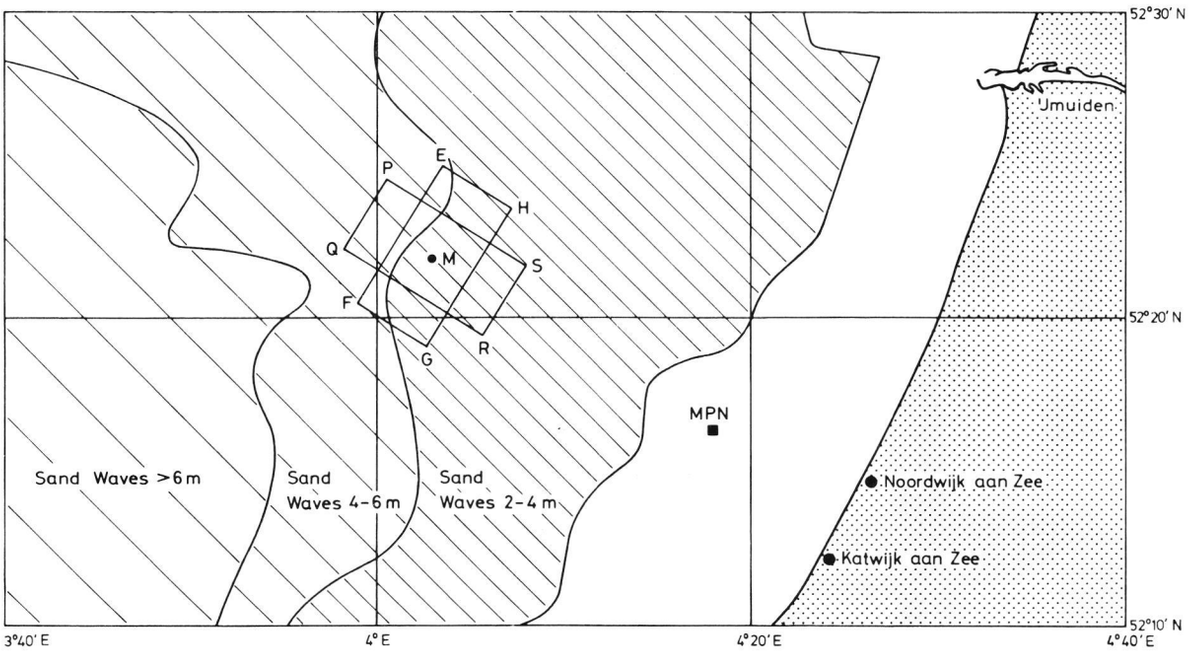

Figure 9. The test area for the main experiment off the Dutch coast.

At the beginning and the end of each flight the aircraft passed the Noordwijk Platform (MPN). The image of MPN can be used as a position fix (see also section 5.3)

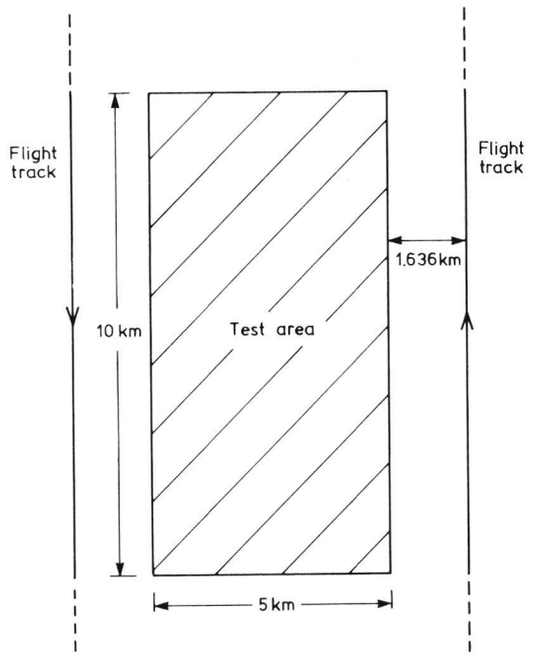

Figure 10a. Top view of flight track.

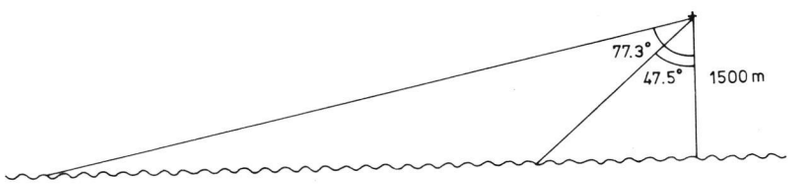

Figure 10b. Side view of flight track.

4.3 Tidal phase

It is mentioned in the literature that the sea bottom topography can be made visible with imaging radars when the current velocity is at least 0.5 m/s. This is confirmed by the evaluation of the 'oil-SLAR' images in chapter 2. It is known from earlier radar measurements that the periods of optimum visibility of the sand waves occur between high and low tide, when the current velocity is at its maximum. Alpers and Hennings (1984) predict

the modulation in the radar cross section due to bottom topography to be proportional to current velocity (see chapter 3). Therefore the experiment should be performed when the current velocity is as large as possible, preferably larger than 0.5 m/s.

Old measurements of the current velocity at MPN were available. These measurements were recorded on November 7th, 8th and 10th, 1977. From the graphs of the current velocity as a function of time the periods in which the current velocity exceeds 0.4 m/s or 0.5 m/s were found, together with the time of occurrence and the value of the maximum current velocity. The results for low tide are collected in table 9.

Date	T_{LWS}	V > 0.4 m/s begin	V > 0.4 m/s end	V > 0.5 m/s begin	V > 0.5 m/s end	T_{max}	V_{max} (m/s)
Nov 7 1977	7:22	-2:32	-0:10	-	-	-1:58	0.45
Nov 7 1977	19:35	-1:45	-0:47	-	-	-1:05	0.45
Nov 8 1977	8:20	-1:38	-0:14	-1:08	-0:44	-0:56	0.52
Nov 8 1977	20:32	-2:32	-0:02	-1:32	-1:32	-1:32	0.50
Nov 10 1977	9:55	-2:55	+0:17	-2:31	-0:19	-1:43	0.55
Nov 10 1977	22:10	-2:34	+0:38	-2:10	-1:28	-1:58	0.53
Mean		-2:20	-0:03	-1:50	-0:46	-1:32	0.50

Table 9. Current velocity data at MPN for low tide.

The first and second column of table 9 contain the date and T_{LWS}, the time of low tide in Scheveningen (in MET), extracted from the tidal tables (Rijkswaterstaat, 1976). The third column contains the beginning and the end of the period in which the current velocity exceeds 0.4 m/s. These times are relative to T_{LWS}. The fourth column contains the beginning and the end of the period (relative to T_{LWS}) in which the current velocity exceeds 0.5 m/s. The last columns contain the time relative to T_{LWS} of the maximum current velocity and the value of the maximum current velocity respectively. All times are written as hh:mm.

The requirement that the current velocity exceeds 0.4 m/s is sometimes to restrictive for low tide. From table 9 it follows that during the measurements the current velocity exceeded 0.4 m/s on an average between T_{LWS} - 2:20 and T_{LWS} - 0:03, and always between T_{LWS} - 1:38 and T_{LWS} - 0:47.

The results for high tide are shown in table 10. This table has the same structure as table 9. T_{HWS} is the time of high tide in Scheveningen (in MET), extracted from the tidal tables. The times in the third, fourth and fifth column are relative to T_{HWS}. From table 10 it is found that during the measurements the current velocity exceeded 0.5 m/s on an average between T_{HWS} - 1:04 and T_{HWS} + 2:17, and always between T_{HWS} - 0:16 and T_{HWS} + 2:05.

Date	T_{HWS}	V > 0.4 m/s begin	end	V > 0.5 m/s begin	end	T_{max}	V_{max} (m/s)
Nov 7 1977	11:52	-0:52	+2:44	-0:16	+2:08	+0:38	0.67
Nov 8 1977	0:16	-1:52	+3:02	-1:40	+2:32	-0:28	0.80
Nov 8 1977	12:43	-1:19	+2:23	-0:55	+2:05	+0:41	0.62
Nov 10 1977	1:52	-1:46	+2:32	-1:22	+2:08	-0:04	0.88
Nov 10 1977	14:12	-1:18	+3:00	-1:06	+2:30	0:00	0.76
Mean		-1:25	+2:44	-1:04	+2:17	+0:11	0.75

Table 10. Current velocity data at MPN for high tide.

The following assumptions regarding the behavior of the current velocity are now made :

1. The influence of the wind on the current velocity is neglected. During the measurements the wind speed varied between 7 and 15 m/s (4 - 7 Bft), which is equal to or greater than the wind speed during the experiment (see the next section).
2. The maximum current velocity occurs simultaneously at MPN and the test area. This is reasonable since the line that connects M, the centre of the test area, with MPN is perpendicular to the coast line.

Under these assumptions the preferred period for performing the experiment is the period in which during the measurements the current velocity always exceeded 0.4 m/s at low tide and 0.5 m/s at high tide. The possible period is the period in which during the measurements the current velocity on an average exceeded 0.4 m/s at low tide and 0.5 m/s at high tide.

The value of the current velocity is estimated suitable for performing the experiment :

1. At low tide between T_{LWS} - 2:20 and T_{LWS} - 0:03, preferably between T_{LWS} - 1:38 and T_{LWS} - 0:47.
2. At high tide between T_{HWS} - 1:04 and T_{HWS} + 2:17, preferably between T_{HWS} - 0:16 and T_{HWS} + 2:05.

4.4 Wind speed

The experience with the old EMI SLAR has taught that the sea bottom topography can be made visible at wind speeds between 1 and 10 m/s (1 - 5 Bft). This is confirmed by other measurements found in the literature. The optimum wind speed for the EMI SLAR is between 5 and 8 m/s (around 4 Bft). This agrees with the optimum wind speed of 4 - 10 m/s (3 - 5 Bft) for the 'oil-SLAR' found from the evaluation of the 'oil-SLAR' images in chapter 2. No evidence was found for any dependence on the wind direction in the 'oil-SLAR' images, in contrast with the EMI SLAR images. At wind speeds exceeding 10 m/s (more than 5 Bft) the phenomenon becomes less visible because of the increasing roughness of the sea.

On theoretical grounds it is expected that the modulation in the radar backscatter increases with decreasing wind speed (see chapter 3). In particular, van Gastel (1987a) predicts very large modulations in the radar cross section of the sea surface at low wind speeds between 1 and 3 m/s (1

- 2 Bft). This does not imply that low wind speeds are favorable for mapping bottom topography, since the radar cross section of the sea is very small at low wind. In those cases the intensity of the radar backscatter can be below the noise level of the Dutch Digital SLAR, so the effect will not be detectable.

Figure 11 shows the normalized radar cross section (NRCS) of the sea σ_0 in the upwind direction for HH polarization as a function of the angle of incidence θ at different values of the wind speed u_{19} at 19 m anemometer height. The curves in figure 11 were obtained analysing literature data and fitting to measurements made from MPN for θ between 20° and 70° (de Loor, 1988).

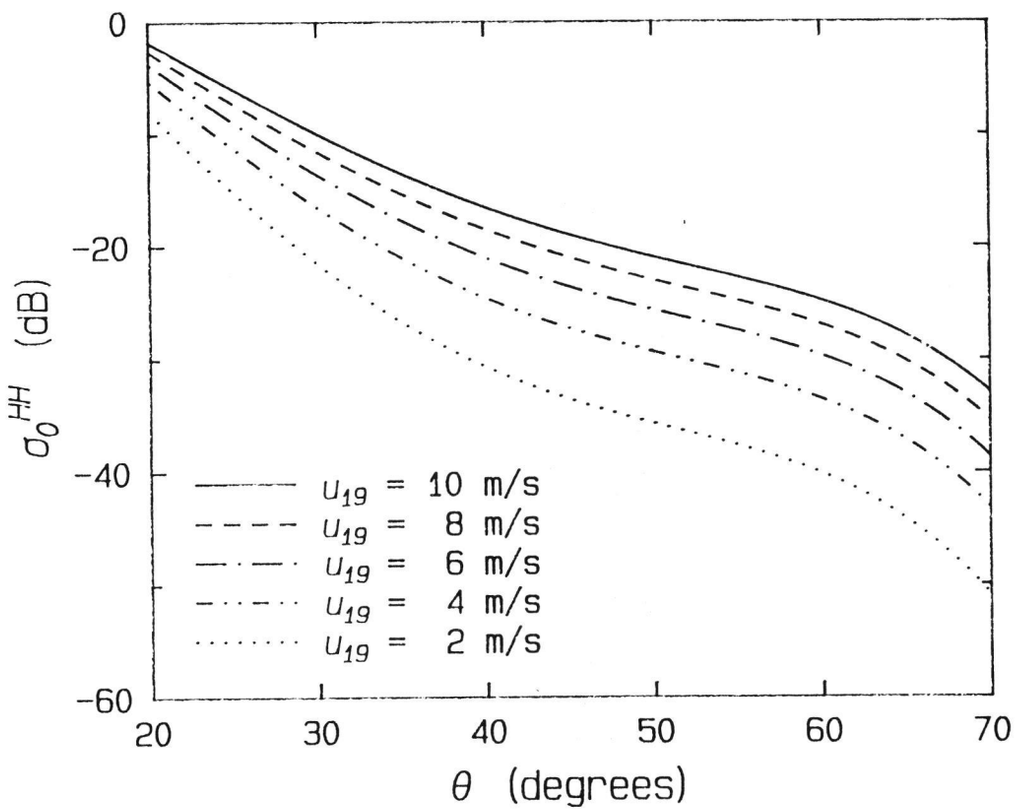

Figure 11. Dependence of the normalized radar cross section of the sea σ_0 for HH polarization as a function of the angle of incidence θ at different values of the wind speed at 19 m anemometer height u_{19}.

From figure 11 one can see that the NRCS σ_0 decreases with decreasing wind speed and increasing angle of incidence. An angle of incidence of 70° corresponds with a distance of 4.1 km from the projection of the aircraft track on the ground (halfway the test area, see figures 10a and 10b)

The minimum radar cross section detectable by the Dutch Digital SLAR is estimated to be -34 dB. The minimum radar cross section of the 'oil-SLAR' is about the same. However, the 'oil-SLAR' illuminates a larger area, operates at VV polarization, and the NRCS σ_0 of the sea is about 5 dB higher at this polarization. Therefore the 'oil-SLAR' is a more sensitive instrument for mapping bottom topography than the Dutch Digital SLAR. The minimum radar cross section detectable by the old EMI SLAR was about -47 dB, because the EMI SLAR had larger emitted power and larger pixel size than the Dutch Digital SLAR. This explains why bottom topography was visible in EMI SLAR images even at very low wind speeds of 1 - 3 m/s (1 - 2 Bft).

From figure 11 it is inferred that the wind speed should be well above 10 m/s (6 Bft or more) for mapping bottom topography with the Dutch Digital SLAR. Theory and experiment indicate that the modulation in the radar backscatter is small at these wind speeds. Moreover, white capping can interfere with the imaging mechanism for wind speeds above 10 m/s (5 Bft).

The minimum NRCS σ_0, detectable by the Dutch Digital SLAR, can be decreased by a 6 dB by using a longer pulse length (200 ns instead of 50 ns) in the radar system. Then a wind speed of 7 - 10 m/s (5 Bft) should be sufficient for mapping bottom topography. As a consequence, however, the radar image can then not be absolutely radiometrically calibrated, because the system can not longer discern the return of the calibration pulse from the other signals. Since the main interest is in the relative variations in the radar backscatter and the images are still relatively radiometrically calibrated, this is not considered a serious drawback.

The atmospheric condition must not be stable. This means that the sea water temperature must not be lower than the air temperature. This requirement is imposed because the radar cross section of the sea decreases strongly with increasing stability.

Therefore it is concluded that the experiment has to be performed at a wind speed between 7 m/s and 10 m/s (5 Bft), regardless of the wind direction. The atmospheric condition has to be neutral or instable (sea water temperature equal to or greater than air temperature). The Dutch Digital SLAR should operate with a long pulse length.

4.5 The Dutch Digital SLAR

The Dutch Digital SLAR is a SLAR system designed for remote sensing research. It is operated from the Swearingen Metro II laboratory aircraft of the National Aerospace laboratory NLR. The system is developed as a successor of the old EMI system, which was an analog SLAR system that recorded the data on photographic film. The radar signal is digitized and recorded, without processing, in digital form by means of a High Density Digital Recorder. At the laboratory data is reproduced for quick look and selected parts are written on computer compatible tape to be processed.

The software system PARES is available to perform routine processing. PARES combines SLAR data, position/altitude data as measured by an Inertial Sensor System, and radiometric calibration data (antenna diagram) to calculate a digital map of the radar backscatter coefficient : the radar image. This image is geometric correct ; images can be overlaid by simple routines.

The configuration of the SLAR system used for the experiment is :

- SLAR antenna
- DECCA Transceiver unit, modified and with a calibration circuit added
- SPEEDIG Digitizer unit with DAF2 formatter interface
- AMPEX AR700 instrumentation recorder with High Bit Rate interface
- LTN58 Inertial Sensor System and IRIG B/A Time Code generator

The main characteristics of the SLAR system in combination with the PARES software as used for the experiment are listed in table 11.

TRANSMITTER	
radar frequency	9.4 GHz
pulse power	25 kW
pulse width	200 ns (instead of 50 ns)
pulse repetition frequency	200 Hz
ANTENNA	
construction	slotted wave guide, HH polarization
beam width	10 mrad (horizontal, two way)
gain	max 30 dB, at -5° to aircraft axis
RECEIVER	
dynamic range	80 dB
band width	DC-10 MHz
DIGITIZING	
sample frequency	50 MHz (20 ns)
levels per sample	256 (8 bits)
samples per line (pulse)	4096
line length	12 km
sample interval	3 m
line interval	0.5 m
FLIGHT	
nominal ground speed	90 - 100 m/s
altitude	1500 m
PROCESSING	
geometric resolution cross track	30 m (instead of 7.5 m)
geometric resolution along track	10 m per km slant range
grid	15 x 15 m
dynamic range	50 dB
radiometric resolution	0.2 dB

Table 11. Main characteristics of the Dutch Digital SLAR system as used for the experiment.

4.6 Sea truth

One of the goals of the experiment is to establish the possibilities and limitations of using the mapping of sea bottom topography with imaging radars for cartographic purposes. Therefore the radar images were compared with digitized bathymetric maps of the test area to establish the relation between the two. The construction of these maps is described in section 5.2. The relation between the bathymetric maps and the radar images found from the experiment can be compared with theoretical predictions. This will give information about our understanding of the imaging mechanism.

From measurements of the current velocity profile at some point in the test area and from the wind speed during the last 12 hours, the surface current velocity can be calculated using the method of Davies (1987, 1988). Then the current velocity in the whole test area can be calculated from the continuity equations (11a) and (11b). This fixes all variables needed to compute the relative modulation in radar cross section of the sea as given by the simple relaxation theories described in chapter 3. Measurement of the current velocity at two or more points will give insight in the applicability of the continuity equations. Therefore the following sea truth is necessary for the interpretation of the experiment :

1. The current velocity profile at (one or more) points in the test area
2. The wind vector during the period from 12 hours before the experiment to the experiment itself
3. The temperature of sea water and air

The temperatures were needed to check if the atmospheric conditions were indeed neutral or instable as required.

During the experiment the current velocity profile was measured from two ships, one located above a sand wave crest and the other above a trough. The other quantities were collected at MPN on a routine base. The angle of incidence can be extracted from the position data of the aircraft during the measurements.

The positional accuracy in the radar images was improved by using the images of MPN (before and after each flight) and the ships measuring the current velocity profile as described in section 5.3.

5 DATA PROCESSING

5.1 Introduction

This chapter deals with the further processing of the data collected during the experiment and the construction of a digitized bathymetric map of the test area. The radar images are geometrically corrected by the PARES software at NLR. Since the longer pulse length was chosen to improve the sensitivity of the Dutch Digital SLAR system, absolute radiometrically calibration of the images is not possible. However, the images are still relatively radiometrically calibrated.

The construction of a digitized bathymetric map from an ordinary bathymetric map (Dienst der Hydrografie, 1984) using spline interpolation techniques is discussed in section 5.2.

In section 5.3 it is described how the position in the radar images is fixed using the known positions of fixed points (MPN and the measuring ships). With this procedure the error in position is estimated two pixels (30 m).

This chapter is quite technical in nature. It can be skipped by readers who are not interested in technical details.

5.2 Construction of digitized bathymetric maps

An ordinary bathymetric map (Dienst der Hydrografie, 1984) of the test area is available. The scale of the map is 1:25000. The depth was measured along parallel lines at a direction of 36° true North. The small solid squares in figure 12 indicate the positions at which the depth was measured. These lines are parallel to the coast line and perpendicular to the sand wave crests. The distance between the lines is 250 m; the distance between the selected points on a line at which the depth was measured continously varies between 50 m and 300 m, with a mean distance of 75 m. The accuracy of the depth is 0.25 m.

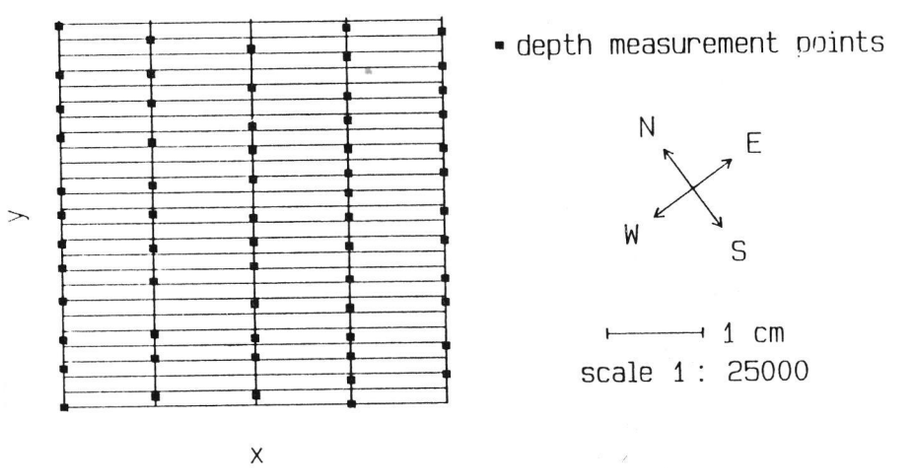

Figure 12. Grid for the calculation of the digitized bathymetric map.

On the map a coordinate system was defined with the y-axis parallel to the lines at which the depths were measured (see figure 12). The positions and depths in this new coordinate system were digitized for an area measuring 11 km in the x-direction and 12 km in the y-direction. This area encloses the test area. With the known geographical coordinates of three points on the map the relation between x-y coordinates and geographical coordinates can be readily established. The coordinates of the origin (x = 0 and y = 0) are 52° 21.920' N and 3° 54.447' E.

The first step in the construction of a digitized map consists of calculating a cubic spline interpolation for each line in the y-direction (vertical lines in figure 12). A cubic spline interpolation reproduces the value of the original points and has continuous first and second derivative. For the calculation the second derivative of the depth at both ends is needed. As usual this second derivative is set to zero, causing the interpolation to be less accurate at the ends. Therefore the digitized area was taken larger than the test area. With the spline interpolation the depths on a rectangular grid in the x-y coordinates can be calculated.

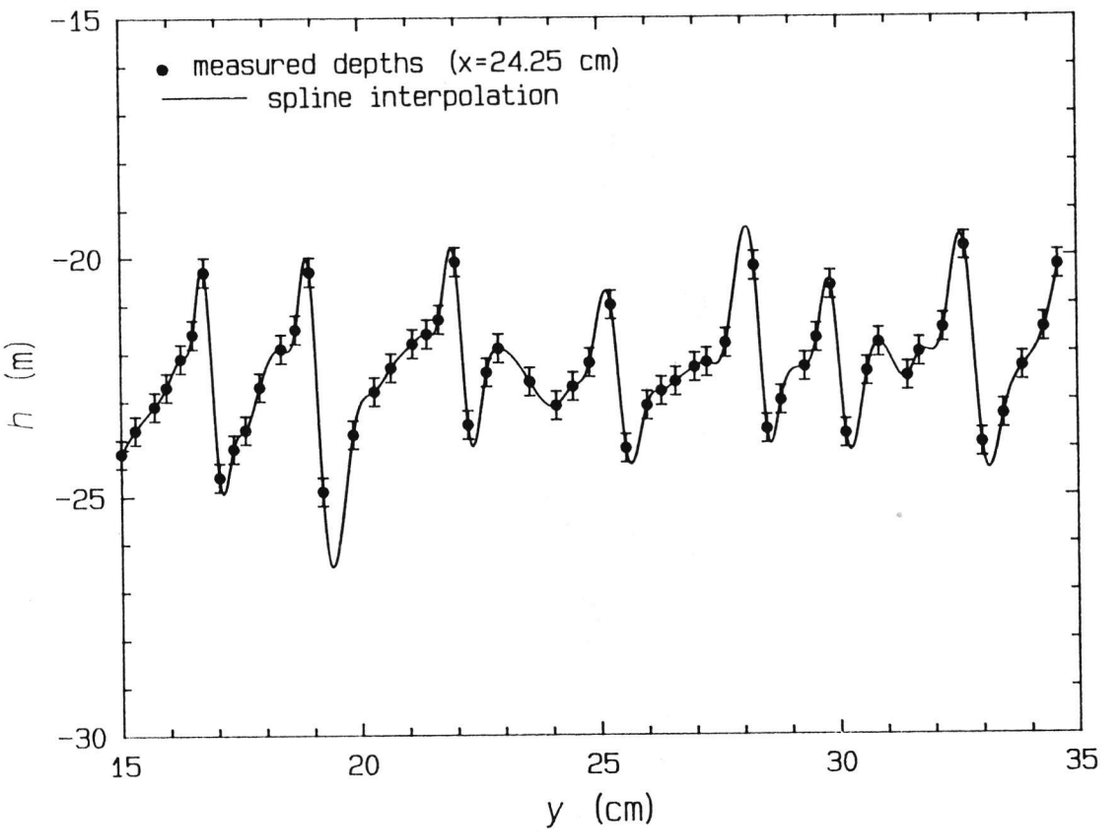

Figure 13. Interpolated and original depths.

The second step consists of calculating a two-dimensional cubic (bicubic) spline interpolation from the depths on a rectangular grid. Note that this bicubic spline interpolation uses the interpolated values of the depth at the grid points (see figure 12). Therefore the distance in y-direction of the grid points should be small enough to ensure that the bicubic spline interpolation reproduces the original depths within their errors. With a distance of 40 m between the grid points in the y-direction the bicubic spline interpolation compares well with the original depths.

This can be seen in figure 13, which shows the original measurements (solid dots) and the interpolation (solid line) for y ranging from 15 to 30 cm at x = 24.25 cm. This corresponds to a line of 3.75 km length, passing through the centre of the test area and running parallel to the coast line and perpendicular to the sand wave crests. At the crests and troughs of the sand waves the interpolation suffers some 'overshoot', due to large variations in depth at short distances. This 'overshoot' is of the same order of magnitude as the error in the depth. Note the asymmetric shape of the sand waves in figure 13.

With this bicubic spline interpolation it is possible to calculate not only the depth at each point of the test area, but also the gradient of the depth (bottom slope) in any direction.

It should be remarked that the bathymetric map used here dates from 1984 while the radar images were recorded in 1988. The bottom topography of the test area is stable : comparison of the bathymetric map used here with a map from 1977 showed no significant changes in the depth. Therefore it is assumed that no large changes in the bottom topography have occurred between the measurements of the depth in 1984 and the experiment in 1988 and that the bathymetric map is still correct.

5.3 Positioning of the radar images

The radar images recorded with the Dutch Digital SLAR system are processed using the PARES software at NLR. The resulting images are geometrically correct. This means that the images can be compared directly with a (bathymetric) map of the same scale as the images. To do so, five parameters have to be known :

- P_x : the pixel size in flight (x-) direction
- P_y : the pixel size in range (y-) direction
- Φ : the image direction (in degrees true North)
- H_{11} : the geographic latitude (height) of the first pixel on the first line
- L_{11} : the geographic longitude (length) of the first pixel on the first line

P_x and P_y define the scale of the radar image, Φ fixes the orientation of the radar image relative to the map while H_{11} and L_{11} fix the origin of the radar image relative to the map. The geographical height H_{ij} and length L_{ij} of a point in the radar image with line number i and pixel number j is then given by

$$H_{ij} = H_{11} + [(i-1)\sin(\Phi) P_x + (j-1)\cos(\Phi) P_y]/R_H , \qquad (44a)$$

$$L_{ij} = L_{11} + [(i-1)\cos(\Phi) P_x - (j-1)\sin(\Phi) P_y]/R_L . \qquad (44b)$$

When the pixel size is expressed in meters and the geographical coordinates

in minutes, the transformation factors R_H and R_L are given by

$$R_H = 1854 \text{ m/min} , \tag{45a}$$

$$R_L = 1854 \cos(H_{11}) \text{ m/min} . \tag{45b}$$

In other words, R_H is the length (in meters) of one minute geographical height and R_L the length (in meters) of one minute geographical length at geographical height H_{11}.

The parameters P_x, P_y, Φ, H_{11} and L_{11} are calculated by the PARES software from the position and movements (pitch, roll and yaw) of the aircraft. The evaluation of the aircraft movements requires numerical integration of the accelerations recorded during flight. Combined with the errors in the measurements of position and acceleration, this may cause considerable errors in the parameters P_x, P_y, Φ, H_{11} and L_{11}. Independent calculation of these parameters requires (at least) three known points in the radar image. The radar images recorded during the experiment contain only one (MPN) or two (the ships measuring the current velocity profile) known points.

Fortunately, the values of the pixel size, P_x and P_y, and of the image direction, Φ, are calculated by the PARES software with an accuracy of 1% or better. This is sufficient for this work. Therefore only one known point suffices to calculate the coordinates of the first pixel on the first line, H_{11} and L_{11}. The coordinates of MPN are known (see table 8). The coordinates of one of the ships in the test area (the 'Octans') was recorded with high precision during the experiment using a HYPERFIX position fixing system. When both line and pixel number and geographical coordinates of a point in the radar image are known, H_{11} and L_{11} can be calculated easily. The line and pixel number were found by inspection. Since MPN and the ships cover several pixels in the radar images, due to very strong reflections, these points can be located with an accuracy of about one pixel in both flight and range direction. Together with an error of about 1% in pixel size and image direction, the error in position in the radar image is estimated two pixels (30 m) at most.

Figure 14a show the geographical correction in H_{11} and L_{11} (the difference between the position of the first pixel on the first line given by the PARES software and that calculated using the known point) as a function of time for the first flight. Figure 14b shows the geographical correction as a function of time during the second flight. In both figures the geographical correction is expressed in minutes. The squares give the geographical correction in the position of MPN, the circles that of the 'Octans'. The solid and broken lines are spline interpolations to distinguish the corrections in height and length from each other. Four images were recorded during each flight. Since the ships measuring the current velocity profile had not yet arrived to their positions at the time the first image of the first flight was made, figure 14a contains only three geographical corrections for the 'Octans'.

From figures 14a and 14b it can be seen that the correction in H_{11} and L_{11} can be as large as 2' in length and 1.5' in height, which is of the order of 3 km. This demonstrates clearly that radar images recorded by the Dutch Digital SLAR must contain at least one known point in order to fix the position precisely. Note that the geographical correction is not linear in time. This is due to the manoeuvres of the aircraft between the recording of the images.

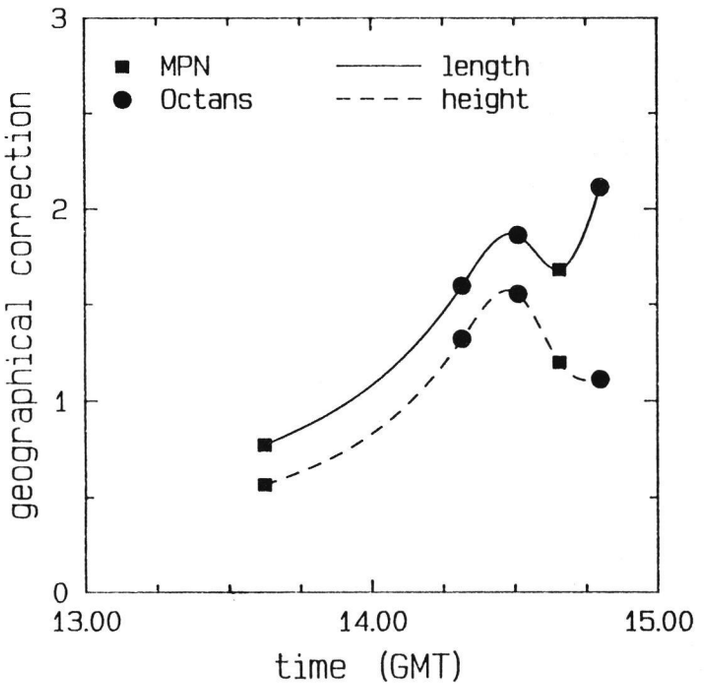

Figure 14a. The geographical correction in length and height (in minutes) as a function of time during the first flight.

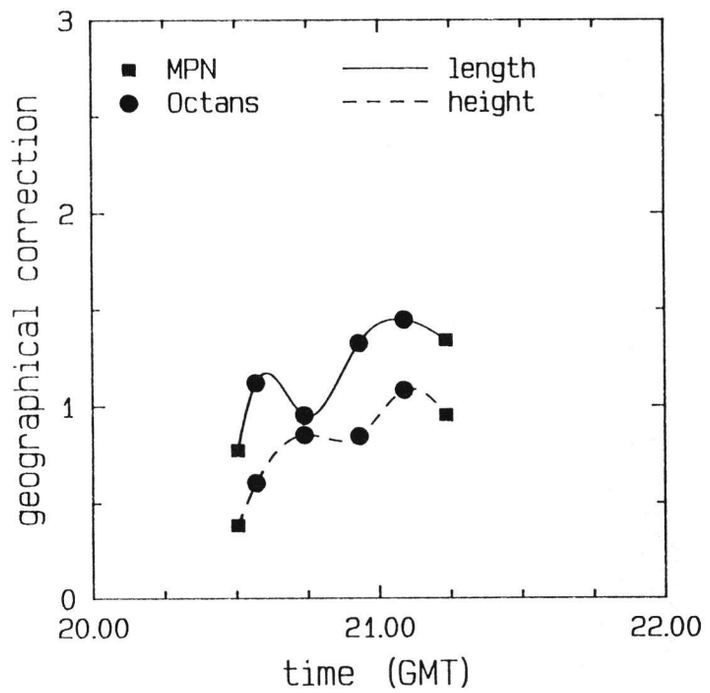

Figure 14b. The geographical correction in length and height (in minutes) as a function of time during the second flight.

6 RESULTS AND DISCUSSION

6.1 Introduction

The main experiment was performed on January 19th, 1988. Two flights were made at opposing directions of the current velocity, the first flight in the afternoon and the second in the evening. During each flight the test area was recorded from four different flight directions by the Dutch Digital SLAR. Therefore a total number of eight radar images was made of the test area during the experiment. Before and after each flight images were made of Meetpost Noordwijk (MPN) in order to fix the position. Since the position in each radar image is fixed using one of the ships measuring the current velocity profile, as explained in section 5.3, the images of MPN are not considered any further.

Wind speed and direction, temperature of sea water and air, sea water level, significant wave height and the energy of the waves with frequency between 0.2 and 0.5 Hz were recorded on MPN. During the experiment, the current velocity profile was measured with Elmar current meters from two ships at or near the centre of the test area : the 'Smal Agt' on 52° 22.54' N , 4° 1.84' E and the 'Octans' on 52° 22.69' N , 4° 2.00' E. The coordinates of the Octans were recorded with high precision using a HYPERFIX position fixing system.

The images and relevant sea truth are presented in section 6.2. The quality of the images is rather poor, due to the low sensitivity of the Dutch Digital SLAR. Two images, with range direction pointing upwind and perpendicular to the sand wave crests, show the sand waves most clearly. These two images are selected for further study.

The averaged (mean) and surface current velocities were calculated from the current velocity profiles and wind data measured during the experiment using the method of Davies (1987, 1988). The results of these calculations are presented in section 6.3. It is found that the continuity equations (11a) and (11b) give a satisfactory description of the mean current velocity.

As already stated, the quality of the images obtained during the experiment is rather poor. In section 6.4 it is shown that the sand waves can be made visible more clearly when the image is filtered with a low pass Fourier filter or a median filter, the latter giving the best results.

In section 6.5 the modulation depth in the radar images, α, is found to be of the order of 0.4 (see formula (42b) in section 3.5 for the definition of α). This corresponds to a modulation of about 4 dB, in agreement with other experiments. This is an order of magnitude larger than predicted by simple relaxation models, indicating that either non-linear wave-wave interactions must be included or first order Bragg scattering is not an appropriate description at X-band (see chapter 3).

The central parts of the two selected images, filtered with a 3 x 3 median filter, are compared with digitized maps of depth and bottom slope in section 6.6. This comparison indicates that the extremes in the modulation are positioned above regions with maximum bottom slope.

The positional relation between the radar images and the digitized map of the bottom slope can be quantified by calculating the correlation between the two. It is shown in section 6.7 that the extremes in the radar backscatter are indeed located above regions with maximum slope, within the estimated accuracy in position of two pixel sizes (30 m), in perfect

agreement with predictions by simple relaxation models (chapter 3). This is a most important result, not only for the interpretation of X-band radar imagery of the sea but also for the theoretical study of the imaging mechanism.

The relation between the intensity of the radar backscatter and the bottom slope is studied in section 6.8. It is shown that there is a relation between the two. Due to the poor quality of the images this relation can not be used for accurate inverse modelling (calculation of the bottom slopes from the radar images).

This chapter ends with section 6.9 where the conclusions drawn from the experimental results are summarized.

It should be remarked here that the experiment is one of the most complete in its kind : the positioning of the images is very precise and many environmental parameters have been recorded. It is expected that the results presented in this chapter will be of great use for future studies.

6.2 Images and sea truth

Some flight, wind and PARES processing data are collected in table 12. The third column in table 12 contains the time (in GMT, denoted as hh:mm:ss when the recording of the image started and ended respectively. The fourth column contains the image direction (in degrees true North) as given by the PARES software. The wind speed (in m/s) and the wind direction (in degrees true North) are listed in the fifth column. The last column contains the percentage of pixels in the image that were too low for further processing.

Image number	Flight number	Recording time (GMT) start	end	Image dir.	Wind speed	dir.	pixels too low
1	1	14:46:59	14:49:01	-62°	8.3	165°	9%
2	1	14:29:38	14:32:01	-150°	7.4	168°	13%
3	1	13:51:27	13:53:29	128°	7.7	173°	54%
4	1	14:17:59	14:20:01	30°	7.6	174°	46%
5	2	20:33:07	20:35:09	-60°	7.4	197°	8%
6	2	21:04:18	21:06:20	-150°	7.3	188°	15%
7	2	20:43:16	20:45:18	128°	7.5	196°	35%
8	2	20:54:48	20:56:50	30°	7.4	192°	44%

Table 12. Some flight, wind and processing data for the images recorded during the main experiment

Note that the images are not numbered in order of recording time, but according to the aircraft tracks. Since the 'Octans' and the 'Smal Agt' arrived at their position when the first flight already was started, the track of image 1 has been repeated after the overflight of MPN. There was no time left to repeat the track of image 2. Therefore no ships are visible in this image.

According to the tidal tables (Rijkswaterstaat, 1987), the predicted time for high tide in Scheveningen, T_{HWS}, was 15:07 GMT and that for low tide in Scheveningen, T_{LWS}, was 23:14. From the recording times listed in table 12 it can be inferred that the images were made between T_{HWS} - 0:17 and T_{HWS} + 0:42 during the first flight and between T_{LWS} - 1:41 and T_{LWS} - 0:17 during the second flight. These intervals are within the possible intervals specified in section 4.3. As will be shown in section 6.3, the surface current velocity exceeded 0.5 m/s during the radar measurements.

The wind speed varied between 7.3 and 8.3 m/s, which is in the required interval of 7 - 10 m/s (see section 4.4). The significant wave height varied between 50 and 75 cm at MPN during the radar measurements.

During the first flight the sea water temperature varied between 6.6 °C and 6.8 °C and the air temperature between 7.7 °C and 8.1 °C. During the second flight the sea water temperature was 6.8 °C while the air temperature varied between 8.7 °C and 8.8 °C. The air temperature was higher than the sea water temperature by 1 - 2 °C during the experiment. This implies that the conditions were not neutral or instable as required.

Figures 15a and 15b show the radar images made during the experiment. The mean wind direction during each flight is indicated at the centre of the figures, together with the geographical directions. The image direction is indicated with an arrow along each image. The image direction roughly corresponds to the flight direction, the difference between the two being caused by the wind. The range direction is to the left of the image direction. The arrows indicating the image direction are placed at the side of the images where the angle of incidence is lowest.

From figures 15a and 15b it appears that images 1 and 5 show the sand waves most clearly. These images were made with the range direction pointing upwind/crosswind and perpendicular to the sand wave crests. Images 2 and 6 also show the sand waves, but not as clear as images 1 and 5. Here the range direction is also upwind/crosswind, but parallel to the sand wave crests. Theory predicts that the sand waves should not be visible since there should be no variation in the current velocity parallel to the sand wave crests (see the continuity equations 11a and 11b in section 3.2). However, the bottom topography of the test area is not completely quasi one-dimensional. Also the continuity equations can be an oversimplification.

Images 3 and 7 show the sand waves faintly for low angles of incidence, while images 4 and 8 show no sign of bottom topography. These four images were made in the crosswind/downwind direction. It is well known that the radar backscatter of the sea surface is lower in the crosswind and downwind directions than in the upwind direction. From the last column of table 12 it can be seen that a large fraction of the pixels had values too low for further processing. This indicates that the radar backscatter in these images is near or below the detection limit of the Dutch Digital SLAR, causing modulations to be invisible. This view is corroborated by the patchy appearance of the images. The images made with the old EMI SLAR showed the sand waves much better. It should be noted that the conditions during the experiment were slightly stable (1 - 2 °C). This also may decrease the quality of the images.

From this it is concluded that the wind speed during the experiment (between 7.3 and 8.3 m/s) is only slightly above the minimum wind speed for the Dutch Digital SLAR, causing the quality of the image to depend on the flight direction relative to the wind direction. It is also concluded that the Dutch Digital SLAR is a rather insensitive instrument for mapping sea

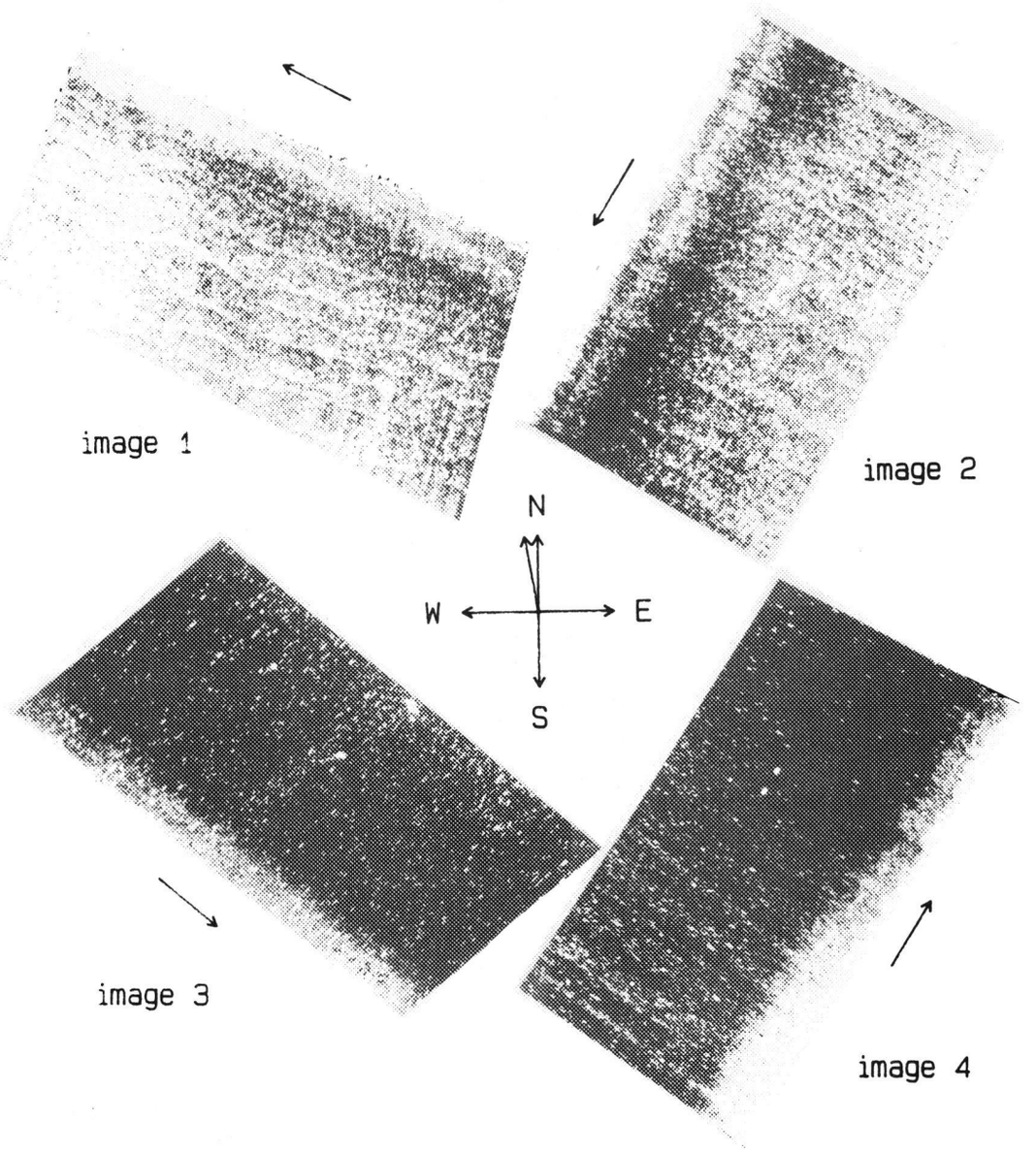

Figure 15a. The radar images recorded during the first flight. The geographical and wind directions are indicated at the centre. The image direction is indicated by the arrow along each image.

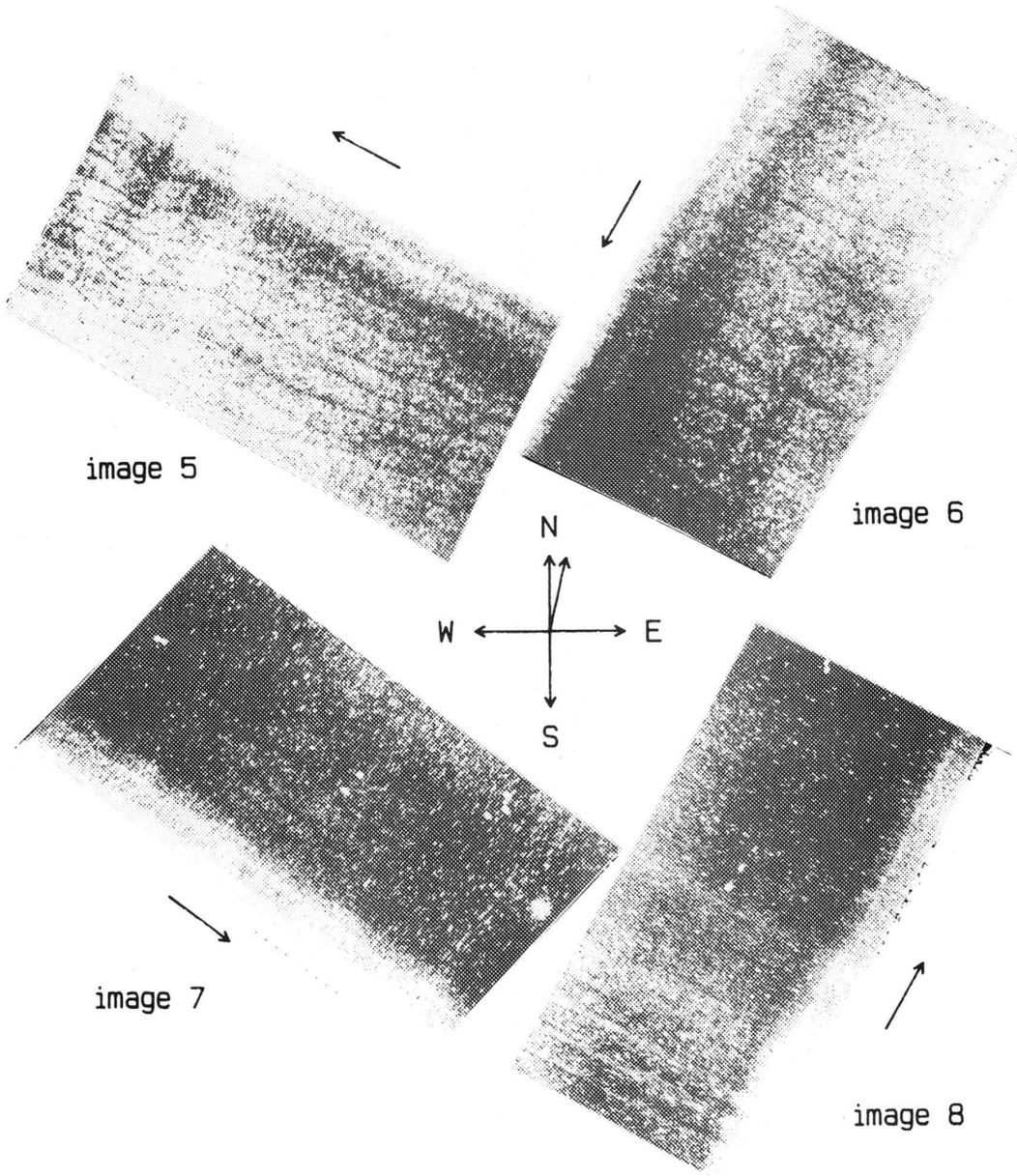

Figure 15b. The radar images recorded during the second flight. The geographical and wind directions are indicated at the centre. The image direction is indicated by the arrow along each image.

bottom topography.

In the following sections only the central parts of images 1 and 5 will be considered, since these images show the sand waves most clearly. It is interesting to note that the modulation in intensity in these two images is opposite : the sand wave pattern can be made to disappear by overlaying them.

6.3 Results for the current velocity

A total number of 53 current velocity profiles was measured with Elmar current meters during the experiment, 26 from the 'Octans' and 27 from the 'Smal Agt'. The 'Octans' was located at 52° 22.69' N , 4° 2.00' E ; the 'Smal Agt at 52° 22.54' N , 4° 1.84' E. The difference in depth at these two positions is about 1.8 m. The measured profiles were combined with the wind data from MPN using the method of Davies (1987, 1988). With this method both the averaged (over the vertical) or mean current velocity U and the surface current velocity V can be calculated.

Assuming the direction of the sand wave crests to be -60° true North, with an error of 5°, it is possible to calculate the current velocity components parallel to the sand wave crests, U_{par} and V_{par}, and the components perpendicular to the sand wave crests, U_{per} and V_{per}. Also the discharge perpendicular to the sand wave crests, D, can be calculated from

$$D = U_{per}\, d\, (1\ m) \quad , \tag{46}$$

where U_{per} is the mean current velocity and d the depth. The factor 1 m is inserted in (46) to give D the dimension m^3/s.

The error in the measured magnitude of the current velocity is about 10%; that in the measured direction about 5°. It is hard to establish the error in the calculated mean and surface current velocities. It seems reasonable to assume that the errors in the calculated quantities are the same as in the measured ones : 10% in the magnitude of the current velocity and 5° in its direction.

Figure 16a shows D as a function of time for the measurements from the 'Octans' and the 'Smal Agt'. According to the continuity equation (11a) D should be the same for both positions, depending only on time. Indeed this is the case within the experimental errors except when the current velocity vanishes (around 18:30 GMT).

Figure 16b shows the mean current velocity component parallel to the sand wave crests, U_{par}, as a function of time for the measurements from the 'Octans' and the 'Smal Agt'. If the continuity equation (11b) is valid, U_{par} must be a function of time only, having the same value at both positions. This is also the case within the experimental errors, again with the exception of vanishing current velocity (around 18:30 GMT).

These results indicate that the continuity equations (11a) and (11b) describe the current velocity well for non-vanishing current velocities. Note that when the current vanishes, sea bottom topography is not observable with imaging radar, so this poses no restriction on the usability of the continuity equations. The results presented here agree with those of van Gastel (1987b). However, these results can not be regarded as conclusive evidence for the validity of the continuity equations for the following reasons :

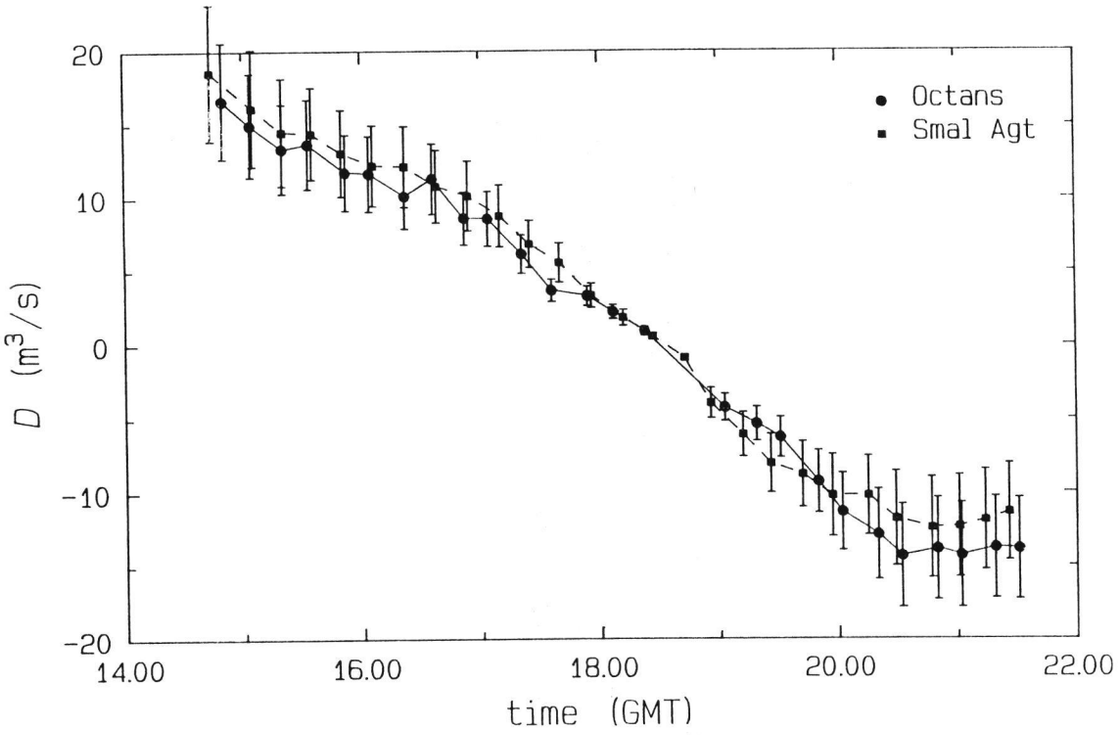

Figure 16a. The discharge perpendicular to the sand wave crests, D, as a function of time.

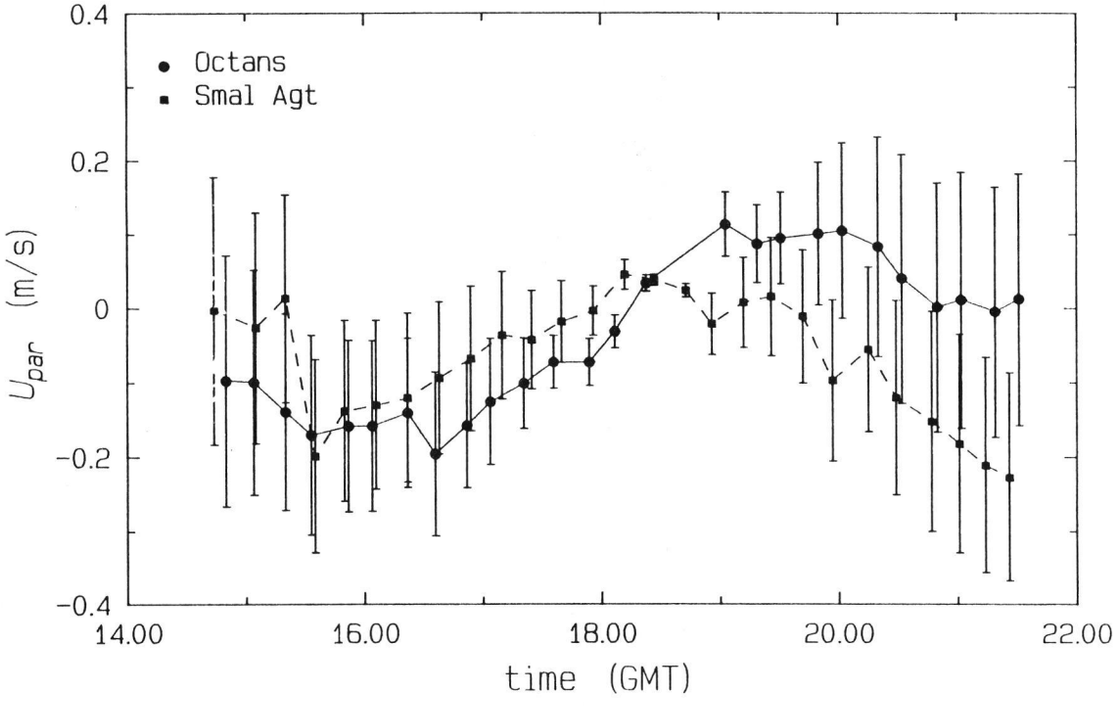

Figure 16b. The mean current velocity parallel to the sand wave crests, U_{par}, as a function of time.

1. The current velocity profiles were measured at two points only. In particular it is not possible to establish whether or not the maximum current velocity is located exactly above regions with minimum depth.
2. The error in the magnitude of the current velocities is about 10%, which is of the same order of magnitude as the relative difference in depth between the two points at which the measurements were performed. With this precision only large deviations from the continuity equations can be detected.

More elaborate and precise measurements and calculations are needed to establish whether or not the continuity equations are valid.

Figure 17 shows the results for the surface current velocity components perpendicular and parallel to the sand wave crests, V_{per} and V_{par}. For reasons of clarity the error bars are not included in figure 17. The magnitude of the current velocity perpendicular to the sand wave crests is between 0.7 and 0.8 m/s during the first flight and between 0.6 and 0.8 m/s during the second flight. This is well above the minimum value of 0.4 or 0.5 m/s required in section 4.3. The current velocity parallel to the sand wave crests is small (0.3 m/s at most).

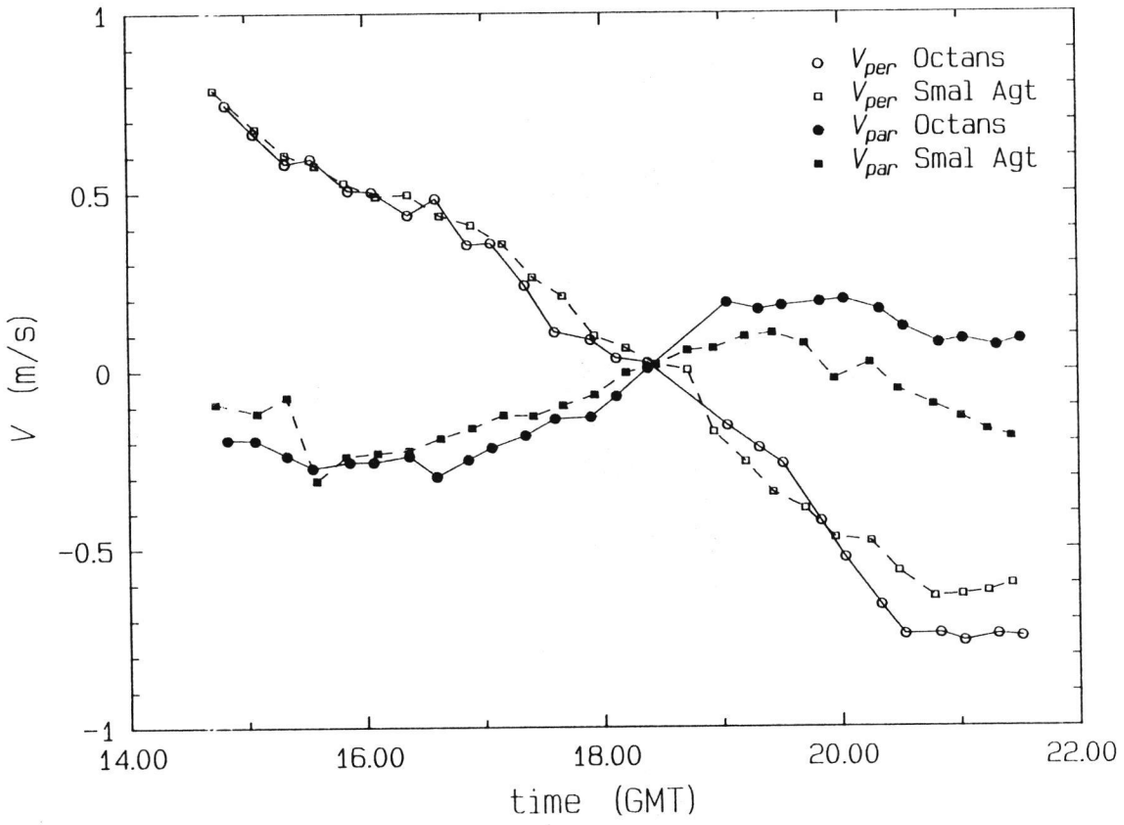

Figure 17. The surface current velocity components parallel and perpendicular to the sand wave crests, V_{par} and V_{per}, as a function of time.

6.4 Filtering of the radar images

The quality of the radar images made during the experiment, shown in figures 15a and 15b, is rather poor; the images have a patchy appearance. To exhibit the sand waves more clearly, the central parts of images 1 and 5 have been filtered. Two types of filters were considered :

1. Low pass Fourier filter
2. Median filter.

A low pass Fourier filter was constructed in the following way : first the two-dimensional Fourier transform of the radar image was calculated. This is a two-dimensional representation of the intensity (pixel value) of the image in spatial wave number space. The absolute value of the spatial wave number ranges from zero (constant intensity) to k_{max} (details as large as one pixel). Then the Fourier components in some direction are set to zero if they have a spatial wave number k larger than a specified cutoff wave number k_c, with

$$k_c = C\, k_{max} \quad , \tag{47}$$

where C is the cutoff factor (between 0 and 1). This means that small intensity variations are deleted from the Fourier representation of the image. After inverse Fourier transformation a smoothened image results. Note that the cutoff factor C is not necessarily the same for different orthogonal directions.

A n x m median filter operates as follows : each pixel value is replaced by the median value of n x m pixels centered around the original pixel (including the original pixel value). This process is continued until less than a specified number of the pixel values changes (say 1% of the total number of pixels).

The original radar images contain 1000 lines with 400 pixels each. Figure 18a shows the central part of image 5 (line 253 to 509 and pixel 102 to 358). The colour scale ranges from black (low backscatter) via white (high backscatter) to orange (very high backscatter) In the centre of the image the two ships are visible in orange. There are also some other pixels with very high backscatter, caused by breaking waves or signals from other radars not recognized by the PARES software. The flight direction is from left to right, the range direction from bottom to top. The geographical, wind and current directions are indicated.

Figure 18b shows the same portion of image 5 in the same colour scale, but filtered with a two-dimensional Fourier low pass filter. The cutoff factor C is 0.05 in the flight (horizontal) direction and 0.40 in the range (vertical) direction. The low pass Fourier filter tends to smear out the features and to decrease the contrast. Rapid changes in intensity are represented by Fourier components with large spatial wave number. Omission of these components causes oscillations, as can be seen from the images of the ships in the centre of figure 18b.

Figure 18c also shows the same portion of image 5 as figure 18a, also in the same colour scale, but now filtered with a 3 x 3 median filter. This figure shows the sand waves most clearly. The image is smoothened without too much loss of detail while the contrast is preserved better than with the Fourier filter. However, some contrast is lost since extreme pixel values are ruled out.

Figure 19 shows the histograms of the images presented in figures 18a, 18b and 18c. From this figure it can be seen that the distribution of pixel values becomes taller and higher by filtering, notably for the low pass Fourier filter.

From the previous figures it is concluded that a median filter gives the best results and is to be preferred over a Fourier filter.

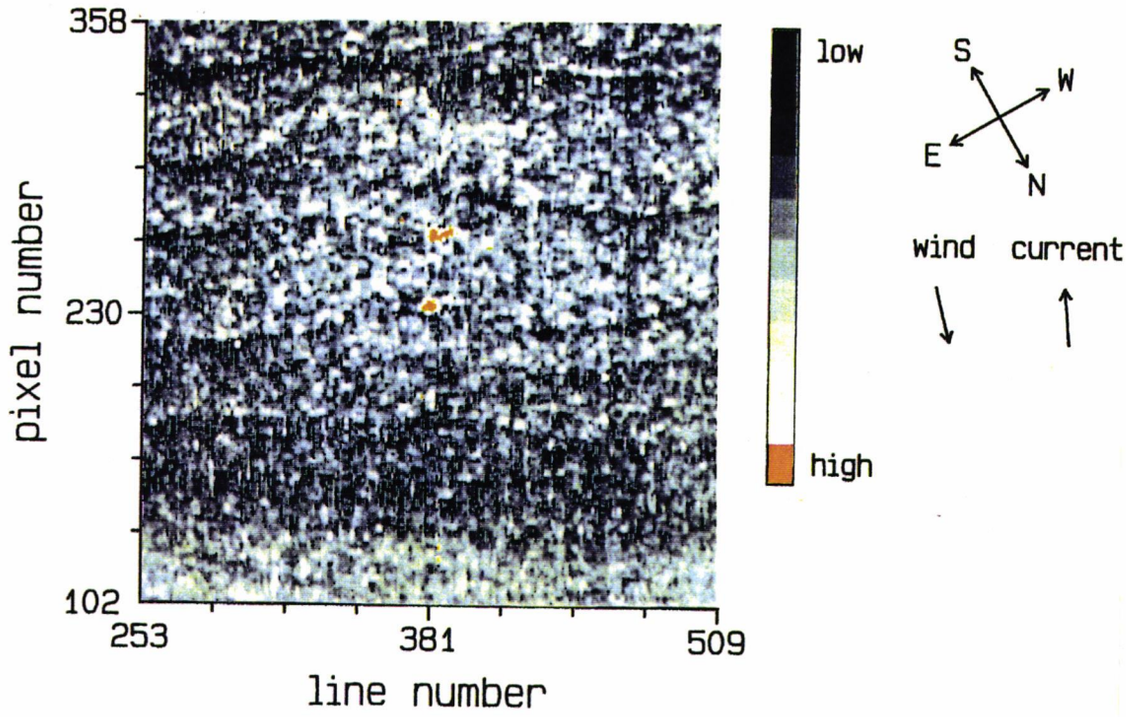

Figure 18a. Central part of the original image 5.

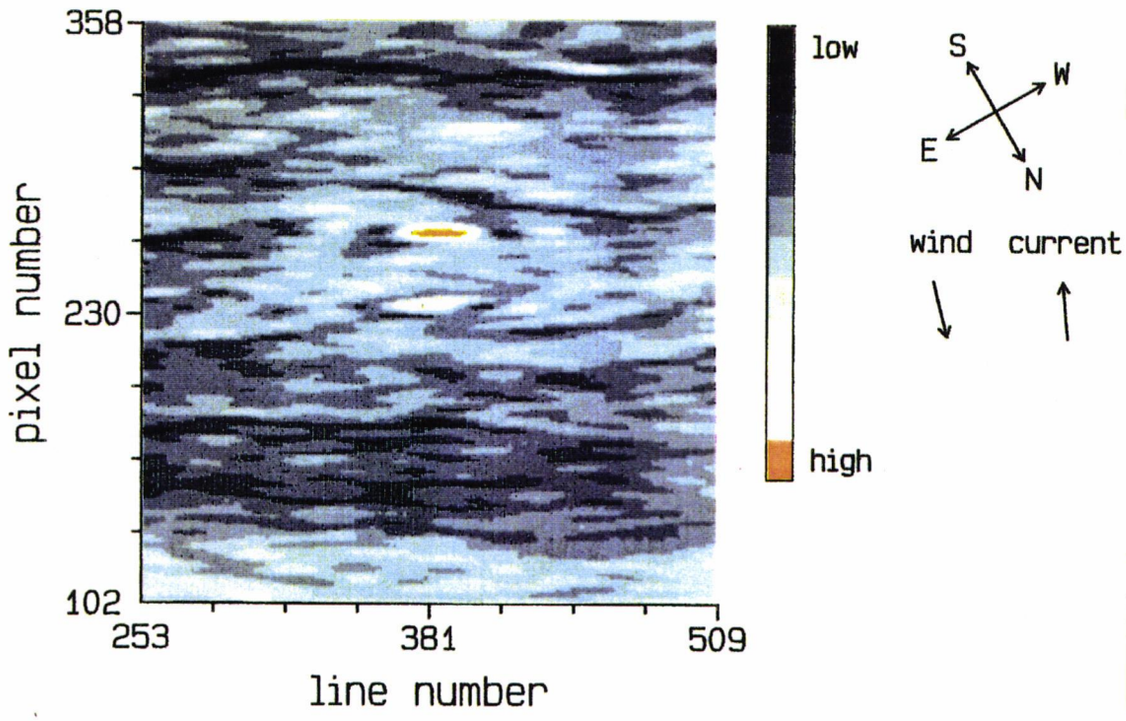

Figure 18b. Central part of image 5 filtered with a two-dimensional low pass Fourier filter.

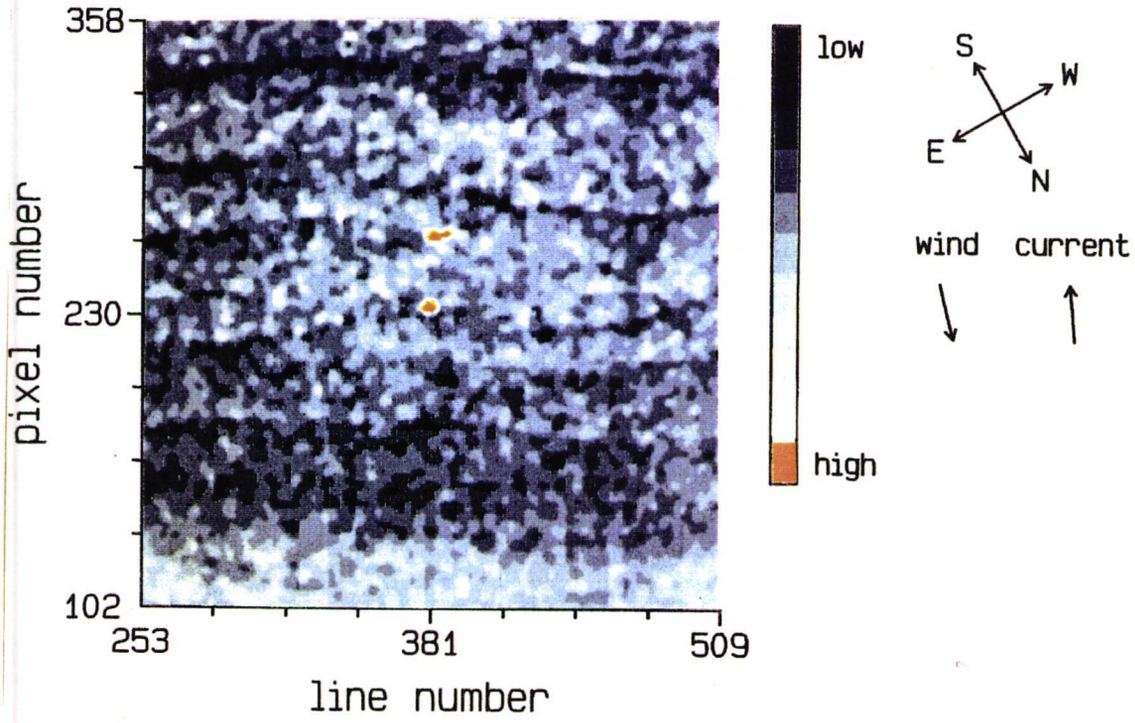

Figure 18c. Central part of image 5 filtered with a 3 x 3 median filter.

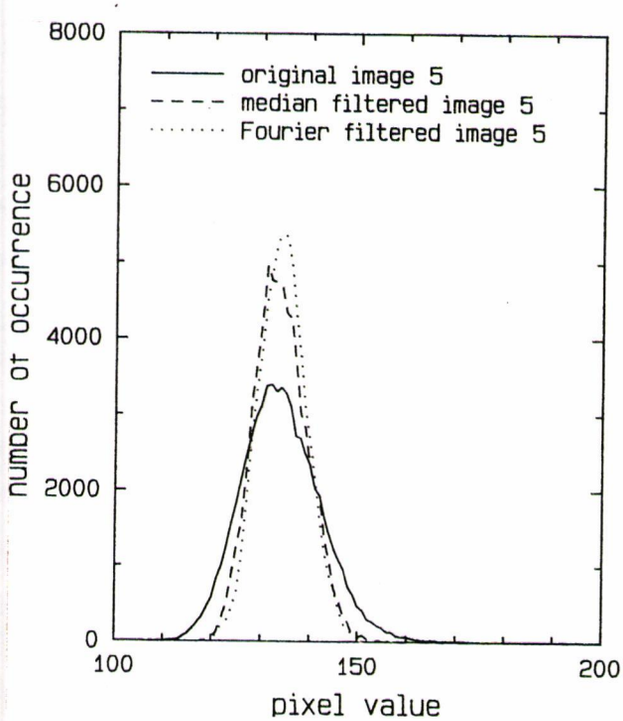

Figure 19. Histograms of the original and filtered images.

6.5 Modulation depth

The pixel value in the images is proportional to the reflection coefficient γ_0, which is related to the radar cross section σ_0 by

$$\sigma_0 = \gamma_0 \cos(\theta) \quad , \tag{48}$$

with θ the angle of incidence. Formula (48) implies that low pixel values indicate low backscatter (low σ_0). A step of size 1 in pixel value corresponds to a step of 0.2 dB in the reflection coefficient. Note that if σ_0 and γ_0 are expressed in a logarithmic scale (decibels), the dependence on θ reduces to an additive term with a value between -1.7 and -6.6.

Figure 20 shows a histogram of the pixel values in the central parts of the original images 1 and 5. Most of the pixels have a value between 100 and 160. The minimum, maximum, mean and median pixel values for these images are listed in table 13. The highest pixel values are caused by the ships and by breaking waves or other radars not recognized by the PARES software.

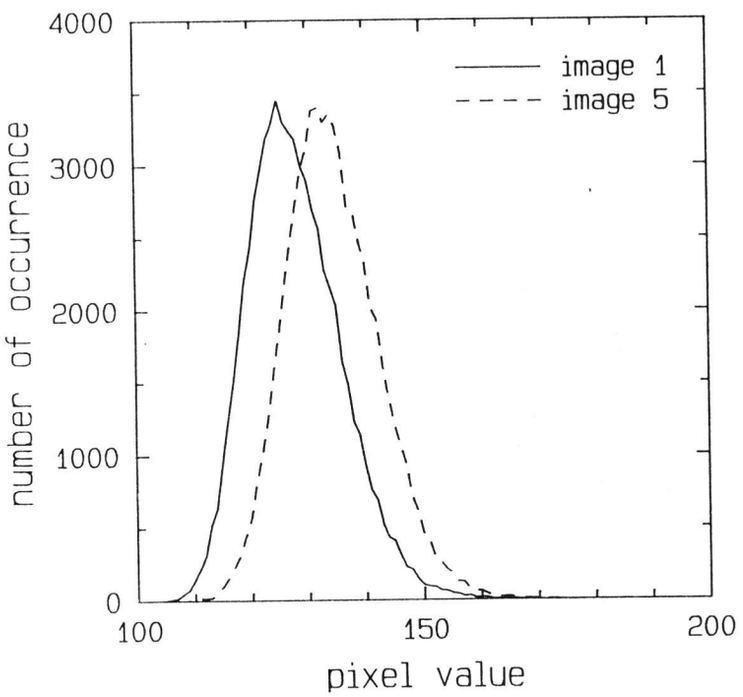

Figure 20. Histogram of the pixel values in the central parts of the original images 1 and 5.

The largest local variation in pixel value due to bottom topography is about 20 (upper right in image 18a), almost the same as the width at half maximum of the curves in figure 20. This corresponds to a variation of 4 dB in the reflection coefficient γ_0. Since θ is nearly the same for pixels not too far apart, the variation in the cross section is about 4 dB.

Image number	Pixel values			
	minimum	maximum	mean	median
1	102	255	129	125
5	107	255	136	132

Table 13. Some characteristics of the pixel values in the central parts of the original images 1 and 5.

If first order Bragg scattering is the dominant scattering mechanism, this modulation of 4 dB corresponds to a modulation depth α (see equation (42b) of section 3.5) of about 0.4. This is an order of magnitude larger than the modulation at X-band predicted by simple relaxation models (see figures 6b and 7b in chapter 3), but of the same order of magnitude as the predictions at L-band. The difference between theoretical and experimental modulations can be explained by other scattering mechanisms as first order Bragg (Holliday, St-Cyr and Woods, 1987) or by non-linear wave-wave interactions (van Gastel, 1987a).

In table 14 the results of this work are compared with those of two other experiments.

Authors	Band	Wind speed	Current modulation	Backscatter modulation
Apel et al. (1985)	L	6 m/s	0.3 m/s	3 - 7 dB
	X	6 m/s	0.3 m/s	2 - 6 dB
Valenzuela et al. (1985)	L	< 7 m/s	0.4 m/s	20 dB
	L	7 - 12 m/s	0.4 m/s	2 - 3 dB
	X	< 7 m/s	0.4 m/s	20 dB
	X	7 - 12 m/s	0.4 m/s	2 - 3 dB
This work	X	7 - 8 m/s	0.2 m/s	4 dB

Table 14. Comparison with other work.

The results in table 14 pertain to internal waves (Apel et al., 1985) and to bottom topography in the Nantucket Shoals (Valenzuela et al., 1985). The current modulation is the difference between minimum and maximum value of the current velocity; it is given by the current induced by an internal wave (Apel et al.) or estimated with the continuity equations (Valenzuela et al. and this work). From table 14 it can be seen that our results agree with those obtained by others at wind speeds of 6 m/s or more. Note that Valenzuela et al. find large modulations (20 dB or more) at low wind speeds.

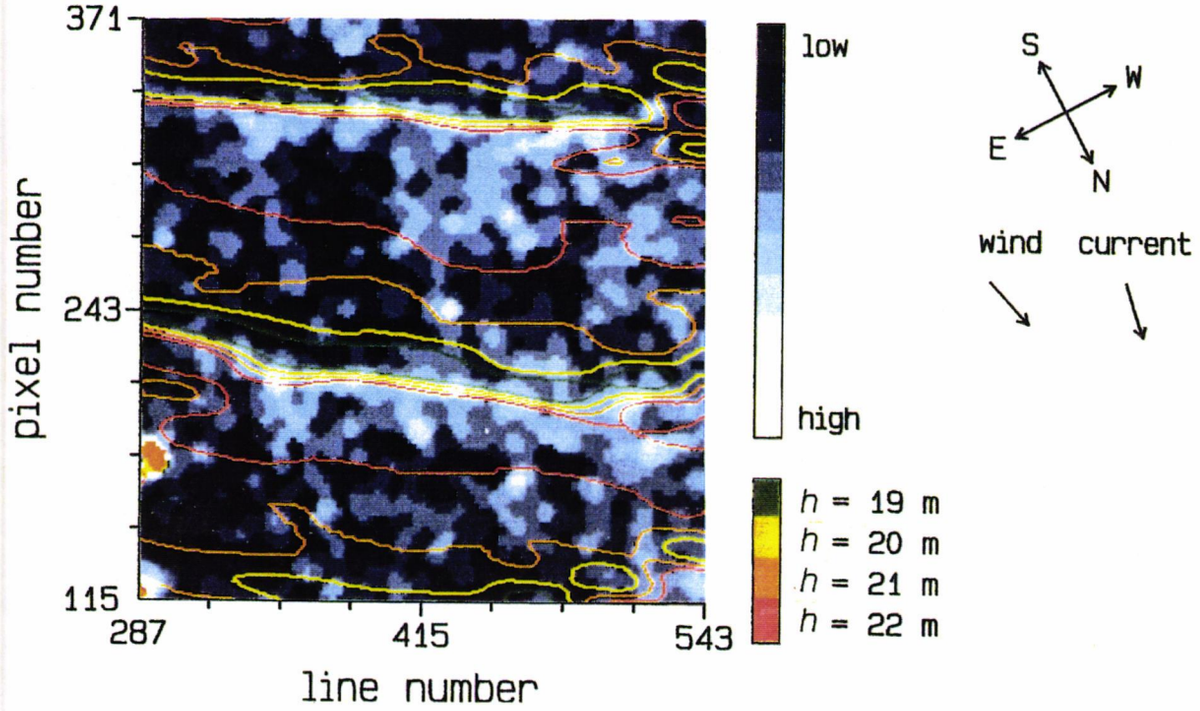

Figure 21a. Part of the 3 x 3 median filtered image 1 with depth contour lines.

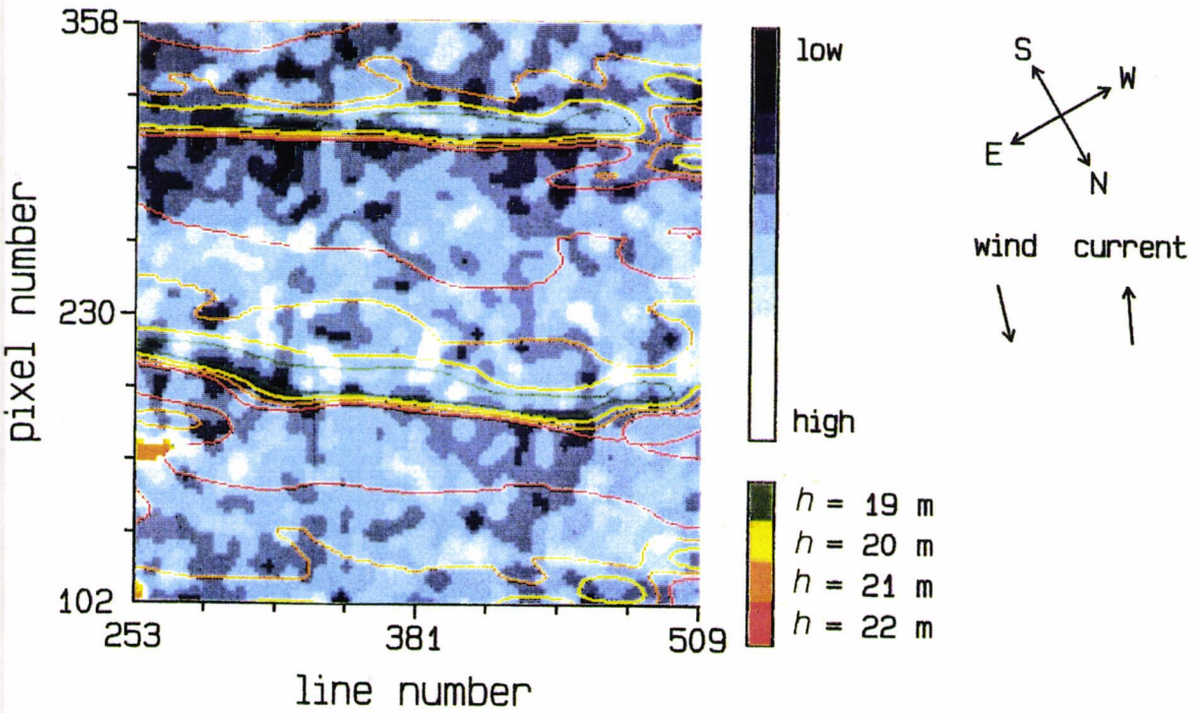

Figure 21b. Part of the 3 x 3 median filtered image 5 with depth contour lines.

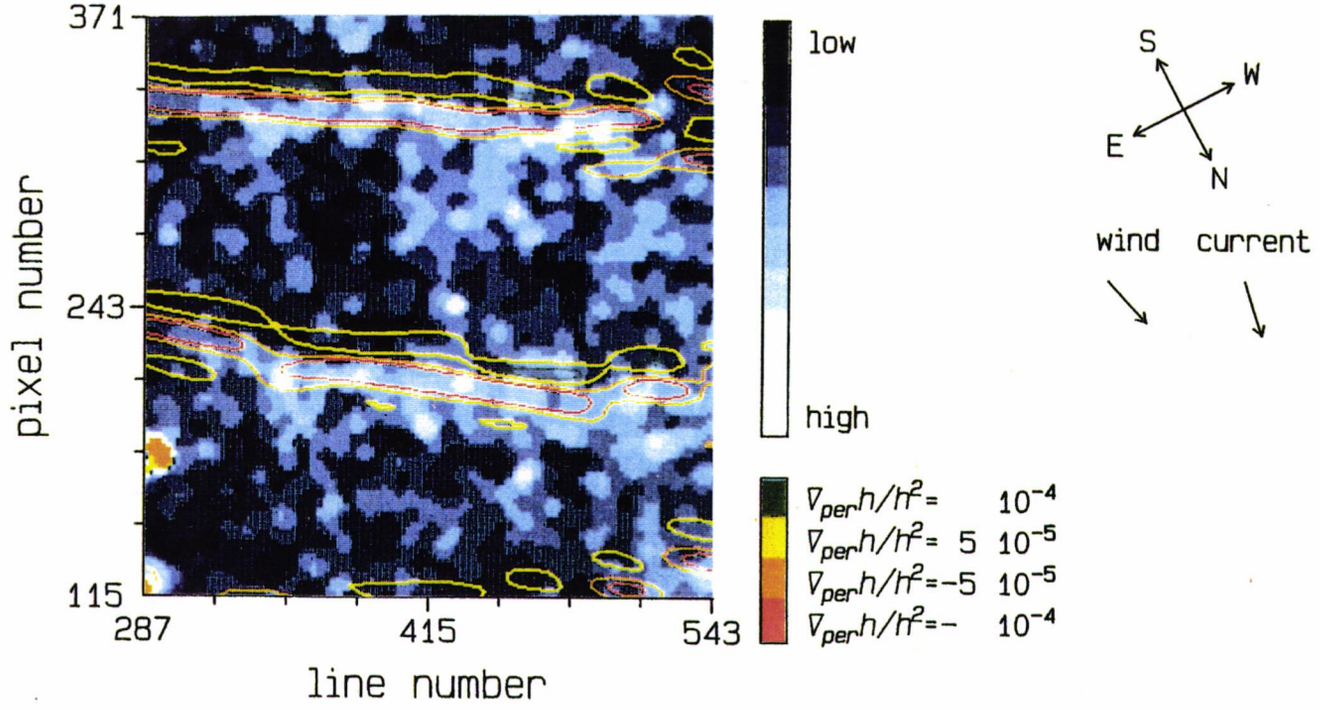

Figure 22a. Part of the 3 x 3 median filtered image 1 with contour lines of $\nabla_{per}(h)/h^2$.

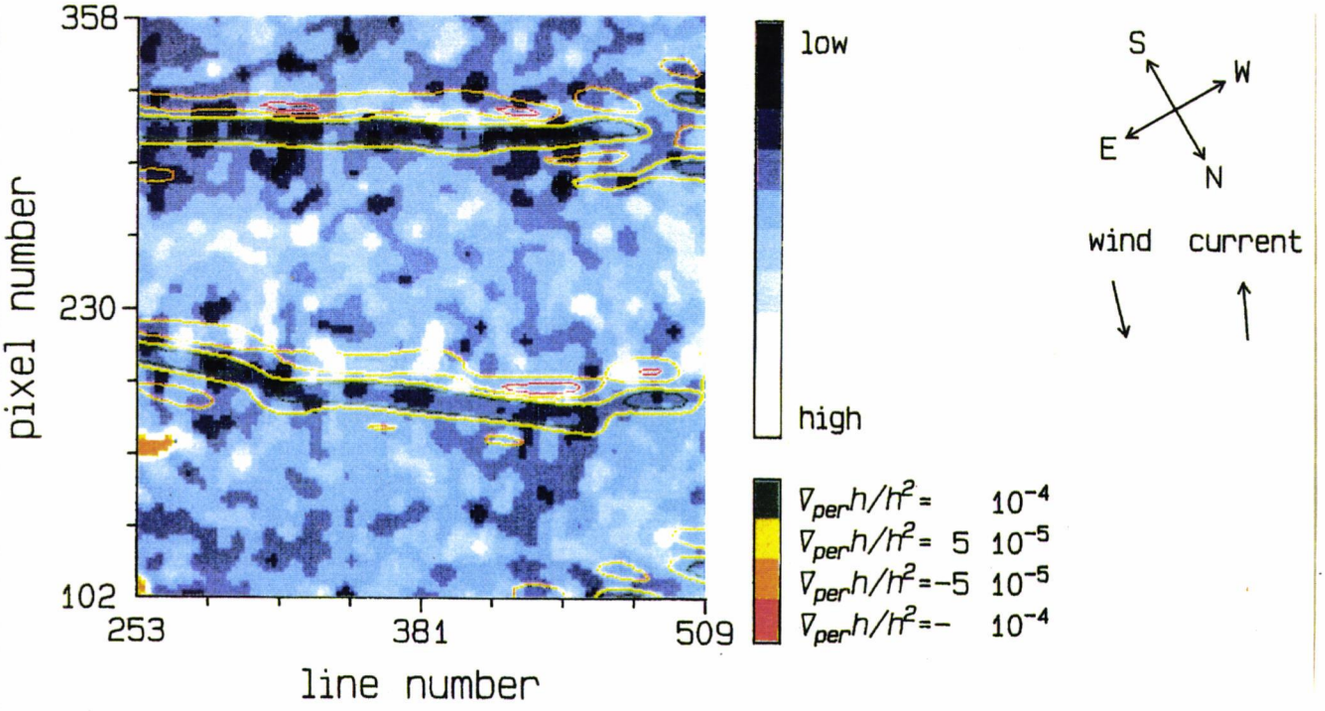

Figure 22b. Part of the 3 x 3 median filtered image 5 with contour lines of $\nabla_{per}(h)/h^2$.

6.6 Comparison with digitized bathymetric maps

The radar images showing the sand waves most clearly, images 1 and 5, were compared with digitized maps of depth and bottom slope. The construction of these maps is described in section 5.2, and the positioning relative to the radar images in section 5.3. Only small parts of the 3 x 3 median filtered images are shown in the next figures, to prevent that these figures are obscured by contour lines or irrelevant details on the radar images.

Figure 21a shows a part of image 1 (line 415 - 543 and pixel 243 - 371) with depth contour lines. Regions where the depth changes rapidly correspond with the light area's in the radar image. Figure 21b shows a part of image 5 (line 381 - 509 and pixel 230 - 358 ; upper right part of image 18c), also with depth contour lines. Here regions where the depth changes rapidly correspond to the dark area's.

Figures 21a and 21b indicate that the extremes in the radar backscatter are located above regions where the depth changes most rapidly, or, stated otherwise, regions with maximum bottom slope. The original model of Alpers and Hennings (1984) predicts that the radar backscatter is proportional to $-\nabla_{per}(h)/h^2$, with h the depth and $\nabla_{per}(h)$ the bottom slope in the direction of the current velocity component normal to the sand wave crests. Positive values of $\nabla_{per}(h)$ correspond to decreasing depth (rising bottom) ; negative values to increasing depth. Therefore the radar images are compared with maps of $\nabla_{per}(h)/h^2$.

The results of this comparison are shown in figure 22a for the same part of image 1 as shown in figure 21a, and in figure 22b for the same part of image 5 as in figure 21b. The direction of the gradient is taken in the range direction (from top to bottom in figure 22a and from bottom to top in figure 22b).

From figures 22a and 22b it can be seen that regions where $|\nabla_{per}(h)/h^2|$ reaches its maximum values correspond with extremes in the radar backscatter. However, there are lighter and darker area's in the radar image which apparently are not related to bottom features. This is most likely due to the poor quality of the radar images, though other effects cannot be ruled out. Nevertheless, it seems that the radar backscatter is lowest where $\nabla_{per}(h)/h^2$ reaches its maximum value and vice versa. In the next section the error in position will be considered.

6.7 Correlation calculations

In the previous section it was concluded that the extremes in the radar backscatter are located above regions where $|\nabla_{per}(h)/h^2|$ has its maximum values. However, this conclusion is based on the comparison of only a small part of images 1 and 5 with maps of the bottom slope. Moreover, the error in the position was not estimated. To get an estimate of this error, the correlation between the pixel value and $\nabla_{per}(h)/h^2$ was calculated. This was done for the central parts of the 3 x 3 median filtered images 1 and 5 (257 lines with 257 pixels each).

The correlation C_j between image and map is defined as

$$C_j = \frac{\overline{MI_j} - \bar{M}\,\bar{I_j}}{[\mathrm{var}(M)\ \mathrm{var}(I_j)]^{1/2}} \quad . \tag{48}$$

In equation (48) $\overline{MI}_j$ stands for the mean value of the product of $\nabla_{per}(h)/h^2$ and pixel value, with the radar image shifted over j pixels in the range (pixel) direction relative to the map. This shift is indicated by the subscript j. $\overline{M}$ is the mean value of $\nabla_{per}(h)/h^2$ and var(M) its variance ; $\overline{I}_j$ is the mean pixel value and var(I_j) its variance. The mean values and variances are calculated for the overlapping parts of map and image. With this definition, the correlation C_j is automatically normalized between -1 and 1. If the pixel value is indeed correlated with $-\nabla_{per}(h)/h^2$, as predicted by the Alpers and Hennings model, the correlation between pixel value and $\nabla_{per}(h)/h^2$ should have a minimum at j = 0.

Figure 23 shows C_j as a function of j for the central parts of image 1 (line 253 - 509 and pixel 102 - 358) and image 5 (line 287 - 543 and pixel 115 - 371). The correlation reaches a minimum at j = 1 for both images. This means that the correlation between pixel value and $-\nabla_{per}(h)/h^2$ reaches its maximum if the radar image is shifted one pixel upward relative to the map. This is well within the estimated error in position (two pixels, 30 m).

Calculations of the correlation with the original images produce similar result. In particular, the minimum correlation is also reached at j = 1 for both image 1 and 5.

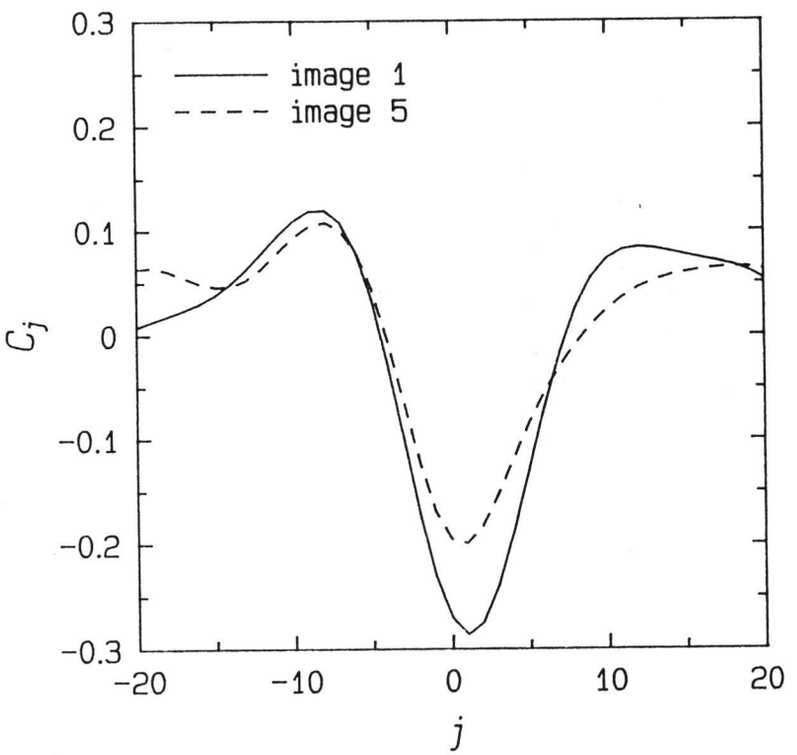

Figure 23. Correlation between pixel value and $\nabla_{per}(h)/h^2$ for the central part of 3 x 3 median filtered images 1 and 5.

The shift j ranged from -20 to 20 pixels in these calculations. Comparison of larger parts of the images with maps of $\nabla_{per}(h)/h^2$ showed that the shift should be within this interval. Notably the fork in the sand waves above the ships, which is also visible on the bathymetric maps, fixes the possible values of j well within these limits. It should be noted that the correlation C_j is a periodic function of j, since both the radar images and the maps of $\nabla_{per}(h)/h^2$ show periodic features. Figure 23 shows only a part of the period around j = 0 for the reasons mentioned above.

The correlation calculations presented in this chapter were performed with a shift perpendicular to the sand wave crests. Also the correlation with the shift parallel to the sand wave crests was calculated. These calculations show a very broad minimum around j = 0 as expected, since the bottom topography is quasi one-dimensional and the current velocities parallel to the sand wave crests are small. These calculations are not shown here.

The correlation calculations show that the extremes in the radar backscatter are positioned directly above regions where $|\nabla_{per}(h)/h^2|$ has its maximum values, with an error of 2 pixels (30 m). Since the change in depth is small compared to the change in bottom slope, this means that the extremes in the radar backscatter are located right above regions with maximum bottom slope. The intensity in the radar image increases (positive modulation) if the depth increases in the current direction (negative bottom slope) and vice versa.

This is a most important result. Bottom signatures in X-band radar images are directly related to the bottom slope, as expected from previous X-band and SEASAT L-band measurements. This facilitates the interpretation of such images. The result is in perfect agreement with predictions from simple relaxation models. In particular advection is not important for X-band at high winds.

The sand waves have an asymmetric profile ; they look more like a sawtooth than like a sine (see figure 13). The steeper sides are directed to the Northeast. It are these sides that show up in the radar images, as light bands (positive modulation) if the current is directed from SW to NE (image 1) and as dark bands (negative modulations) for the opposite current direction (image 5). The other sides with gentle slopes cause a smaller and opposite modulation. They act as a background, since they take a much larger area and since there are no flat area's for reference. Taking the background levels equal to the median pixel values from table 13, it appears that the background level in image 5 is 1.4 dB higher than that in image 1. This difference cannot be caused by the wind, since the wind speed was lowest during the recording of image 5. However, it should be kept in mind that the images are only relatively calibrated. As a consequence, it is dangerous to compare intensities of different images with each other. This is also indicated by the fact that the minimum pixel value in image 5 is 1 dB higher than that in image 1.

6.8 Inverse modelling

In the previous sections the positional relation between radar images and bathymetric maps was studied, with the result that this relation confirms the predictions by simple relaxation models of the imaging mechanism. Therefore inverse modelling seems possible : the calculation of the bottom slope (or, more precisely, $\nabla_{per}(h)/h^2$) from the radar images.

According to the model of Alpers and Hennings (1984) the radar backscatter is proportional to $-\nabla_{per}(h)/h^2$. However, this is valid under the assumption that first order Bragg scattering is the dominant scattering mechanism, which probably is not the case at X-band (see the discussions in section 6.5 and chapter 3).

The relation between these two quantities is shown in figures 24a and 24b for the central part of image 5 (line 253 to 509 and pixel 102 to 358). Figure 24a shows the result for the original image (see figure 18a) and figure 24b for the 3 x 3 median filtered image (see figure 18c). Since most of the bottom in the test area has small slope, these figures include only the data points with $|\nabla_{per}(h)/h^2|$ greater than or equal to 0.00005, corresponding to slopes exceeding approximately 2%.

These figures indicate that there is a relation between pixel value and $\nabla_{per}(h)/h^2$: low pixel values (dark area's) tend to cluster at large positive values of $\nabla_{per}(h)/h^2$. This again indicates that the pixel value is proportional to $-\nabla_{per}(h)/h^2$, in agreement with simple relaxation models. However, there is a lot of spreading in the data, obscuring the relation between pixel value and bottom slope. This is most likely due to the poor quality of the radar images. Note that the spreading is smaller for the 3 x

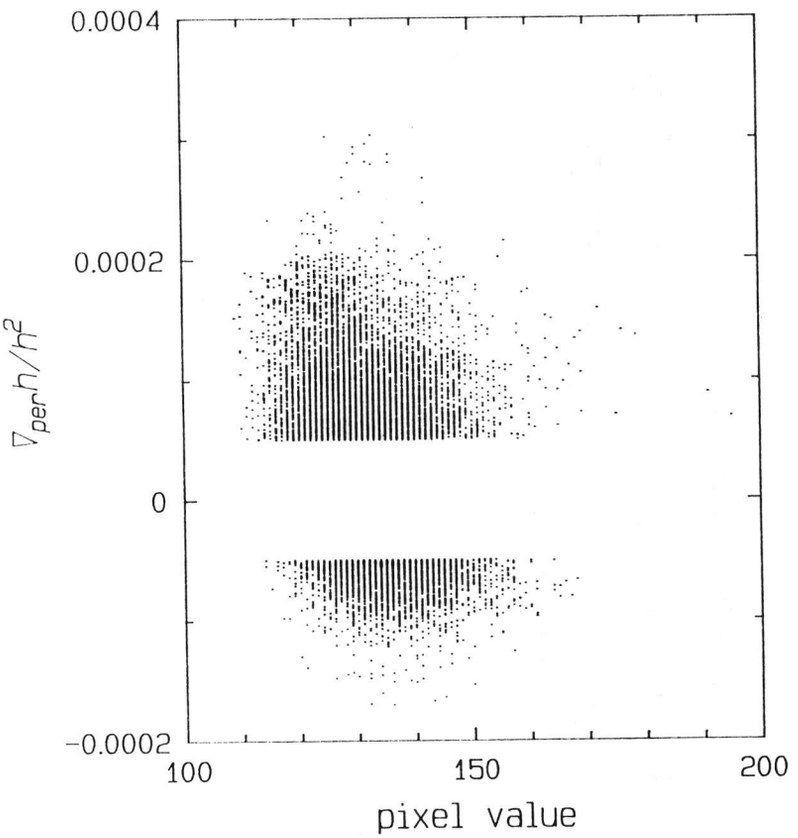

Figure 24a. Relation between pixel value and $\nabla_{per}(h)/h^2$ for the central part of the original image 5.

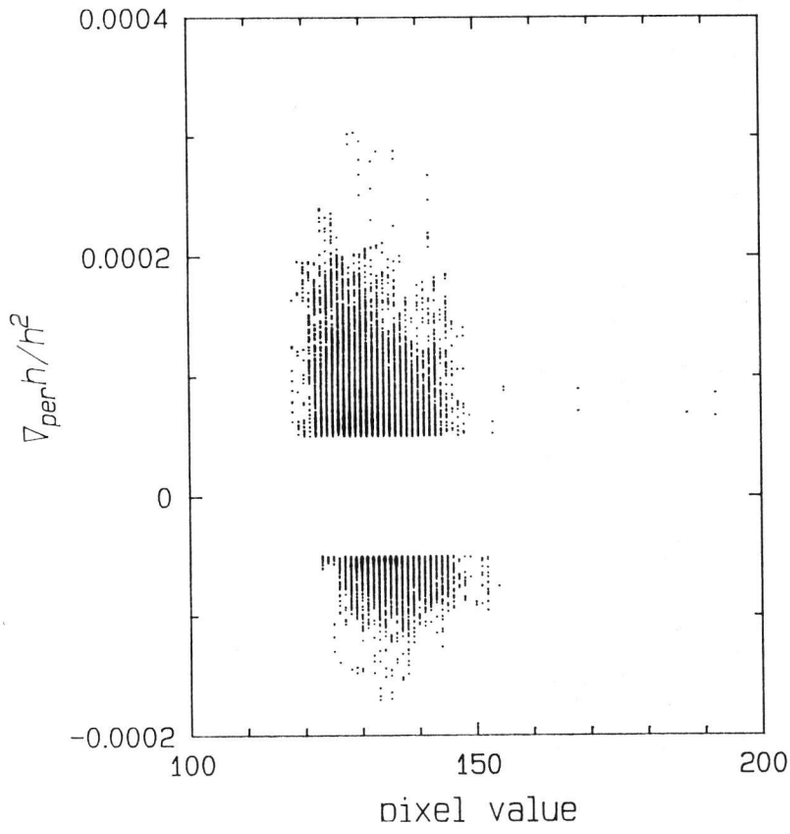

Figure 24b. Relation between pixel value and $\nabla_{per}(h)/h^2$ for the central part of the 3 x 3 median filtered image 5.

3 median filtered image, since this filter removes extreme pixel values (see figure 19).

From figures 24a and 24b it is concluded that the quality of the images is not good enough for a precise calculation of the bottom slope from the radar images, and that better images are needed to study inverse modelling.

6.9 Conclusions

From the results of the main experiment a number of conclusions was drawn. These conclusions are summarized below :

1. The results of the current velocity measurements agree with the continuity equations unless the current velocity vanishes. More elaborate measurements are needed to establish whether or not the continuity equations indeed give a good description of the current.
2. The sand waves in the radar images can be made better visible by filtering the images. A median filter gives the best results.
3. The extremes in the radar backscatter are positioned right above regions with maximum bottom slope, with an error of two pixels (30 m). This is in perfect agreement with predictions from simple relaxation models.

4. Radar images with range direction perpendicular to the sand wave crests show the bottom topography more clearly than images with range direction parallel to the sand wave crests. According to simple relaxation models, bottom topography should not be visible in the latter case. This might be due to the fact that the test area is not quasi one-dimensional. An other possibility is that the continuity equations are an oversimplification.
5. The wind speed during which the radar images were recorded (between 7.3 and 8.3 m/s) is only slightly above the minimum wind speed for the Dutch Digital SLAR. Therefore images made in the upwind direction do show bottom topography, in contrast with images made in the downwind direction. Also the meteorological conditions were slightly stable. This can affect the quality of the images in a negative way.
6. The quality of the radar images obtained during the experiment is not good enough (for the reasons mentioned above) to allow inverse modelling. Better images are needed to study the possibility of calculating bottom slopes from radar imagery.
7. The modulation in the backscattered intensity due to bottom topography is of the order of 10%, in agreement with other experiments. This is of the same order of magnitude as found for L-band images, and an order of magnitude larger than the hydrodynamic modulation predicted by simple relaxation models.

7 CONCLUSIONS AND RECOMMENDATIONS

7.1 General remarks on the imaging mechanism

From the experimental and theoretical results presented in the previous sections the following general picture of the imaging mechanism emerges : the interaction between tidal current and bottom topography produces modulations in the surface wave spectrum, visible as spatial modulations in the radar cross section of the sea.

On theoretical grounds one expects that these modulations are proportional to the modulation in the current velocity. This is supported by the disappearance of bottom topography in SLAR images when the current velocity vanishes (de Loor, 1981). It should be noted that this is a qualitative observation. No precise measurements of the relation between current velocity and modulation in the radar backscatter are available.

The modulation in the radar backscatter decreases with increasing wind speed, due to the increasing roughness of the sea which tends to wipe out the bottom topography patterns. Large banks are visible even at 12 m/s (6 Bft) or more. This does not automatically imply that low wind speeds are favorable for mapping bottom topography, since a minimum wind speed exists at which the backscatter from the sea is detectable with the radar system. The value of this minimum wind speed depends on the sensitivity of the radar system. The modulation in the radar backscatter on the one hand and the sensitivity of the radar system on the other hand therefore define the optimum wind speed, which is above the minimum wind speed. When the wind speed is slightly above its minimum value, bottom topography may be visible in images taken in the upwind direction but not in those taken in the crosswind or downwind direction. This is due to the well known upwind/downwind asymmetry in the radar cross section of the sea.

At X-band the extreme values of the modulation in the radar backscatter are located above regions with largest slope, in agreement with predictions of simple relaxation models. The modulation in the radar backscatter is positive (increased backscatter) when the bottom slope is negative (increasing depth) in the current velocity direction and vice versa. At low wind speeds theory indicates that the patterns in the radar image are shifted in the direction of the current (see chapter 3). This effect will be much stronger at L-band than at X-band. It can be of some importance for C-band, the band at which the ERS-1 SAR will operate.

The measurements of the current velocity are in agreement with the continuity equations for non-vanishing current. However, these measurements can not be regarded as conclusive evidence for the validity of the continuity equations, due to the large errors in the measurements. It may be possible that the position of the maximum current velocity is shifted relative to the position of minimum depth. Since the results of the main experiment show that the extreme values in the radar backscatter are located above regions of maximum slope for opposing current directions, this shift is expected to be small.

The magnitude of the modulation in the radar backscatter at X-band can not be explained by the simple relaxation models : the measured modulations are an order of magnitude larger than the hydrodynamic modulations predicted by these models. This may be due to the use of first order Bragg scattering as the dominant backscatter mechanism. Inclusion of the influence of the longer waves by using two scale models or models based on the

Stratton-Chu integral equation increases the magnitude of the modulations. An other possibility is inclusion of wave-wave interactions in the source term of the action balance equation.

Finally the atmospheric conditions should be neutral or instable (sea water temperature equal to or higher than air temperature), since at stable conditions the radar cross section of the sea decreases strongly.

7.2 Usability of imaging radar for cartographic purposes

The results of the main experiment show that at X-band and at high winds (> 7 m/s) the extremes in the radar modulations are located above the regions with largest slope, in agreement with theoretical predictions. This is a most important result if radar images are to be used for cartographic purposes. It implies that a radar image shows the bottom slope (first derivative of the depth) of the recorded area.

The positional accuracy depends on the radar system and the visibility of known points in the image. If the image is geometrically corrected for the movements of the radar platform (pitch, roll and yaw), five parameters determine the geographical position of each pixel in the image : flight direction, pixel size in both range and flight direction and the geographical coordinates of the first pixel. In the general case three known points are needed to fix these five parameters. In case of the Dutch Digital SLAR the geographical position of the first pixel as given by the PARES software can vary several hundreds of meters during a flight. Since both flight direction and pixel size are reliable, one known point suffices to determine the geographical position. The procedure for fixing the five parameters that determine the geographical position is described in section 5.2.

The positional accuracy of the images obtained during the main experiment is two pixels (30 m) or better. For other radar systems like the ERS-1 C-band SAR the positional accuracy is estimated also two pixels or better. It is hard to estimate the positional accuracy of images that are not geometrically corrected, like the 'oil-SLAR' images. Such images can not be used for precise cartographic purposes.

The images recorded during the main experiment clearly show elongated area's about 50 m wide (3 - 4 pixels) that can be related to sand wave slopes of 0.04 or more. In principle it should be possible to map area's that are one pixel wide. In practice the minimum size and minimum slope that can be detected are determined by the quality of the images.

The quality of the images recorded during the main experiment is rather poor, due to the low sensitivity of the Dutch Digital SLAR. The bottom features can be made visible more clearly by false coloring. The images can be smoothed by filtering. Good results have been obtained with a median filter.

Radar imagery of shallow seas (depth less than 50 m) gives an overview of the bottom slope in the recorded area. This implies that a number of important practical applications seem possible (Hennings, 1988) :

1. Mapping of subsurface structures for routing (oil or gas) pipelines or telephone cables
2. Monitoring changes in bottom structures to optimize bathymetric surveys.
3. Information about the momentary current velocity and direction if the bottom topography of the area is known.
4. Information about the depth if the current velocity and the bottom topography of the area is known.

It should be noted that SEASAT SAR images of the Southern Bight of the North Sea have been used to choose the route of telephone cable UK-NL 12.

7.3 Conclusions regarding the optimum hydro-meteo conditions

From the results presented in this work the following conclusions regarding the optimum hydro-meteorological conditions for mapping bottom topography with imaging radar can be drawn :

1. The current velocity should be as large as possible and certainly above 0.4 m/s.
2. The wind speed should be above the minimum wind speed at which the radar backscatter of the sea is detectable by the radar system.
3. At wind speeds slightly above the minimum wind speed the radar range direction should be upwind.
4. The atmospheric conditions should be neutral or instable.

7.4 Conclusions regarding the practical usability of imaging radar

From the results presented in this work the following conclusions regarding the practical usability of mapping bottom topography with imaging radar can be drawn :

1. At X-band and high wind radar images show the bottom slope (first derivative of the depth). Such images can be used for a number of practical applications like monitoring bottom topography to optimize bathymetric surveys and routing pipelines or telephone cables, as well as for studying the dynamical behaviour of bottom structures.
2. The applications mentioned above can be of great value for regions where the bottom topography is not well known like the coastal waters of developing countries.
3. If a radar image is geometrically corrected for the movements of the radar platform (pitch, roll and yaw) and if enough known points are visible in it, a positional accuracy of two pixels or better can be achieved with the procedure outlined in section 5.2.
4. Elongated structures that are at least 3 - 4 pixels wide and that have a slope of at least 0.04 can be made visible with the Dutch Digital SLAR. Smaller area's with smaller slope are expected to be visible using a more sensitive radar system.
5. Bottom topography in radar imagery can be made more clearly visible by filtering with a median filter.

7.5 Recommendations

There are still a lot of unknown factors in the imaging mechanism. Therefore further research is needed to clarify their role. Some of these factors, like the form of the source terms in the action balance equation and the influence of long gravity waves on the current velocity profile (wave-current interaction), are of a fundamental nature. These should be studied in laboratory experiments. Other factors can be studied in future field experiments.

The influence of the magnitude of the modulation in the current velocity on the modulation in the radar backscatter is not well known. Also the relation between the wind speed and the magnitude of the modulation in the radar backscatter is not well known. These can be studied quantitatively during the ERS-1 mission starting in 1990 by taking C-band SAR images at several phases of the tidal cycle. The first ERS-1 images of the Dutch coastal waters are expected to be available in 1991. The mission with the JPL aircraft carrying P-, L- and C-band polarimetric SAR in the second half of 1989 can be used as a preparation for the ERS-1 mission.

It is expected that the patterns in radar images will shift in the direction of the current velocity if the radar wave length increases. This shift is an important factor if radar images are to be used for cartographic means. The SIR-C/X-SAR (Shuttle Imaging Radar) mission in 1991/1992 provides an excellent opportunity to study this shift, since the Shuttle will carry polarimetric L-, C- and X-band SAR.

It is not known whether the maximum surface current velocity is located precisely above the minimum depth or not. The measured current velocities indicate that this is the case, for the continuity equations are valid. An experiment using an array of self-registrating Doppler current meters over a sand wave should be considered. These Doppler current meters measure the complete velocity profile and are expected to be available in the near future.

It is also recommended that the Dutch Digital SLAR is modified for use above sea. At the moment it is a rather insensitive instrument, bottom topography being visible only at high wind speeds (> 8 m/s). One possibility is the change of the existing HH polarized antenna with a longer one or with a VV polarized one. This would greatly improve the performance of the Dutch Digital SLAR above sea, since the backscatter of the sea at VV polarization is about 5 dB higher than at HH polarization. Adaption of the IF amplifier (narrowing the bandwidth) when the longer pulse length is used (as in this exercise) would also give an improvement of a 3 to 5 dB. An other possibility is to increase the emitted power. This, however, requires a major revision of the system (a new TR box).

There is a tendency to increase the resolution of new imaging radar systems (smaller pixel sizes). It should be noted that this decreases the radiometric sensitivity, affecting the usability of the radar system above sea in a negative way. It is recommended that this point is kept in mind in the design of new radar systems.

ACKNOWLEDGEMENTS

This work was funded by the Dutch Remote Sensing Board (BCRS) as a part of the National Remote Sensing Program (NRSP). Many people have made contributions in some way or another. The authors wish to thank them all, in particular the following persons :

I. Hennings (University of Bremen), G.J. Komen (Royal Netherlands Meteorological Institute) and J.T.F. Zimmerman (Netherlands Institute for Oceanic Research) for their interest in this work and stimulating discussions about the theory of the imaging mechanism. I. Hennings is also thanked for providing the Alpers and Hennings model including advection prior to publication.

J. Wiersma (RWS-DNZ) for his interest in this work and stimulating discussions about hydrodynamics and imaging mechanism.

R. Cramer, J. Huisman, P.J. Hulsebos, J.B. Martin and P.P. Verburg (Rijkswaterstaat, North Sea Directorate), the pilots of the oil patrol aircraft, for making the 'oil-SLAR' images and their cooperation in collecting these images.

A. Roskam (Rijkswaterstaat, Tidal Waters Division) for his help in retrieving the wind and wave data used to evaluate the 'oil-SLAR' images.

G.L. Lamers, the pilot of the National Aerospace Laboratory aircraft, and his crew, who repeated some tracks because the ships measuring the current velocity had not yet arrived.

Captains and crew of the Rijkswaterstaat ships 'Octans' and 'Smal Agt', in particular T. Krijthe, D. Pimentel, A.T. Visser and H. Wervers who performed the current velocity measurements.

G.H.F.M. Hesselmans (Delft Hydraulics) for the further processing of the radar images and the correlation calculations.

T.J. Zitman, P. Santbergen and C.F. de Valk (Delft Hydraulics) for analyzing and processing the current velocity measurements.

REFERENCES

ALPERS, W. and HENNINGS, I., 1984,
A theory of the imaging mechanism of underwater bottom topography by real and synthetic aperture radar.
Journal of Geophysical Research, 89 C, 10529 - 10546.

VAN ALPHEN, J.S.L.J. and DAMOISEAUX, M.A.,
Geomorfologische kaart van de Nederlandse kustwateren, 1:150000, Blad Hollandse kust.
Rijkswaterstaat, Directie Noordzee en Meetkundige Dienst, The Hague, The Netherlands.

APEL, J.R., et al. (SARSEX Experimental Team), 1985,
SARSEX interim report.
JHU/APL STD-R-1200, The John Hopkins University/Applied Physics Laboratory, Laurel, Maryland.

BARRICK, D.E., 1968,
Rough surface scattering based on the specular point theory.
IEEE Transactions on Antennas and Propagation, 16, 449 - 454.

CHARNOCK, H., 1955,
Wind stress on a water surface.
Quarterly Journal of the Royal Meteorological Society, 81, p. 639.

DAVIES, A.M., 1987,
On extracting current profiles from vertically integrated numerical models.
Coastal Engineering, 11, 445-477.

DAVIES, A.M., 1988,
On formulating two-dimensional vertically integrated hydrodynamic numerical models with an enhanced representation of bed stress.
Journal of Geophysical Research, 93 C, 1241 - 1263.

DIENST DER HYDROGRAFIE VAN DE KONINKLIJKE MARINE, 1976,
Stroomatlas Noordzee, zuidelijk deel.
The Hague, The Netherlands.

DIENST DER HYDROGRAFIE VAN DE KONINKLIJKE MARINE, 1984,
Minuutblad HY-71-LM-41.
The Hague, The Netherlands.

FUNG, A.K., 1968,
Mechanisms of polarized and depolarized scattering from a rough dielectric surface.
Journal of the Franklin Institute, 285, 125 - 133.

GARRATT, J.R., 1977,
Review of drag coefficients over oceans and continents.
Monthly Weather Review, 105, 915 - 929.

VAN GASTEL, K., 1987a,
Imaging by X-band radar of subsurface features: a nonlinear phenomenon.
Journal of Geophysical Research, 92 C, 11857 - 11865.

VAN GASTEL, K., 1987b,
Velocity profiles of tidal currents over sand waves.
Netherlands Journal of Sea Research, 21, 159 - 170.

HASSELMANN, K., 1960,
Grundgleichungen der Seegangsvorhersage.
Schiffstechnik, 7, 191 - 195.

HENNINGS, I., 1985,
Moeglichkeiten der Bestimmung der Richtung des Nettosandtransportes aus Radar-Satellitenbildern.
Deutsche Hydrographische Zeitschrift, 38, 119 - 132.

HENNINGS, I., 1988,
Abbildung von submariner Bodentopographie auf Luft- und Satellitbildern im Mikrowellenbereich und im sichtbaren Bereich des elektromagnetischen Spektrums.
Thesis, Universitaet Bremen, Bremen

HOLLIDAY, D., ST-CYR, G., and WOODS, N.E., 1986,
A radar ocean imaging model for small to moderate incidence angles.
International Journal of Remote Sensing, 7, 1809 - 1834.

HOLLIDAY, D., ST-CYR, G., and WOODS, N.E., 1987,
Comparison of a new ocean imaging model with SARSEX internal wave image data.
International Journal of Remote Sensing, 8, 1423 - 1430.

HUGHES, B.A., 1978,
The effect of internal waves on surface wind waves. 2. Theoretical analysis.
Journal of Geophysical Research, 83 C, 455 - 465.

INOUE, T., 1967,
On the growth of a spectrum of a wind generated sea according to a modified Miles-Phillips mechanism and its application to wave forecasting.
Report TR-67-5, Geophysics Science Laboratory, New York University, New York.

KASISCHKE, E.S., SHUCHMAN, R.A., LYZENGA, D.R. and MEADOWS, G.A., 1983,
Detection of bottom features on SEASAT Synthetic Aperture Radar imagery.
Photogrammetric Engineering and Remote Sensing, 49, 1341 - 1353.

KNMI (Royal Netherlands Meteorological Institute), 1986 and 1987,
Monthly Bulletin North Sea,
KNMI, de Bilt, The Netherlands

KWOH, D.S.W., LAKE, B.M. and RUNGALDIER, H., 1986,
Identification of the contribution of Bragg-scattering and specular reflection to X-band microwave backscattering in an ocean experiment. TRW, Space and Techn. Group, California.

LODGE, D.W.S., 1983,
Surface expression of bathymetry on SEASAT synthetic aperture radar images.
International Journal of Remote Sensing, 4, 639 - 653.

DE LOOR, G.P. and BRUNSVELD VAN HULTEN, H.W., 1978,
Microwave measurements over the North Sea.
Boundary Layer Meteorology, 13, 113 - 131.

DE LOOR, G.P., 1981,
The observation of tidal patterns, currents and bathymetry with SLAR imagery of the sea.
IEEE Journal of Oceanic Engineering, OE-6, 124 - 129.

DE LOOR, G.P., 1988,
Slope modulation of the radar backscatter by sea waves.
Report BCRS-88-05, Netherlands Remote Sensing Board, Delft, The Netherlands

McLEISH, W., SWIFT, D.J.P., LONG, R.B., ROSS, D. and MERRILL, G., 1981,
Ocean surface patterns above sea-floor bedforms as recorded by radar, Southern Bight of the North Sea.
Marine Geology, 43, M1 - M8.

PHILLIPS, O.M., 1984,
On the response of short ocean wave components at a fixed wave number to ocean current variations.
Journal of Geophysical Research, 83 C, 1425 - 1433.

RIJKSWATERSTAAT, Directie Waterhuishouding en Waterbeweging, 1976/1987
Getijdetafels voor Nederland 1977/1988.
Staatsuitgeverij, The Hague, The Netherlands.

RUFENACH, C. and SMITH, C., 1985,
Observation of internal waves in LANDSAT and SEASAT satellite imagery.
International Journal of Remote Sensing, 6, 1201 - 1207.

SHUCHMAN, R.A., LYZENGA, D.R. and MEADOWS, G.A., 1985,
Synthetic Aperture Radar imaging of ocean-bottom topography via tidal-current interactions: theory and observations.
International Journal of Remote Sensing, 6, 1179 - 1200.

STRATTON, J.A., 1941,
Electromagnetic theory, chapter 8.
McGraw-Hill, New York.

TERWINDT, J.H.J., 1971,
Sand waves in the Southern Bight of the North Sea.
Marine Geology 10, 51 - 67.

ULABY, F.T., MOORE, R.K. and FUNG, A.K., 1982,
Radar remote sensing. Volume II, chapter 12.
Addison-Wesley, Reading, Massachusetts.

VALENZUELA, G.R., 1968,
Depolarization of EM waves by slightly rough surfaces.
IEEE Transactions on Antennas and Propagation, AP-15, 552 - 557.

VALENZUELA, G.R., 1978,
Theories for the interaction of electromagnetic and oceanic waves - a review.
Boundary Layer Meteorology, 13, 61 - 85.

VALENZUELA, G.R., PLANT, W.J., SCHULER, D.L., CHEN, D.T. and KELLER, W.C., 1985,
Microwave probing of shallow water bottom topography in the Nantucket Shoals.
Journal of Geophysical Research, 90 C, 4931 - 4942.

VESECKY, J.F. and STEWART, R.H., 1982,
The observation of ocean surface phenomena using imagery from the SEASAT Synthetic Aperture Radar : an assessment.
Journal of Geophysical Research, 87 C, 3397 - 3430.

VOGELZANG, J., 1988,
The mapping of bottom topography with imaging radar: a comparison of the hydrodynamic modulation in some existing models.
Rijkswaterstaat note GWAO-88.379, Rijkswaterstaat, Tidal Waters Division, The Hague, The Netherlands. (Accepted for publication in the International Journal of Remote Sensing, 1989).

WILLEBRAND, J., 1975,
Energy transport in a nonlinear and inhomogeneous random gravity wave field.
Journal of Fluid Mechanics, 70, 113 - 126.